SHANDONG UNIVERSITY

UNIVERSIDAD AUTÓNOMA DE MADRID

Fabricaiton and Characterization of Waveguide Structures in Transparent Optical Materials

Doctoral Dissertation

Submitted to

Shandong University and Universidad Autónoma de Madrid

By

Ruiyun He

(Condensed Matter Physics)

Co-supervised by:

Prof. Feng Chen (Shandong University)

and

Prof. Daniel Jaque (Universidad Autónoma de Madrid)

目　录

CONTENTS

中 文 摘 要

集成光路可以将光信号限制在高度集成化的区域内进行传输和处理，由于其具有体积小、稳定性好、损耗小等优势，自 20 世纪 60 年代集成光路的概念被提出以来，传统的集成电路逐渐被集成光路所替代。集成光路由多种功能性元件集合而成，基本元件包括连接器、功率分束器、波导反射器、定向耦合器、偏振片、偏振分束器、相位调制器、功率调制器、TE/TM 模式转换器和频移器。而各功能元件都基于集成光学中的基本结构——光波导。光波导是一个被折射率较低的区域包围的折射率较高的区域，利用全反射原理将光限制在其内部传输，由于光波的波长较短，可以将光信号控制在微米甚至亚微米尺度内，获得较高的腔内光密度。光波导作为集成光路的基本元件，可以连接各功能元件对光信号进行操控，实现耦合、分支、开关、复用等功能。根据对光信号在三维空间中的限制能力，光波导可分为一维、二维和三维光波导。其中，一维光波导即平面光波导；二维光波导根据结构又可划分为脊型、条形、埋层通道光波导和光纤；三维光波导形态多样，常见的如光子晶体结构和波导分支器，可实现复杂的功能。二维和三维光波导结构更紧凑，更易获得较高的腔内光能量密度，易于多功能性集成，具有更高的研究和应用价值。

迄今为止，人们已经利用在多种透明光学材料中实现了光波导的制备，如玻璃、陶瓷、晶体、聚合物等。制备方法多样，主要包括离子注入/辐照、脉冲激光沉积、离子交换技术、聚焦质子直写、外延生长、飞秒激光加工（写入）技术等。其中飞秒激光加工技术是利用超快脉冲激光对透明光学材料进行三维微加工。由于飞秒激光加工技术具有简单灵活、分辨率高、可加工三维形态等优点，近年来受到广泛的关注。本论文主要采用飞秒激光微加工技术在几种透明光学材料中制备光波导结构，由于加工过程中飞秒激光能量集中在焦点处，通过合理的设置飞秒激光的参数（能量、扫描速度、扫描间隔等），可以实现多种形态的光波导制备，同时保留材料的优异性质。

光波导的特点和优势主要表现在较高的光密度，但由此引起的温度变化对波导的性能和寿命有着不可忽视的影响。例如，在波导激光振荡中，泵浦光的吸收

使得波导温度升高，可能造成波导折射率变化，引起波导退化，寿命降低，激光性能下降。因此对光波导工作过程中的温度进行表征具有重要的研究价值。进一步地，通过对波导温度的监控可以大大优化波导的性能及其作为集成光学器件的应用。荧光测温技术是一种通过对材料荧光性质的表征获取温度信息的测量技术，由于其适用范围广、非接触、样品无损耗等优势而受到广泛关注。本论文结合共聚焦荧光显微技术和荧光强度比率法对泵浦下的光波导进行三维高分辨热成像。

本论文的主要内容包括利用飞秒激光写入技术在光学材料中制备通道光波导及波导分支器；对波导在各波段的导波性质进行研究，分析波导的形成机理；利用可饱和吸收体在光波导中实现调 Q 脉冲激光振荡；利用荧光强度比率法对泵浦所致波导温度变化进行研究等。根据实验选用的材料及所制备光波导器件类型的不同，可以将本论文的主要工作归纳如下：

利用飞秒激光写入技术在锗酸铋（BGO）晶体中制备双线型、包层、折射率升高型通道光波导及波导分支器，通过对飞秒激光参数的调试，实现不同的折射率改变，制备多种波导形态。结果表明，双线型光波导位于飞秒激光写入痕迹相夹的内部区域，其中飞秒激光写入痕迹处折射率降低约 1.4×10^{-3}。基于重构的折射率分布，模拟了波导的传输模式，与实验测量的 632.8 nm 波长下模式分布一致，双线型波导支持 TE 和 TM 偏振下的单模传输。经高温退火处理后，飞秒激光单脉冲能量为 2.52 μJ，写入痕迹间隔为 20 μm 的双线型波导的传输损耗降低至 0.5 dB/cm。直径为 100 μm 的 BGO 晶体包层光波导支持 TE 和 TM 偏振下 632.8 nm 波长的多模传输，且对偏振不敏感。经 260℃的退火处理后，波导的传输损耗降低至~2.1 dB/cm。一般地，飞秒激光直写制备折射率升高型光波导较难在晶体中实现，通过对飞秒激光参数的调试，我们在 BGO 晶体中成功制备了折射率升高型通道光波导。端面耦合结果表明，折射率升高型光波导支持中红外波段的导波，且具有偏振不敏感性。波导在 4 μm 波长端面耦合的传输损耗约为 3.5 dB/cm。最后，基于 BGO 晶体折射率升高型光波导，利用飞秒激光写入制备了波导分支器（1 × 2，1 × 3，1 × 4）。通过端面耦合装置研究了其在中红外波段的分支性能。各分支器均支持 4 μm 波长下的单模传输，无偏振效应，且分支比例均匀接近 1:1，分支引起的损耗低至~0.3 dB，表明 BGO 折射率升高型波导分支器可利用于中红外分支器件。

采用飞秒激光写入技术，在掺钕钒酸钇（Nd:YVO_4）晶体中制备双线型、单包层及双包层通道光波导，并利用石墨烯作为可饱和吸收体，实现调 Q 脉冲激光振荡。双线型通道光波导的双线间隔为 20 μm，在 820 nm 连续激光泵浦下，输出 1064.4 nm 激光。相比于 TM 偏振，TE 偏振下的激光性能更优，得益于 TE 偏振下较小的传输损耗：~1.2 dB/cm（TE）和~1.9 dB/cm（TM）。在 1.2 W 的 TE 偏振激光泵浦下，获得最大平均输出功率为 129 mW，最小脉冲宽度为 25.0 ns，最高重复频率为 16.3 MHz，最大单脉冲能量为 8.1 nJ。此外，在直径分别为 42 μm 和 114 μm 的单包层光波导和内/外径为 42/114 μm 的双包层光波导中实现了 1065.2 nm 的调 Q 脉冲激光输出。结果表明，包层光波导具有更对称的形态，更低的损耗，激光性能更优异。且相比于单包层，双包层光波导具有更优异的激光性能，激光阈值仅为 103 mW/123 mW @ TE/TM，在 1.2 W 的 TE 偏振光泵浦下，双包层光波导获得最大平均输出功率为 361 mW，相应的激光脉冲的重复频率为 14.5 MHz，单脉冲能量为 24.9 nJ，脉宽为 31 ns。

利用共聚焦荧光强度比率法对掺钕钇铝石榴石（Nd:YAG）晶体和铒镱共掺磷酸盐玻璃（Er:Yb：phosphate glass）中的飞秒激光微加工表面型通道光波导进行温度表征。在 100 mW，808 nm 激光泵浦下，Nd:YAG 波导内部温度升高约 10℃。实验和理论结果表明，飞秒激光写入痕迹处折射率降低，与空气表面形成一个折射率较低的包层，将光限制在波导内部传输；同时，飞秒激光写入痕迹的热导率降低，形成热阻抗限制热量的扩散，使得温度变化主要发生在波导内部。此外，铒镱共掺磷酸盐玻璃中的荧光分析利用了铒离子的双光子吸收，热敏感度高，又由于磷酸盐玻璃的导热系数低，波导中的温度变化更明显。结合高分辨率多光子吸收荧光成像技术，在铒镱共掺磷酸盐玻璃波导中实现了高分辨率的三维热成像。120 mW，980 nm 的激光泵浦下，铒镱共掺磷酸盐玻璃波导内部升温高达 200℃。为降低波导泵浦中的热效应，我们对泵浦激光进行时间调制，产生方脉冲激光，在不改变脉冲激光峰值功率和脉宽的情况下，增大脉冲间隔，减小相邻脉冲之间的热量累计效应，减小波导温度升高值。理论和实验结果一致地证明了该方法的可行性。

利用飞秒激光加工在 x 切铌酸锂（$LiNbO_3$）晶体中制备包层通道光波导，并研究了波导直径和传输方向对其导波性质的影响。分别采用可见光（0.633 μm）、

近红外（1.064 μm）和中红外（4 μm）作为入射光，利用端面耦合系统使得激光在直径分别为 50 μm 和 110 μm、传输方向分别沿 *y* 轴和 *z* 轴的波导中传输。结果表明，直径为 50 μm 的波导在 4 μm 下为单模传输，其余情况下均为多模传输。直径为 110 μm 沿 *z* 方向传输的波导具有最低的损耗，经过 260℃高温退火一小时后，该波导在 1064 nm 波长下的插入损耗低至 0.5 dB。

关键词：飞秒激光加工；通道光波导；波导分支器；调 Q 脉冲波导激光；共聚焦荧光显微镜；荧光测温技术；波导热成像。

Abstract

Integrated optical circuits (IOC) can realize transmission and processing optical signals in a highly integrated space. IOC has been of great interest since 1960s, when it was firstly proposed, due to the small size, stable performance, low power consumption, functional diversity, et al. Various integrated photonics devices have been developed for different application, nevertheless the basic components remain unchanged, including interconnect, power splitter, waveguide reflector, directional coupler, polarizer, polarization beam splitter, phase modulator, intensity modulator, TE/TM mode converter and frequency shifter. It must be pointed that those functional components are based on the basic element: optical waveguide. Optical waveguide is a structure composed of higher-refractive-index region surrounded by a region with lower refractive index. Taking advantage of the relatively short wavelength, light signal can be confined in a space with volume in a micro or sub-micro scale. Thus, optical density is greatly enhanced inside the waveguide volume.

According to the confinement and propagation of light in three-dimensional space, optical waveguides can be divided into one-dimensional (1D), two-dimensional (1D) and three-dimensional (3D) waveguide. 1D waveguide is also known as planar waveguide. 2D waveguide can be divided into the following types: ridge, channel and buried waveguides. Optical fiber could also be taken as 2D waveguide. 3D waveguides with more complex structures, such as photonic crystal and splitters, can be used for complicated functions. 2D and 3D optical waveguides can confine optical propagation and guidance in higher dimensional scale, reaching higher optical density, which means 2D and 3D optical waveguides have great application prospects in construction of compact functional integrated devices.

So far, optical waveguides have been realized in several transparent optical materials, such as glass, ceramic, crystal and polymer. A few methods have been utilized to fabricate waveguides, including ion implantation/irradiation, pulsed laser deposition, ion-exchange, focused proton beam writing, epitaxial growth and

femtosecond laser micromachining/writing. Femtosecond laser micromachining can realize 3D micro-processing in transparent optical materials by applying ultra-short pulse irradiation. Benefiting from the high resolution, simple and flexible process and 3D micro-processing, femtosecond laser micromachining has been emerged as one of the most efficient techniques for waveguide fabrication. In this thesis, femtosecond laser micromachining is employed to fabricate optical waveguides in transparent dielectric materials. During the processing, the energy of the laser pulse is concentrated in the focus. Different waveguide configurations can be realized by choosing appropriate parameters of the femtosecond laser, such as pulse energy, scanning velocity and separation.

The content mainly includes femtosecond laser micromachining waveguides and waveguide splitters in dielectric materials; investigation of the guiding properties at a wide wavelength region and analysis the formation mechanism of waveguides; Q-switched pulse laser generation in optical waveguides based on saturable absorber; using luminescence intensity ratio to detect pump-induced thermal effect in waveguide volume. According to different dielectric materials and different types of optical waveguide devices, the main work of this thesis can be summarized as follows:

We report on the fabrication of dual-line waveguides, depressed cladding waveguides, buried channel waveguides with increased refractive index femtosecond inscribed filaments, and waveguide splitters in BGO crystals by femtosecond laser micromachining. The dual-line waveguides are located at the core of two femtosecond laser filaments with a refractive index decrease of 1.4×10^{-3}. Based on the reconstructed 2D refractive index profile of the waveguide cross section, the propagation modes of the BGO dual-line waveguides are calculated. Both the simulation and experimental results show that the dual-line waveguide supports single-mode propagation along TE and TM polarizations at the wavelength of 632.8 nm. Thermal annealing treatment is effective to reduce the propagation loss of dual-line waveguides to 0.5 dB/cm. Circle cladding waveguide with a diameter of 100 μm supports multi-mode propagation along both TE and TM polarization at 632.8 nm

and is insensitive to polarization. With thermal annealing at 260℃, the propagation loss of the cladding waveguide is reduced to 2.1 dB/cm. It is common to fabricate waveguides with increased refractive index in glass rather than crystal. Waveguides with increased refractive index have only been reported in a few crystals, including $LiNbO_3$, Nd:YCOB and ZnSe, with limitations in stability and polarization. By carefully choosing the fabrication parameter, waveguides with increased refractive index are realized in BGO crystal by femtosecond laser writing. The end-coupling experiment reveals that waveguides support polarization insensitive guidance at mid-infrared region. The propagation loss of the waveguide at 4 μm is estimated to be ~3.5 dB/cm. Then, the same femtosecond laser parameters are utilized to construct waveguide splitters with increased refractive index filaments. The 2D (1 × 2) and 3D (1 × 3，1 × 4) waveguide splitters support polarization insensitive guidance at 4 μm, and the near-field intensity mode are single-modes. The intensity splitting ratio of the output arms are close to 1:1. The splitting losses are as low as 0.3 dB. The results show the promising capability of direct femtosecond laser written waveguide splitters in BGO crystal for MIR applications.

We report on the passively Q-switched lasers in femtosecond laser written dual-line, single- and double-cladding waveguides in Nd:YVO_4 crystals. Using graphene as the saturable absorber, passively Q-switched waveguide laser operations were achieved. The separation of the dual-line waveguide is 20 μm. Under 820 nm CW laser pump, laser oscillations at the wavelength of 1064.4 nm have been achieved in the dual-line waveguide. The performance along TE polarization is superior to that along TM, which could contribute to the propagation loss of the dual-line waveguide: ~1.2 and ~1.9 dB/cm along TE and TM polarizations. At the pump power of 1.2 W, the maximum average output laser power is achieved as 129 mW, corresponding to the minimum pulse width of 25.0 ns, the highest repetition rate of 16.3 MHz and the highest single pulse energy of 8.1 nJ. Q-switched pulse laser generation is also achieved at the single-cladding waveguide with diameters of 42 or 114 μm and double-cladding waveguide with inner/external diameters of 42/114 μm. The wavelength of the generated laser is 1065.2 nm. The cladding waveguides possess

more symmetrical shape, lower loss and better laser performance. Especially, the double-cladding waveguide is superior to the single-cladding waveguide, as the outer cladding provides large pump area and single-mode propagation is achieved by inner cladding confinement. The maximum waveguide laser output power is ~361 mW with a lasing threshold of 103 mW along TE polarization, meanwhile, the repetition rate of the pulsed laser could be tuned and raised up to 14.5 MHz corresponding to single-pulse energy of 24.9 nJ and pulse width of 31 ns.

We have demonstrated how luminescence thermometry, in combination with high resolution confocal fluorescence imaging, constitutes a contact-free technique for intra-waveguide thermal imaging. Femtosecond laser writing is utilized to fabricate channel waveguides in Nd:YAG crystal and Er:Yb:phosphate glass. For 800 nm injected laser powers close to 100 mW, intra-waveguide laser-induced heating of a few degrees have been experimentally found in Nd:YAG waveguide. Both the theory and experimental results show that: i) the refractive index of femtosecond laser inscribed filaments decreases, thus the light is confined in the waveguide core; ii) femtosecond laser induce filaments are also characterized by a reduced thermal conductivity, acting as the thermal barriers, so thermal loading is mainly confined at the waveguide volumes.

The luminescence measurement of the Er:Yb:phosphate glass waveguide is realized by the two-photon excited luminescence of Erbium ions. The thermal effect of the waveguide is much obvious as the high thermal sensitivity and low glass thermal conductivity. In combination with high resolution multiphoton fluorescence imaging, high resolution 3D thermal imaging of Er:Yb:phosphate glass waveguide is obtained. Under 120 mW, 980 nm CW laser pump, the temperature increments at waveguide volume is as large as 200°C, which means that the laser induced thermal loading cannot be neglected at all. To reduce the thermal effect, time modulation is applied to change the pump laser to a square pulse laser, with a fixed pulse width of 2 ms and fixed peak power of 60 mW. Experimental and numerical simulations have concluded that intra-waveguide temperature increment can be reduced by increasing the pulse separation, as the heat accumulation between neighbor pulses can be

minimized.

We fabricated cladding waveguides in $LiNbO_3$ crystal by using femtosecond laser micromachining, and studied the effect of propagation direction and diameter on the guiding property. The cladding structures with diameter of 50 μm and 110 μm support guidance along both extraordinary index (n_e) and ordinary index (n_o) polarizations at wavelengths of 0.633 μm, 1.064 μm and 4 μm. At the wavelength of 4 μm, single modes are achieved for the cladding waveguides with diameter of 50 μm. After thermal annealing, the insertion loss of the cladding waveguide with a diameter of 110 μm (along *z* axis) was reduced to 0.5 dB.

Keywords: Femtosecond laser micromachining; Channel optical waveguide; Waveguide splitter; Q-switched waveguide laser; Confocal luminescence microscopy; Luminescence thermal imaging; Waveguide thermal imaging.

符号说明

n：介质的折射率

h：普朗克常数

k_B：玻尔兹曼常数

t：时间

α：损耗系数

θ：入射角

λ：波长

ω：频率

D：透过率

I：荧光强度

L：长度

T：温度

P：光强

R：荧光强度比率

S：热敏度

TE：光波中的横电场

TM：光波中的横磁场

第一章 绪 论

二十世纪末，人类迈入信息时代，信息技术的发展改变了人们的生活和工作方式，信息大爆炸的今天，信息的采集、存储、处理和传输等成了发展的关键。光通信作为信息时代的重要技术，是网络和电信网络的基石[1]。1880 年 A. G. Bell 发明了“光电话”——用太阳光搭载信息来传播声音，开启了光通信的大门。1960 年 T. H. Maiman 成功研制了世界第一台激光器[2]——红宝石固态激光器，随后，氦氖激光器、半导体激光器、化学激光器、燃料激光器等相继出现，成为研究热点，光通信技术随之迅速发展，激光物理学、导波光学、非线性光学等一系列交叉学科涌现，大大推动了军事、医学、农业、通讯和科学技术等领域的进步[3-6]。传统光学系统由于体积大、损耗高、稳定性差已无法满足科技发展的要求，随着激光的广泛应用和发展，集成光学迅速发展为一门新兴技术。1969 年，美国贝尔实验室的 S. E. Miller[7]提出集成光学概念。集成光学[8-13]通过集成化的光学器件，实现激光激励、耦合、光开关、光分束、频率转换等功能，对光信号进行处理和传输。集成光学系统具有体积小、重量轻、抗电磁干扰、信息量大、稳定性好等优点[14]，在光通讯、光学测量和传感器等领域有重要的研究价值和应用前景。

集成光学的基本元件为光波导[15-18]，是一个被折射率低的区域所包裹的折射率高的区域，由于全反射原理，光被限制在折射率高的介质中传输，该区域尺寸一般在微米或纳米量级。在光波导内可以达到较高的光密度，可以有效的延长光信号的传输距离。结合介质的材料特性，光波导可以实现多种功能，如耦合、开关、频率转换、分束等，而这些功能性波导元件集成在一个光子芯片上，形成集成光路。光波导的品质直接决定了集成光路的优劣，因此设计和优化光波导结构一直是集成光学的研究重点。迄今为止，科学家利用多种技术在透明光学材料中制备了光波导结构，根据波导的形态主要可以分为以下三类：

一、平面光波导的制备。利用离子注入/辐照[19-22]、离子交换[23,24]、金属离子扩散[25,26]、薄膜沉积[27-29]等方法在介质表面形成一层折射率较高的平面区域，将光限制在平面内传输；

二、通道光波导的制备可以在平面光波导制备的基础上实现，如使用光刻掩

膜[30,31]、金属掩膜[32]等技术在介质表面形成一个通道，而后使用平面波导制备方法形成表面型通道光波导，又可以对已经制备的平面光波导采取飞秒激光烧蚀[33]、金刚石刀切割[34]或化学腐蚀[35]等方法形成脊型或条形通道光波导。另外，可以通过飞秒激光加工[36]或聚焦质子束直写[37]等方法直接在样品中引入折射率变化，形成条形通道光波导。相对于平面光波导，通道型光波导在两个维度对光进行限制，可以获得更高的光密度和更紧凑的结构；

三、三维光波导的制备。聚焦质子束写入和飞秒激光加工等三维加工方法可以在介质中直接写入分支器、耦合器等三维光波导结构，实现更复杂的功能[38,39]。

本文主要工作采用飞秒激光加工（写入）方法制备通道及三维光波导结构。飞秒激光加工技术是一门新兴的技术[40-43]，利用具有高峰值功率、短脉宽的飞秒激光脉冲对材料进行改性。1987 年，两篇报道引起了科学家的广泛关注，并促使飞秒激光加工技术快速的发展，首先 R. Srinivasan 等人[44]报道了利用飞秒脉冲激光切割有机玻璃，随后 S. Küper 和 M. Stuke[45]使用 300 fs 紫外脉冲激光烧蚀有机玻璃（PMMA），过程中周围区域都没有受到热效应的影响。迄今为止，飞秒激光已被广泛应用玻璃、陶瓷、晶体、聚合物、生物组织等材料的加工和研究[46-50]，对于医学、生物学、材料加工等领域的发展具有重要的影响。由于飞秒激光产生的热量聚集在焦点处通过非线性吸收被材料吸收，无热效应，附近区域受影响较小[51]，材料自身性质不受破坏，可适用于生物组织[52]和脆性材料[53]（如半导体、绝缘体）等；另外，多光子吸收过程使得飞秒激光可以对透明光学材料进行三维定位加工[54-56]；2001 年，S. Kaeata 等人利用多光子吸收中的非线性效应和阈值效应的共同作用[57]，使用波长为 780 nm 的飞秒激光制备了空间分辨率为 18 nm 的结构，突破衍射极限[58]；此外，飞秒激光加工还具有无污染、时间短等优点。

1996 年，K. M. Davis[59]首次将飞秒激光加工技术利用在玻璃中制备了光波导结构，随后，飞秒激光加工广泛应用于各种透明光学材料中制备不同形态的通道和三维光波导结构[60]。由于材料和飞秒激光参数的不同，飞秒激光写入区域的折射率变化不同：一类为折射率升高型，写入区域折射率升高直接形成波导，这类波导常见于玻璃中[61,62]，而晶体结构往往被飞秒激光能量破坏，难以形成折

射率升高型光波导，目前在 $LiNbO_3$[63]、Nd:YCOB[64]、ZnSe[65]晶体和本文所使用的 $Bi_4Ge_3O_{12}$ 晶体[66]中有此类波导的报道，折射率升高型光波导有利于直接在材料中进行三维加工；另一类飞秒写入痕迹处折射率降低，周围区域由于应力挤压作用折射率略有升高，利用两条相互平行的写入痕迹可以形成双线型通道光波导，波导位于两条写入痕迹之间。这类光波导易加工，但导波性质受到各项异性的写入痕迹影响而具有偏振各向异性[67,68]。另外，也可利用多条折射率降低的写入痕迹组成一个封闭的包层，波导位于包层内部。包层光波导适用材料广泛，结构本身无偏振异性，适用于相位匹配、频率转换机制，通过对包层形状和大小的设计可用于波导——光纤耦合[69,70]。

1961 年 E. Snitzer 报道了氧化钕（Nd_2O_3）掺杂玻璃材料的圆柱形波导激光[71]，开拓了波导激光领域。波导激光[72,73]作为光波导结构的一个重要应用，可使集成光路成为一个有源系统。通过在激光增益介质中制备光波导结构，将泵浦光耦合至波导中，波导作为谐振腔产生激光振荡。波导激光与传统激光光源相比，体积小、稳定性好。光波导作为谐振腔，腔内光能量密度远远高于体材料，且光波导和泵浦光耦合效率高，大大降低了激光振荡的阈值，有利于获得高功率的激光输出[74,75]。波导激光既可以作为单独的激光器，也可以和其它光学元件结合制备多功能器件[76,77]。

影响光波导性能的一个重要因素即温度，在光信号的处理、传输和存储过程中，温度变化导致的光波导结构变化对系统性能会有破坏性的作用[78-81]。例如，在激光泵浦过程中，光波导相对于材料本身具有较低的泵浦阈值和较高的效率等优势，但同时热效应也会影响输出激光的性能，例如谐振腔的长度变化、波导折射率变化、输出光的光束质量、激光的稳定输出及输出激光的功率及效率等。另外，由于泵浦引起的光波导温度梯度，产生应力场，会影响波导的性能和寿命。再如，利用非线性晶体光波导实现频率转换时，二次谐波的产生与相位匹配条件密切相关，而温度的变化对相位匹配的影响明显。测量和调控光波导在工作中的温度变化是一个至关紧要的任务。介于波导的维纳尺寸和结构特点，在对其进行温度测量的过程中，要求无接触、对波导器件无损伤及可在三维空间精细测量。传统的温度传感器，如热膨胀式温度传感器、电热阻/电热偶温度传感器及红外测温仪等无法满足此要求[82]。荧光测温技术[83]可以同时满足以上要求，根据稀

土离子掺杂介质的荧光特性，结合高分辨率的共聚焦荧光显微镜，已经实现对纳米颗粒、荧光分子等材料的温度表征。荧光测温技术有望应用于波导温度的测量，对光波导工作过程中的温度变化进行表征。

本论文工作主要目的是利用飞秒激光加工技术，在多种透明光学材料中制备多种形态、尺寸及功能的通道光波导，对其光学性能进行研究。主要研究内容包括导波特性、荧光特性、激光性能及波导热成像。研究结果表明飞秒激光加工技术可用于制备性能优异的多功能性通道光波导及波导分支器，为其在集成光路中的应用提供了理论和实际依据。全文共包括七章，可分为六个部分：

第一部分即第二章，对研究工作中涉及到的基本理论知识、实验和模拟方法进行了介绍。主要内容包括：光波导的结构；飞秒激光写入制备光波导技术的原理和实验装置；光波导技术，包括光波导实验方法，如端面耦合技术、传输损耗测量方等，并对光束传播法——模拟光在波导中的传输，进行了介绍；波导激光的实验方法、激光性能的几个重要参数及激光调 Q 技术；荧光分析和共聚焦荧光显微镜技术；最后介绍了荧光的温度敏感性，及利用荧光强度比率表征温度的方法。

第二部分即第三章，主要研究了利用飞秒激光写入锗酸铋（BGO）晶体制备多种形态的双线型和包层通道光波导及波导分支器，并研究其导波特性。具体内容包括：

I. 利用飞秒激光写入在 BGO 晶体中制备双线型光波导。飞秒激光写入痕迹处折射率降低约~10^{-3} 数量级，由于应力挤压作用附近区域折射率升高约~10^{-4}，双线中间区域形成波导。通过端面耦合技术对于双线型光波导在 632.8 nm 波长各偏振下的导波性质进行了研究，并使用高温退火处理优化波导的性能；

II. 包层光波导的制备过程中，飞秒激光写入速度较快为 500 μm/s，写入痕迹较短，痕迹间隔为 3 μm。写入痕迹周围区域受应力影响较小，多条写入痕迹组成一个准连续的折射率降低的包层边界，波导位于该波包层内部。对 BGO 晶体包层通道光波导在 632.8 nm 下的导波性质进行了研究，并使用 260℃高温退火一小时优化波导的传输性能。

III. 在晶体中制备折射率升高型光波导对飞秒激光的参数要求较高，目前只在少数几种晶体中制备成功。通过实验参数调试，我们利用较低的飞秒激光单脉冲功率结合多重扫描技术，在 BGO 晶体中写入具有对称的矩形截面的折射率升高型光波导。通过端面耦合技术对该波导在中红外波段的传输特性进行了研究。

IV. 利用上节所制备的折射率升高型波导结构在 BGO 晶体中制备了波导分支器（1 × 2，1 × 3，1 × 4）。利用端面耦合系统研究了分支器的导波和分支性能，并通过数值计算模拟了中红外激光在波导分支器中的传输。

第三部分即第四章，研究对象为激光晶体掺钕钒酸钇（Nd:YVO_4）晶体。利用飞秒激光加工制备双线型、单包层及双包层光波导，并研究了其传输特性和调 Q 脉冲激光性能。具体内容如下：

I. 飞秒激光写入 Nd:YVO_4 双线型光波导，双线间隔为 20 μm。石墨烯作为可饱和吸收体，具有吸收带宽、损伤阈值高、调制深度大等优势。我们采用石墨烯作为可饱和吸收体，在 820 nm 连续激光泵浦下，实现 1064.4 nm 调 Q 脉冲激光振荡。导波性能测试表明，TE 偏振下损耗较小，激光性能更优异。

II. 对飞秒激光写入 Nd:YVO_4 晶体圆形单包层和多包层光波导也进行了激光泵浦，实现调 Q 脉冲激光输出。包层光波导激光泵浦实验表明，双包层光波导有效吸收截面面积更大，相比于同等尺寸的单包层波导具有更低的激光阈值，更高的输出功率，激光性能更优异。

第四部分即第五章，研究对象为飞秒激光加工制备的表面型通道光波导，包括掺钕钇铝石榴石（Nd:YAG）晶体和铒镱共掺磷酸盐玻璃（Er:Yb:phosphate glass）。主要利用共聚焦荧光强度比率法，对波导的泵浦热效应进行了研究，具体内容如下：

I. 利用飞秒激光加工在 Nd:YAG 晶体中制备了表面型通道光波导。使用 800 nm 的光纤激光与波导进行端面耦合，利用高功率紫外固化系统将光纤和样品集成在一个玻片上，然后采用共聚焦荧光显微镜测量波导的荧光图像，选用 Nd^{3+}离子在 $^4F_{3/2}\rightarrow{}^4I_{9/2}$ 能级跃迁产生的 938 nm 和 945 nm 两条发射线作为温度探针，在“泵浦+探测”系统下利用荧光强度比率法

测量波导温度的变化。理论和实验结果表明，飞秒激光写入痕迹折射率降低，热导率降低，泵浦引起的热效应使得波导内部温度升高，波导外部温度基本不变。我们利用热敏上转换纳米颗粒 Er:Yb:LaF_3 对波导表面的温度进行了测量验证。

II. 在铒镱共掺磷酸盐玻璃中同样制备表面型通道光波导，利用 Er^{3+}离子的双光子吸收，采用“泵浦+探测”系统获得波导的高分辨率三维微荧光图谱。利用 Er^{3+}离子在 980 nm 激发下的 525 nm 和 545 nm 发射线的荧光强度比率获得波导的热成像。由于玻璃的导热系数较小，波导的结构紧凑、光密度高，所以泵浦引起的波导温度升高值高达 200℃。为降低泵浦引起的热效应，对泵浦光采用时间调制法。理论和实验结果表明，泵浦光的时间调制可以降低热累计效应，有效的降低波导的温度。

第五部分即第六章，利用飞秒激光写入 *x* 切铌酸锂（$LiNbO_3$）晶体，制备了四条圆形包层光波导，直径分别为 50 μm 和 110 μm，传输方向分别沿晶体 *y* 轴和 *z* 轴。在 TE 或 TM 偏振下，入射光在波导中的偏振沿晶体的寻常光（n_o）或异常光（n_e）方向，晶体的双折射效应导致波导的导波性能不同。利用端面耦合系统对波导在可见光（0.633 μm）、近红外（1.064 μm）和中红外（4 μm）的导波性能进行了表征，并使用高温退火优化波导性能。

第六部分即第七章，对本论文研究工作和创新点进行总结。

参考文献

1. M. L. Calvo and V. Lakshminarayanan, Optical Waveguides: From Theory to Applied Technologies (CRC Press, 2007).
2. T. H. Maiman, Nature **187**, 493–494 (1960).
3. 李福利. 高等激光物理学, 高等教育出版社，2006.
4. K. Okamoto, Fundamentals of Optical Waveguides (Elsevier, 2005).
5. 曹庄琪. 导波光学，科学出版社，2007.
6. R. W. Boyd, Nonlinear Opics, (Elsevier, 2008).
7. S. E. Miller, Bell System Technical Journal **48**, 2059–2069 (1969).
8. T. Tamir, Integrated Optics (Springer-Verlage, 1975).
9. 陈益新. 集成光学, 上海交通大学出版社, 1985.
10. [日] 西原 浩, 春明正光, 栖原敏明. 集成光路, 科学出版社, 2004.
11. B. E. A. Saleh and M. C. Teich, Fundamentals of Photonics (John Wiley & Sons, 2007).
12. G. Lifante, Integrated Photonics: Fundamentals (John Wiley & Sons, 2003).
13. A. Yariv, P. Yeh, Photonics Optical Electronics in Modern Communications,6th ed. (Oxford University Press, 2006)
14. R. G. Hunsperger, Integrated Optics: Theroy and Technology (Springer, 2009).
15. H. Nishihara, M. Haruna, and T. Suhara, Optical Integrated Circuits (Ohmasha, 1989).
16. E. J. Murphy, Integrated Optical Circuits and Components (Marcel Dekker, 1999).
17. Z. Cao, Guided Wave Optics (Science, 2007).
18. B. P. Pal, Guided Wave Optical Components and Devices: Basics, Technology, and Applications (Elsevier, 2006).
19. P. D. Townsend, P. J. Chandler, and L. Zhang, Optical Effects of Ion Implantation (Cambridge University Press, 1994).
20. F. Chen, laser Photon. Rev. **6**, 622–640 (2012).
21. Y. Y. Ren, F. Chen, Q. M. Lu, and H. J. Ma, Appl. Opt. **49**, 2085–2089 (2010).
22. G. B. Montanari, P. De Nicola, S. Sugliani, A. Menin, A. Parini, A. Nubile, G.

Bellanca, M. Chiarini, M. Bianconi, and G. G. Bentini, Opt. Express **20**, 4444–4453 (2012).

23. A. Tervonen, B. R. West, and S. Honkanen, Opt. Eng. **50**, 071107 (2011).
24. P. Mazzoldi and C. Sada, Mat. Sci. Eng. B **149**, 112–117 (2008).
25. V. V. Atuchin, K. K. Ziling, and D. P. Shipilova, Sov. J. Quantum Electron. **14**, 671–674 (1984).
26. J. Hukriede, D. Kip, and E. Krätzig, Appl. Phys. B **72**, 749–753 (2001).
27. P. K. Tien, R. Ulrich, and R. J. Martin, Appl. Phys. Lett. **14**, 291–294 (1969).
28. K. M. Wang, B. R. Shi, N. Cue, Y. Y. Zhu, F. R. Xiao, F. Lu, W. Li, and Y. G. Liu, Appl. Phys. Lett. **73**, 1020–1022 (1998).
29. T. Yamashiki and K. Tsuda, Opt. Lett. **28**, 316–318 (2003).
30. F. Chen, Crit. Rev. Solid State Mater. Sci. **33**, 165–182 (2008).
31. Y. Tan, F. Chen, M. Stepic, V. Shandarov, and D. Kip, Opt. Express **16**, 10465–10470 (2008).
32. Y. Yao, Y. Jia, F. Chen, Sh. Akhmadaliev, and S. Zhou, Appl. Opt. **53**, 195–199 (2014).
33. Y. Cheng, J. Lv, S. Akhmadaliev, I. Hernández-Palmero, C. Romero, J. R. Vázquez de Aldana, S. Zhou, and F. Chen, Opt. Laser Technol. **72**, 100–103 (2015).
34. T. Nishikawa, A. Ozawa, Y. Nishida, M. Asobe, F. L. Hong, and T. W. Hänsch, Opt. Express **17**, 17792–17800 (2009).
35. D. Choudhury, A. Rodenas, L. Paterson, F. Díaz, D. Jaque, and A. K. Kar, Appl. Phys. Lett., **103**, 041101 (2013).
36. M. Xu, R. He, S. Sun, J. R. Vázquez de Aldana, and F. Chen, Phys. Status Solidi RRL **7**, 1014–1017 (2013).
37. T. C. Sum, A. A. Bettiol, J. A. van Kan, F. Watt, E. Y. B. Pun and K. K. Tung, Appl. Phys. Lett. **83**, 1707–1709 (2003).
38. A. Arriola, S. Gross, N. Jovanovic, N. Charles, P. G. Tuthill, S. M. Olaizola, A. Fuerbach, and M. J. Withford, Opt. Express **21**, 2978–2986 (2013).

39. S.K. Vanga and A.A. Bettiol, Nucl. Instrum. Methods Phys. Res. Sect. B **306**, 281–283 (2013).
40. R. Osellame, G. Cerullo, and R. Ramponi, Femtosecond Laser Micromachining: Photonic and Microfluidic Devices in Transparent Materials (Springer, 2012).
41. D. Choudhury, J. R. Macdonald, and A. K. Kar, Laser Photonics Rev. **8**, 827–846 (2014).
42. R. R. Gattass and E. Mazur, Nature Photon. **2**, 219–225 (2008).
43. K. Sugioka and Y. Cheng, Light-Sci. Appl. **3**, e149 (2014).
44. R. Srinivasan, E. Sutcliffe, and B. Braren, Appl. Phys. Lett. **51**, 1285–1287 (1987).
45. S. Küper and M. Stuke, Appl. Phys. B **44**,199–204 (1987).
46. L. B. Fletcher, J. J. Witcher, N. Troy, S. T. Reis, R. K. Brow, and D. M. Krol, Opt. Express **19**, 7929–7936 (2011).
47. A. Okhrimchuk, V. Mezentsev, A. Shestakov, and I. Bennion, Opt. Express **20**, 3832–3843 (2012).
48. G. A. Torchia, A. Rodenas, A. Benayas, E. Cantelar, L. Roso, and D. Jaque, Appl. Phys. Lett. **92**, 111103 (2008).
49. F. Chen and J. R. Vázquez de Aldana, Laser Photonics Rev. DOI 10.1117/2.1201507.006006.
50. S. Gross, M. Alberich, A. Arriola, M. J. Withford, and A. Fuerbach, Opt. Lett. **38**, 1872–1874 (2013).
51. C. Momma, B. N. Chichkov, S. Nolte, F. von Alvensleben, A. Tünnermann A, H. Welling, and B. Wellegehausen, Opt. Commun. **129**, 134–142 (1996).
52. M. F. Yanik, H. Cinar, H. Nese Cinar, A. D. Chisholm, Y. Jin, and A. Ben-Yakar, Nature **432**, 822 (2004).
53. N. Bärsch, K. Körber, A. Ostendorf, and K. H. Tönshoff, Appl. Phys. A **77**, 237–242 (2003).
54. E. N. Glezer, M. Milosavljevic, L. Huang, R. J. Finlay, T. H. Her, J. P. Callan, and E. Mazur, Opt. Lett. **21**, 2023–2025 (1996).
55. W. Watanabe, S. Sowa, T. Tamaki, K. Itoh, and J. Nishii, Jpn. J. Appl. Phys. **45**,

L765–L767 (2006).

56. Y. Hanada, K. Sugioka, and K. Midorikawa, Opt. Express **18**, 446–450 (2010).
57. S. Kawata, H. B. Sun, T. Tanaka, and K. Takada, Nature **412**, 697–698 (2001).
58. H. B. Sun, S. Matsuo, and H. Misawa, Appl. Phys. Lett. **74**,786–788 (1999).
59. K. M. Davis, K. Miura, N. Sugimoto, and K. Hirao, Opt. Lett. **21**, 1729–1731 (1996).
60. F. Chen and J. R. Vázquez de Aldana, Laser Photonics Rev. **8**, 251–275 (2014).
61. G. Salamu, F. Jipa, M. Zamfirescu, and N. Pavel, Opt. Mater. Express **4**, 790–797 (2014).
62. A. Zoubir, C. Lopez, M. Richardson, and K. Richardson, Opt. Lett. **29**, 1840–1842 (2004).
63. R. Osellame, M. Lobino, N. Chiodo, M. Marangoni, G. Cerullo, R. Ramponi, H. T. Bookey, R. R. Thomson, N. D. Psaila, and A. K. Kar, Appl. Phys. Lett. **90**, 241107 (2007).
64. A. Rodenas and A. K. Kar, Opt. Express **19**, 17820–17833 (2011).
65. J. R. Macdonald, R. R. Thomson, S. J. Beecher, N. D. Psaila, H. T. Bookey, and A. K. Kar, Opt. Lett. **35**, 4036–4038 (2010).
66. R. He, I. Hernández-Palmero, C. Romero, J. R. Vázquez de Aldana, and F. Chen, Opt. Express **22**, 31293–31298 (2014).
67. A. Ródenas, G. Torchia, G. Lifante, E. Cantelar, J. Lamela, F. Jaque, and L. Roso, Appl. Phys. B **95**, 85–96 (2009).
68. C. Zhang, N. Dong, J. Yang, F. Chen, J. R. Vázquez de Aldana, and Q. Lu, Opt. Express **19**, 12503–12508 (2011)
69. A. G. Okhrimchuk, A. V. Shestakov, I. Khrushchev, and J. Mitchell, Opt. Lett. **37**, 2248–2250 (2005).
70. H. L. Liu, Y. C. Jia, J. R. Vázquez de Aldana, D. Jaque, and F. Chen, Opt. Express **20**, 18620–18629 (2012).
71. E. Snitzer, Phys. Rev. Lett. **7**, 444–446 (1961).
72. C. Crivas, Prog. Quant. Electron. **35**, 159-239 (2011).

73. E. Cantelar, D. Jaque, and G. Lifante, Opt. Mater. **34**, 555–571 (2012).

74. J. I. Mackenzie IEEE J. Sel. Top. Quant. **13**, 626–637 (2007).

75. D. Zhou, L. Wei, B. Dong, and W. Liu, IEEE Photon. Technol. Lett. **22**, 9–11 (2010).

76. Z. P. Sun, T. Hasan, F. Torrisi, D. Popa, G. Privitera, F. Q. Wang, F. Bonaccorso, D. M. Basko, and A. C. Ferrari, ACS nano **4**, 803–810 (2010).

77. G. D. Valle, R. Osellame, G. Galzerano, N. Chiodo, G. Cerullo, P. Laporta, and O. Svelto, Appl. Phys. Lett. **89**, 231115 (2006).

78. W. Koechner, Appl. Opt. **9**, 2548–2553 (1970).

79. A. J. Glass and A. H. Guenther, Appl. Opt. **12**, 637–649 (1973).

80. M. B. Bavil and E. Safari, J. Mech. Sci. Technol. **28**, 3231–3236 (2014).

81. G. Schreiber, H. Suche, Y. L. Lee, W. Grundkötter, V. Quiring, R. Ricken, and W. Sohler, Appl. Phys. B **73**, 501–504 (2014).

82. H. M. Pollock and A. Hammiche, J. Phys. D **34**, R23 (2001).

83. D. Jaque and F. Vetrone, Nanoscale **4**, 4301–4326 (2012).

第二章 理论基础和实验方法

本章对本文工作所涉及的基本理论、实验方法、模拟计算、数据分析等进行了简要的阐述，主要包括：光波导基本理论、飞秒激光加工技术、光波导表征技术、波导激光理论、共聚焦荧光显微镜技术和荧光测温技术。

光波导可以将光限制在较小的区域（微米至亚微米）传输，根据其对光的传输维度限制，可以将光波导分为平面光波导（一维），通道光波导（二维）及分支光波导（三维）。其中通道和分支光波导的波导光密度相对于平面光波导有明显提升，是本文的研究重点。

光波导有多种制备方法，本文主要采用飞秒激光加工（写入）技术，利用超快脉冲激光的高分辨率、高功率密度等特性进行光波导的制备。飞秒激光加工技术具有制备便捷、可调控性强、可实现三维精细加工等优点。

对于光波导的特性表征，本文主要采用光波导端面耦合技术、折射率分布重构、数值模拟、损耗测量和计算等方法。通过端面耦合技术实现波导光激励，测量光波导的近场光强分布和功率损耗等导波特性。模拟波导的折射率用来解释波导的形成机理，并通过对照模拟与实验的激光在波导中的传输与分布，验证光波导的结构组成，为最优化实验参数提供理论依据。

光波导在集成光路中既可以作为无源器件，也可以作为有源器件对光进行调制，例如波导激光具有高功率、低阈值的优势。本文介绍了波导激光的机理，及采用石墨烯作为可饱和吸收体实现调 Q 脉冲激光的机制等相关理论。

光学元件的热稳定性是衡量其性能优劣的标准之一，对于光波导而言，由于光在腔内传输时达到高能量密度，由材料的吸收引起的热效应更显著，因此对波导性能的影响更明显。测量并调控光波导结构中的温度分布有利于理解光波导耦合和泵浦机理，优化光波导性能及提高激光、倍频光功率效率等。我们采用“泵浦+探测”系统测量光波导的热效应，本章介绍了该系统所使用的荧光分析方法、共聚焦荧光显微镜技术及荧光测温技术。

2.1 光波导的结构

光波导是集成光路中用于限制和传输光的基本元件，是由折射率较高的介质被折射率较低的介质所包裹而形成的结构[1-5]。基于全反射原理，光波导可以将光限制在微米甚至亚微米尺度内传输，达到较高的光能量密度。

根据对光的传输维度的限制，可以将光波导分为平面光波导（一维），通道光波导（二维）及分支光波导（三维），如图 2.1.1 所示。平面光波导只能对传输光的一个维度进行限制，而在另一个维度会产生发散，难以满足集成光路的要求；而通道光波导实现了在二维空间中对光进行限制和调控，有利于获得更高的光能量密度及元件的微型化和集成化；分支光波导则可对光进行三维调控，实现更复杂的功能，应用更广泛。本论文主要讨论二维和三维光波导。

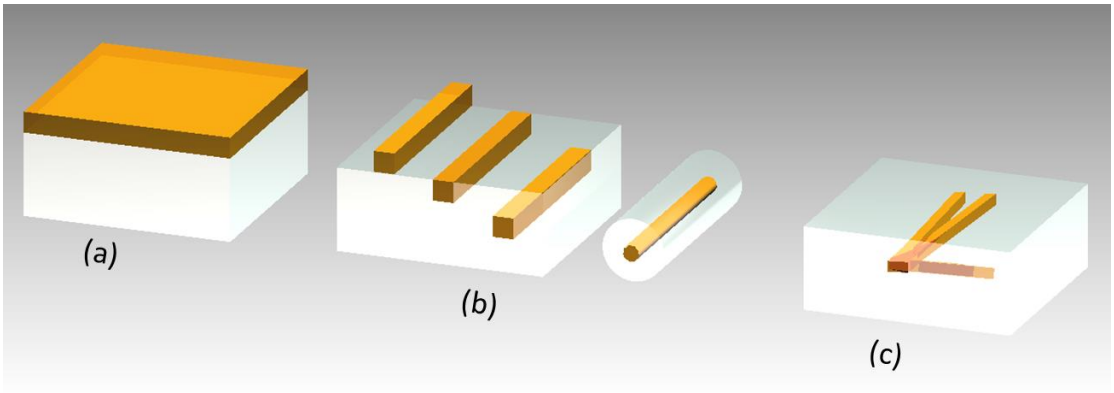

图 2.1.1 光波导结构示意图：（a）一维平面光波导；（b）二维通道光波导；（c）三维分支光波导

2.2 飞秒激光写入制备光波导技术

光波导的制备方法主要包括以下几类：一类是载能离子束辐照[6-8]、离子交换[9-11]、薄膜沉积[12-15]等方法制备一维平面光波导；第二类是基于平面波导的制备，结合预处理（如光刻掩膜、金属掩膜）[16-18]或后加工（如烧蚀、机械刻蚀、化学腐蚀）[19-25]制备二维通道光波导；另一类是直接在介质内部或表面进行加工引起折射率变化，制备二维通道或三维分支光波导，例如飞秒激光加工（写入）[26-28]、聚焦质子束写入[29-31]等。表 2.2.1 列举了常用通道光波导的制备方法及形态。

表 2.2.1 通道光波导的常用制备方法

<table>
<tr><th>样品预处理</th><th>平面光波导制备法</th><th>表面型通道光波导</th></tr>
<tr><td>光刻掩膜
金属掩膜</td><td>离子注入
离子交换
热扩散</td><td rowspan="2"> 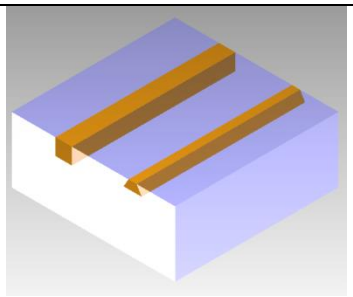 </td></tr>
<tr><th>制备平面光波导</th><th>样品后加工</th></tr>
<tr><td>离子注入
离子交换
热扩散</td><td>金刚石刀切割
飞秒激光光刻蚀
化学腐蚀</td><td> 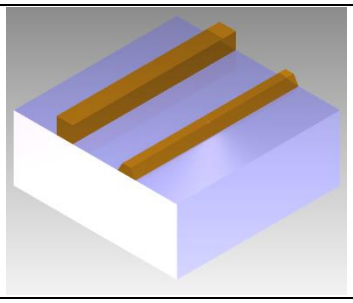 </td></tr>
<tr><th colspan="2">直接制备</th><th>表面型或埋层通道光波导</th></tr>
<tr><td colspan="2">飞秒激光写入
聚焦质子束直写</td><td> 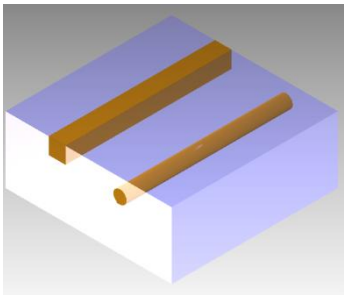 </td></tr>
</table>

1996 年，K. M. Davis 等人首次报道了利用飞秒激光脉冲在透明玻璃中写入光波导结构[32]。随后，飞秒激光加工技术被广泛应用于玻璃、晶体、陶瓷、高分子聚合物等透明光学材料中，制备性能优异的光波导及其它光学元件。飞秒激光加工技术的优势主要体现在以下几个方面：

1) 加工便捷。飞秒激光将技术不需要掩膜或其它预处理、后加工技术，通过程序控制三维电动平台的移动，直接在透明材料中引入折射率变化，实现光波导、分支器等复杂光学元件的一步制备；
2) 适用材料广泛。通过调节飞秒激光的工作参数（如波长、偏振、脉冲能量、脉冲频率、扫描速率等）即可在多种透明材料上进行加工；
3) 精细微纳加工。飞秒激光能量集中在焦点处，焦点的大小控制在微米甚至纳米尺度，而材料的其余位置能量密度较低，不会被飞秒激光所破坏，进而实现高空间分辨率的微纳加工；
4) 三维加工。飞秒激光可聚焦在衬底材料内任意深度，根据所需的尺寸和形状进行扫描，便于制备不同三维形态和分布的光学器件。

本论文工作主要采用飞秒激光加工技术，下面对该技术进行简要介绍。

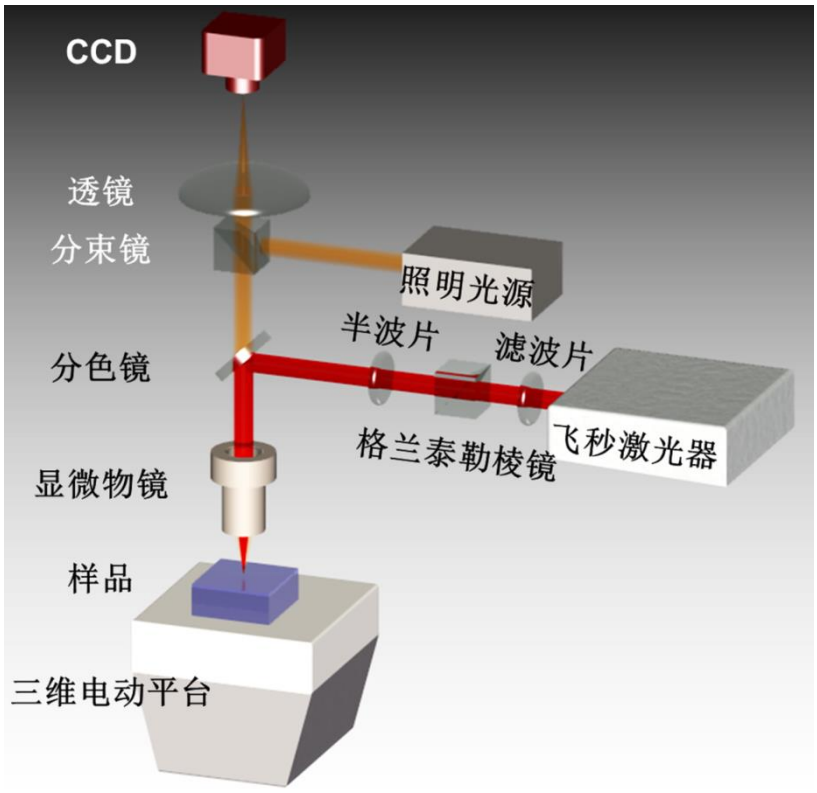

图 2.2.1 飞秒激光加工设备示意图

飞秒激光加工制备光波导主要是将超短脉冲激光聚焦在透明光学材料中进行激光诱导从而改变材料的折射率，形成光波导结构。在加工过程中，聚焦后的飞秒激光脉冲能量密度足够高，可以引起多光子吸收、隧穿电离和雪崩电离，诱导产生电子等离子体。随后，等离子体通过电子—声子耦合将能量传递给材料，引发材料的结构变化，例如应力变化、折射率改变。飞秒激光经过一次或多次扫描，可制备不同结构的光波导。

飞秒激光加工设备主要由飞秒激光器、光学元件和三维电动平移台组成，本论文工作均采用西班牙萨拉曼卡大学（Universidad de Salamanca, Spain）的钛宝石飞秒激光系统，下面以此套设备为例对飞秒激光加工的设置进行简要介绍。如图 2.2.1 所示，采用钛宝石飞秒激光系统（Spitfire, Spectra Physics, USA），飞秒激光的工作中心波长为 800 nm，脉宽为 120 fs，重复频率为 1 kHz，最高脉冲能量为 1 mJ。飞秒激光经过半波片、格兰泰勒棱镜、分束镜等光学元件后由显微物镜聚焦在样品表面或内部，通过调节光学元件可以实现对飞秒激光的偏振、脉冲能量等参数的调控。样品放置在可旋转、俯仰的三维 *XYZ* 电动平台上，电动平台水平方向(*XY*)分辨率为 100 nm，竖直方向（*Z*）分辨率为 1 μm，通过电脑程序编写代码可控制样品在三维空间移动，调节写入速度、方向及聚焦深度。在操作过程中利用 CCD 和照明光源对样品进行实时观测。

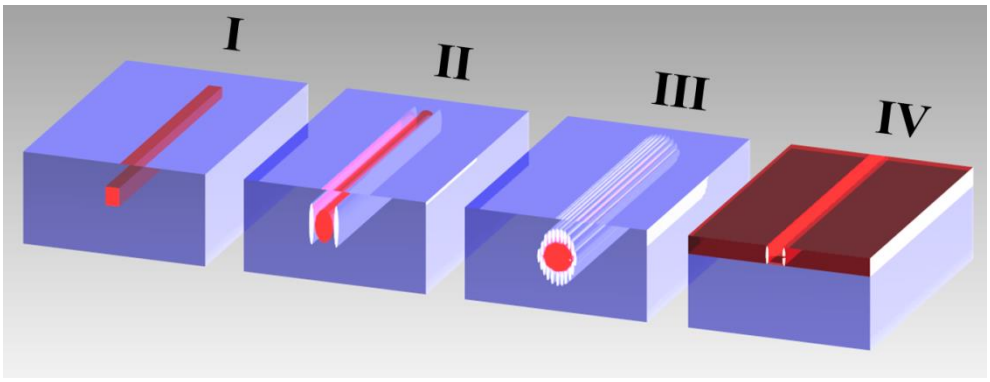

图 2.2.2 飞秒激光加工光波导结构示意图

根据光波导形成机理的不同，我们将飞秒激光所制备的光波导分为四类：

I. 飞秒激光写入折射率升高型光波导。飞秒激光写入痕迹处折射率升高，附近折射率保持不变，因而飞秒激光写入痕迹处即为光波导，如图 2.2.2

所示。基于此特点，可以在材料中直接写入形成二维或三维光波导、分支器等器件。这种类型的光波导易在玻璃[33-35]，如熔融石英等材料中制备，晶体中仅在以下几种中有报道：$LiNbO_3$ [36,37]、ZnSe[38]、Nd:YCOB [39]及本文所研究的 BGO 晶体[40]。

II. 飞秒激光写入双线型光波导：飞秒激光辐照区域折射率明显降低，写入位置周围由于应力作用折射率升高，利用两条或多条折射率降低的写入痕迹形成两条平行的折射率降低的直线，中间所夹的折射率升高区域即二维双线型通道光波导，如图 2.2.2 所示。双线长度一般约为 15~30 μm，间隔为 10~20 μm。此类波导已在诸多材料中实现，如 Yb:YAG 陶瓷[41]、硅酸盐玻璃[42]、Nd:YAG 晶体[43]、BiB_3O_6 晶体[44]、Nd:YVO_4 晶体[45]、Nd:GGG 晶体[46]、$LiNbO_3$ 晶体[47]、KTP 晶体[48]等，并实现了波导激光和波导倍频激光输出。

III. 飞秒激光写入包层光波导。与双线型光波导类似，包层光波导飞秒激光写入痕迹处折射率降低，不同的是，包层光波导一般写入速度较快，如 500 μm/s，因此写入痕迹较短，折射率变化较小，周围区域不受影响。包层光波导的结构由多条写入痕迹组成，各写入痕迹相互平行但位于样品不同的深度，形成一个折射率降低的准连续闭合区间，其内部包围区域为二维通道光波导。一般而言，包层光波导的每一个写入痕迹宽度在百纳米尺度，长度仅为几个微米，其所形成的闭合曲线形状可任意设计，常见的圆形包层光波导与光纤类似，可实现波导—光纤的对接。包层光波导的优势是支持任意偏振方向的激光传输[49-51]，这有利于实现非线性光波导中的二次谐波产生等。目前，包层光波导已广泛应用于各种透明材料的波导加工中，更有具优异性质的双包层结构光波导[52,53]制备成功。

IV. 飞秒激光烧蚀通道光波导。采用高能量的飞秒激光脉冲进行加工时，材料表面会被激光辐照烧蚀掉。在平面波导上运用飞秒激光烧蚀的方法制备具有一定距离（即波导宽度）的两条烧蚀痕迹，中间区域形成通道光波导。该类型波导的性能主要取决于平面光波导的性质，且飞秒激光烧蚀会造成波导额外的损耗[20]，本论文不对此类波导进行研究。

本论文中所研究的波导类型主要为折射率升高型、双线型、包层通道光波导及折射率升高型波导分支器。

2.3 光波导技术

本节对光波导的导波特性表征方法进行简要介绍，主要包括端面耦合技术、波导折射率重构、光波导传输模拟及光波导损耗的测量与计算。

2.3.1 端面耦合技术

端面耦合技术是最常用的波导光激励方法。利用显微镜物镜或者透镜将入射激光汇聚后，垂直入射至波导端面，经波导传输后由另一端面出射，出射光同样经显微镜物镜或透镜收集后利用功率计、CCD、光谱仪等进行收集与分析。图 2.3.1 为波导端面耦合的示意图。基于端面耦合技术，可以测量波导在不同波段下的导波特性，如近场光强分布、损耗及折射率变化等。另外，在端面耦合系统光路中可插入不同的光学器件，实现更复杂的功能，如偏振片/半波片可以用来起偏或改变入射光的偏振；具有相应的透射率和反射率的腔镜可以形成谐振腔，激励波导激光、二次谐波的产生等；加入可饱和吸收体可实现调 Q/锁模脉冲激光的输出。本文主要采用端面耦合技术进行波导的激励。

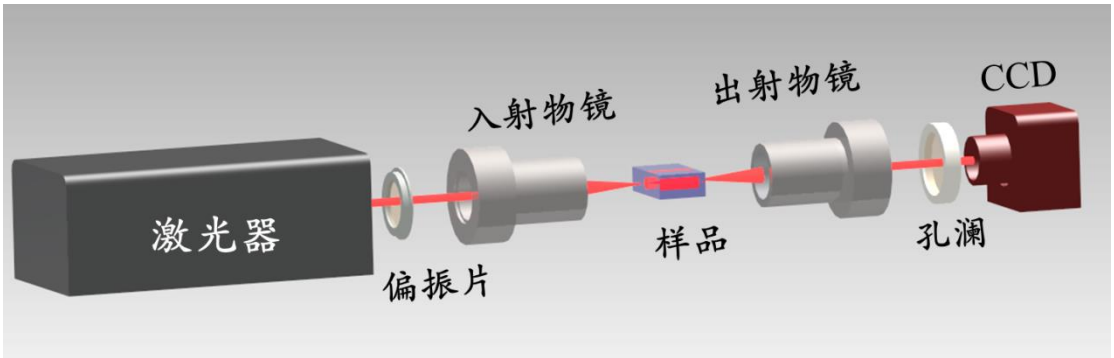

图 2.3.1 光波导端面耦合转置示意图

2.3.2 折射率重构

本文的主要研究对象为通道光波导，该类型光波导一般由折射率较低的包层包围一个折射率较高的条形区域组成，根据经验，该类型的波导折射率分布模型可采用阶跃型折射率分布进行模拟。通过测量波导的数值孔径角 θ_m[54,55]（即光

能够在光波导中有效传输的最大入射角度），可得到波导区域和周围区域的折射率对比 Δn：

$$\Delta n=\frac{\sin^2\theta_m}{2n_0} \tag{2.3.1}$$

其中，n_0 为衬底材料的折射率。该方法测量简单，可有效的估算波导区域的折射率变化，由最大入射角的测量引入的误差约在 30%。

2.3.3 光波导传输模拟

光束传播法[56]（Beam Propagation Method，简称 BPM）是目前模拟和设计光在波导器件中传输的主要方法，其基本步骤有：首先设置波导的折射率分布和初始入射光场分布，沿光的传输方向分为若干个传播截面，然后根据前一个或几个截面上已知的场分布逐步计算下一个传播截面上的场。根据计算方法的不同，光束传播法主要有以下几种：

1. 快速傅里叶变换光束传播法[57]（Fast Fourier Transform Beam Propagating Method，简称 FFT-BPM）。作为最初的 BPM 算法，FFT-BPM 方法受到了广泛的关注和应用，但由于快速傅里叶变换方程是标量方程，该方法还有很大的局限性，例如：能进行一个偏振方向上的计算，不能分辨 TE 模和 TM 模；样品点数量必须为 2 的幂；侧向的离散宽度较大且必须是均匀的；不能使用简单的透明边界条件；计算速度较慢等。
2. 有限差分光束传播法（Finite Difference Beam Propagating Method，简称 FD-BPM），又分为频域有限差分法（Finite Difference Frequency Domain，简称 FDFD）和时域有限差分法（Finite Difference Time Domain，简称 FDTD）。其中 FDFD-BPM 基于差分原理，把偏微分方程的定解问题通过划分网格的方法转化为一组相应的差分方程，得到离散解后应用差值方法即可得到整个场上的近似解。该方法适用于简单波导结构的模式求解。后者 FDTD-BPM 是目前流行的模拟方法，同样的差分原理，对时间空间进行离散化从而实现光波传输的模拟。该方法广泛用于计算光波导的传输模式、有效折射率及研究复杂波导器件之间的耦合、连接等问题。

3. 有限元光束传播法（Finite Element Beam Propagating Method，简称FE-BPM）。以变分原理为基础，通过解泛函求极值，得到横截面上的场分布。该方法通用性强、精度高，但计算量较大，常用于光波导模式的模拟。

本文模拟工作主要采用 Rsoft®软件[58]中 BeamPROP 程序，这是一个集合计算机辅助设计（CAD）与模拟（Simulation）的专业软件，该软件基于 FDTD-BPM 算法，其参数设置和软件界面如图 2.3.2 所示。根据模拟结果和实验结果的对照，可以得到波导的折射率分布、传输模式等。

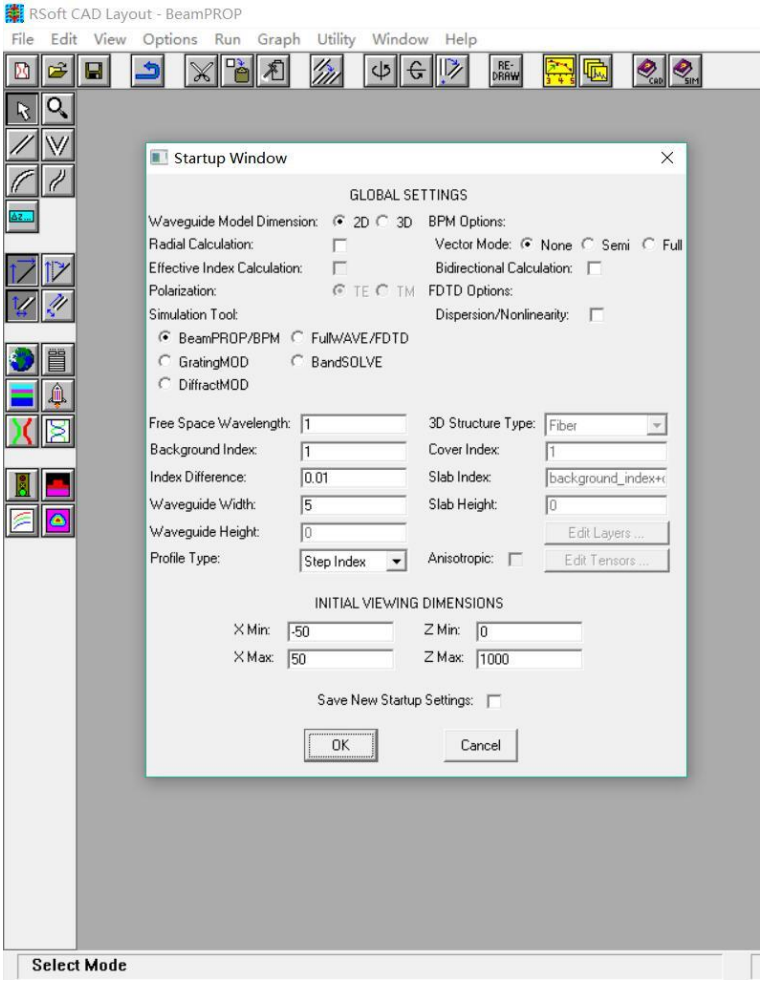

图 2.3.2 Rsoft-BeamPROP 的参数设置和软件界面

2.3.4 光波导损耗的测量与计算

光波导损耗（α）是指光在波导中的传播时能量的衰减，是评价介质光波导性能的一个重要参数。光从波导一端传输至另一端，功率由 P_{in} 降至 P_{out}，则有插入损耗 α（dB）：

$$\alpha = 10 \lg \frac{P_{in}}{P_{out}} \tag{2.3.2}$$

插入损耗由耦合损耗 α_c（dB）和传输损耗 α_p（dB/cm）组成。耦合损耗 α_c 主要与光在波导和空气界面发生的菲涅尔反射，以及入射光模式和导波模式之间的转换效率有关。其中菲涅尔反射系数 R 可由公式[59]计算:

$$R = \left(\frac{n_{eff} - 1}{n_{eff} + 1} \right)^2 \tag{2.3.3}$$

其中，n_{eff} 为有效折射率，1 即空气中的折射率。当波导模式为单模时，入射光模式和导波模式之间的的转换效率 β 可使用下面的公式进行近似：

$$\beta = \left(\frac{2\omega_1\omega_2}{\omega_1^2 + \omega_2^2} \right)^2 \tag{2.3.4}$$

其中，ω_1、ω_2 分别为入射光模式和波导模式的直径。

传输损耗 α_p 产生的因素主要有：由折射率分布不均匀或波导界面粗糙而引起的散射损耗；材料杂质或缺陷引起的吸收损耗；波导弯曲引起的辐射损耗等。波导的传输损耗测量方法主要有以下几种：背反射法（Back-Reflection Method），主要适用于平面波导；截断法（Cut-back Method），适用于长度较长的波导；滑动棱镜法（Prism Sliding Method），适用于长度较长的波导，且波导的散射光不能太弱；法布里珀罗谐振腔法（Fabry-Perot Method），适用于通道光波导，但需要对样品进行加热。本文主要基于端面耦合系统，测量插入损耗 α，计算耦合损耗 α_c，以其差值得到波导的传输损耗，公式如下:

$$\alpha_p = \frac{10}{L} \lg \left(D \cdot \beta \cdot (1 - R)^2 \cdot \frac{P_{in}}{P_{out}} \right) \tag{2.3.4}$$

其中，L 为波导的长度，D 为各光学元件的透过率。

2.4 波导激光理论

自 1917 年爱因斯坦（Alert Einstein）在量子理论的基础上提出，在物质与辐射场的相互作用中，构成物质的原子或分子可以在光子的激励下产生受激发射或者吸收，激光的理论逐步完善[60]。受科学技术和生产条件的限制，直至 1960 年世界第一台红宝石固态激光器才问世[61]，随后科学家研发了不同类型的激光器，对各科学领域和应用技术起到了巨大的推进作用。由于光波导结构的特性及广泛的应用，波导激光也随之问世[62]，与体材料激光相比，波导激光具有紧凑的谐振腔和更高的腔内能量密度，在激光性能上更胜一筹，易于集成在光学器件中。目前，科学家已在多种激光增益介质中实现波导激光，并广泛利用于通信、军事、传感、医疗和工业等领域。下面对波导激光的激励及连续和调 Q 脉冲激光分别进行介绍。

2.4.1 波导激光的激励

本文采用稀土离子掺杂的晶体材料作为增益介质，易获得高的增益和输出功率，且晶体的损伤阈值较高。基于端面耦合系统，我们采用“Fabry-Perot”谐振腔进行波导激光泵浦，如图 2.4.1 所示。波导的两个端面经光学抛光，使用两个反射镜与端面紧密接触，形成激光谐振腔。这种方法结构简单，易在光路中插入光学元件对激光泵浦进行调谐及分析，是常用的波导激光泵浦方法。

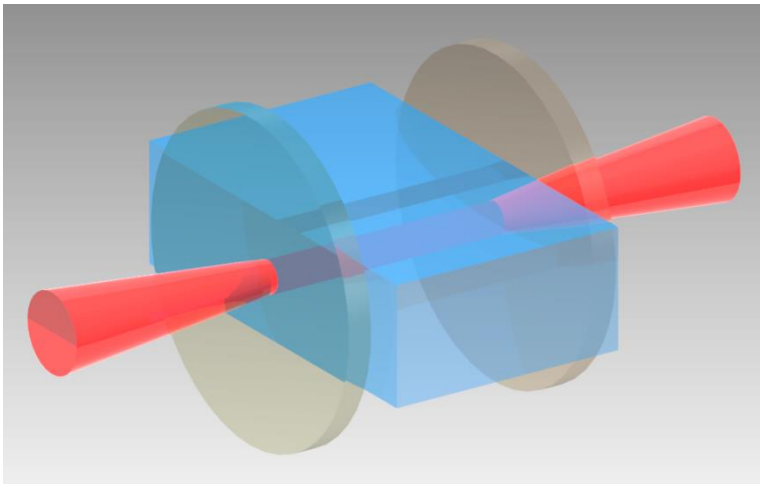

图 2.4.1“Fabry-Perot”谐振腔

2.4.2 连续波导激光

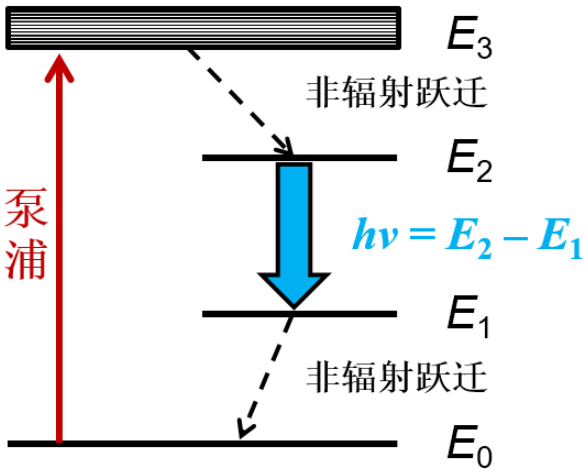

图 2.4.2 四能级激光器的能级简图

得利于波导的微型结构，激光谐振腔内的光密度大大增加，有利于获得低阈值、高功率的波导激光。相比于三能级激光系统，四能级系统激光系统易形成粒子数反转，激光阈值更低，其能级简图如图 2.4.2 所示[63]。在泵浦光辐射下，原子由基态 E_0 跃迁至能级为 E_3 的激发态，接着快速地无辐射跃迁进入 E_2 能级，后发射一个能量为 hv 的光子到达 E_1 能级，再经无辐射跃迁回到基态 E_0。下面对四能级激光系统的通道光波导激光的性质进行分析[64]。

波导的激光阈值为：

$$P_{\mathrm{th}}(ch)=\frac{\sqrt{3}\pi n\left[\left(\omega_{P,x}^2+\omega_{L,x}^2\right)^{1/2}\left(\omega_{P,y}^2+\omega_{L,y}^2\right)^{1/2}\right]}{l\left(\lambda_P+\lambda_L\right)}\left(\frac{\alpha_t+D}{\alpha_b+D}\right)P_{\mathrm{th}}(b) \tag{2.4.1}$$

上述公式中 $P_{\mathrm{th}}(ch)$和 $P_{\mathrm{th}}(b)$分别为通道波导激光和体材料激光的阈值；n 为体材料的折射率；l 为体材料的长度；$\omega_{L/P,x/y}$ 分别为泵浦激光（P）/波导激光（L）的光斑在水平（x）/竖直方向（y）的束腰半径；λ_P 和 λ_L 分别为泵浦光和波导激光的波长；α_t 和 α_b 分别代表通道光波导和衬底材料中激光的往返损耗；D 为出射腔镜在波导激光波长的反射率的自然对数。

由 2.4.1 式可得，波导激光阈值低于体材料激光阈值，通过增加波导的长度 l，减小泵浦光和波导激光光斑的束腰半径（ω），降低波导损耗，可以降低激光

泵浦阈值。因此，波导的设计和制备条件的优化，有利于提升波导激光器件的应用性能。

激光斜效率 η 是指泵浦激光与激光之间功率的转换效率，是表征激光性能的另一重要指标。波导激光的斜效率可表示为：

$$\eta=\left(\frac{D}{D+a}\right)\left(\frac{\nu_L}{\nu_P}\right)\left[1-\exp(\alpha_{\mathrm{p}}l)\right]\left(\frac{dS}{dF}\right) \tag{2.4.2}$$

其中，$\frac{\nu_{\mathrm{L}}}{\nu_P}$ 为与光子转换过程中的量子数亏损，等于 $\frac{\lambda_{\mathrm{p}}}{\lambda_L}$；$\alpha_{\mathrm{p}}$ 为激光增益介质对泵浦光的吸收系数；$\frac{dS}{dF}$ 为泵浦激光与波导激光模式的重叠因数。通道光波导在二维空间上对光进行限制，所以其泵浦激光与波导激光模式的重叠因数较高，有利于提高激光的斜效率。

2.4.3 激光调 Q 技术

激光器有两种工作方式：连续和脉冲。脉冲激光是将激光的能量压缩在宽度极窄的脉冲中，达到极高的峰值功率。常用的脉冲激光的产生方式有调 Q 和锁模技术，本文主要介绍调 Q 脉冲激光的产生。1960 年第一台激光器问世后，1962 年就成功研制了第一台调 Q 激光器，发展至今，已可获得脉冲峰值功率为兆瓦、脉宽为纳秒量级的调 Q 脉冲激光输出。调 Q 脉冲激光目前已应用在光谱分析、激光测距、激光雷达、核聚变等领域[65,66]。

Q 值，即调 Q 脉冲激光的品质因数，是评定激光器谐振腔质量好坏的标志，其定义如下：

$$Q=2\pi\nu_0\frac{\text{腔内储存的激光能量}}{\text{每秒消耗的激光能量}}=\frac{2\pi nL}{\delta\lambda_0} \tag{2.4.3}$$

其中，n 为激光增益介质的折射率，L 为激光谐振腔的长度，δ 为光在谐振腔内传输一个单程时的能量损耗率，ν_0 和λ_0分别为真空中的激光频率和波长。Q 值与谐振腔内损耗成反比关系，一般通过改变腔内损耗的方法来调节谐振腔的 Q 值。调 Q 过程即使得 Q 值循环变化：在泵浦激励的初始阶段，谐振腔内 Q 值较低，腔内损耗高，由于阈值高而不能产生激光振荡，亚稳态的粒子数不断累积；

Q 值突然提高，阈值下降，上能级储存的大量粒子能量迅速转化为激光能量，形成一个脉冲输出。

可以使得谐振腔损耗发生变化实现调 Q 的元件称作 Q 开关。调 Q 方法又分主动调 Q（如转镜、电光和声光调 Q)和被动调 Q（可饱和吸收调 Q）。两者相比，主动调 Q 的激光振荡阈值可调控，而被动调 Q 结构简单、价格便宜、不需要外加驱动装置，是一种便捷的实现调 Q 脉冲激光的方式。下面主要对被动调 Q 中的可饱和吸收调 Q 进行介绍。

可饱和吸收调 Q，是指利用可饱和吸收体控制谐振腔的损耗以达到调 Q 的目的。泵浦初始阶段，可饱和吸收体吸收系数较大，谐振腔内损耗大；在较强激光下，吸收系数显著减小直至饱和，入射光几乎全部透明的透过，激光振荡产生。可饱和吸收体具有以下特点：稳定性强，吸收峰波长与激光器激光波长吻合；饱和光强大小合适。常用的可饱和吸收体有半导体可饱和吸收镜，过渡金属掺杂的晶体，有机染料，石墨烯等。近年来，随着材料科技的发展，越来越多的新型可饱和吸收材料由于其优异性质收到广泛的关注，比如石墨烯、碳纳米管、拓扑绝缘体材料等[67-69]。本文采用石墨烯作为可饱和吸收体实现波导调 Q 脉冲激光的输出。

2004 年英国曼彻斯特大学科学家 K. S. Novoselov 和 A. K. Geim 首次发现石墨烯[70]。石墨烯具有零带隙结构，导带和价带相交于狄拉克点，因此对光的吸收波长无选择性；导热系数为 5300 W/m·K，具有较高的热损伤阈值；调制深度大；制备简单，成本相对低廉，是优秀的可饱和吸收体材料[71-73]。图 2.4.3 是单层石墨烯的的结构示意图。

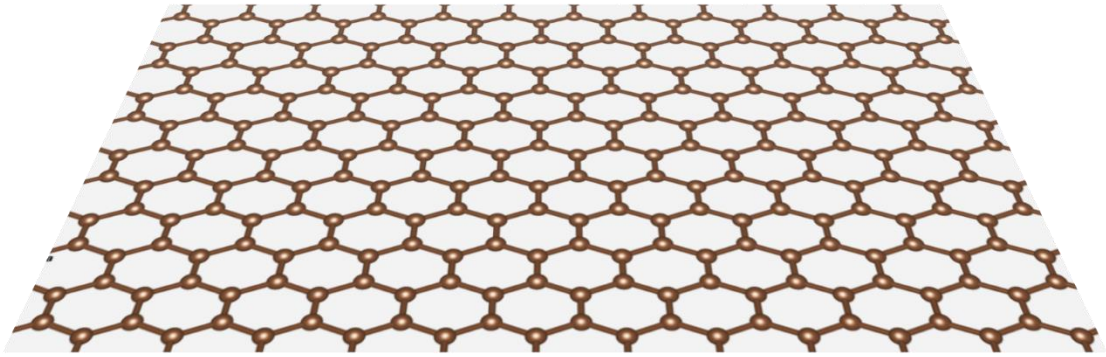

图 2.4.3 单层石墨烯结构示意图

2.5 共聚焦荧光显微技术

2.5.1 荧光分析[74]

1852 年，Stoles 首次提出“荧光（fluorescence）”一词，用来描述叶绿素荧光及其重吸收现象。荧光是一种光致发光现象[75]，伴随着分子能量的吸收和释放，图 2.5.1 所示的 Jablonski 图说明了光能量吸收和释放的跃迁过程。

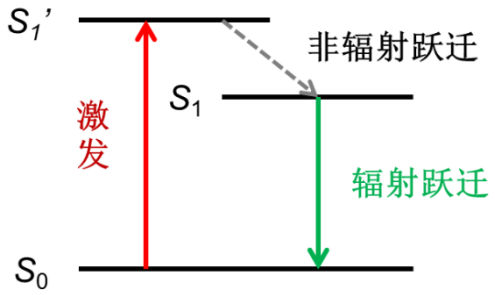

图 2.5.1 Jablonski 能级简图

首先，分子吸收一个光子，由基态S_0跃迁至激发态S_1'，两能级之间的能量差值为所吸收的光子能量 $h\upsilon_{ex}$，即$S_0 + h\upsilon_{ex} \longrightarrow S_1'$。处于激发态的分子并不稳定，会释放能量回到基态，这个过程包括辐射跃迁（如荧光、磷光）和非辐射跃迁（如振动弛豫、系间跨越）。从S_1'经非辐射跃迁很快的到达能量较低的激发态S_1后迅速释放能量回到基态S_0，并释放一个能量为 $h\upsilon_{em}$ 的光子，即$S_1 \longrightarrow S_0 + h\upsilon_{em}$。

根据荧光的激发光和发射光的波长大小可以分为三类：

1. 激发波长 < 发射波长时，发生斯托克斯（Stokes）位移，称为斯托克斯荧光，是一般常见的荧光现象；
2. 激发波长 > 发射波长时，发生反斯托克斯位移，称为反斯托克斯荧光。如双光子/多光子荧光，通常需要强的激发光源产生；
3. 激发波长 = 发射波长时，称为共振荧光。

荧光分析的两个特征光谱为激发光谱和发射光谱。激发光谱是指在不改变测定荧光波长的情况下，改变激发光波长，测得荧光强度随激发波长的变化，发射光谱是指在固定荧光激发光波长的情况下，测量荧光强度随荧光发射波长的变化。荧光光谱可作为荧光物质的编码，对物质进行标记，实现物质检测。

荧光发射光谱有两个重要特征：一是与激发波长无关，荧光光谱的形状一般是固定的；二是与吸收光谱呈对称镜像关系，而吸收光谱与激发光谱形状近似。

由于存在非辐射跃迁，荧光过程并不是每吸收一个光子就相应地释放一个光子。荧光量子产率 Q_e，又称量子效率，定义为发射光子数与激发光子数之比。Q_e 与温度相关：

$$Q_e = \frac{\text{释放光子数}}{\text{激发光子数}} \tag{2.5.1}$$

荧光寿命 τ 是指当物质吸收能量由基态跃迁到激发态，再以辐射跃迁的形式发出荧光回到基态时，荧光的强度由最大值 I_0 降低至 1/e 处时所需要的时间，可用下式表示

$$I_t = I_0 e^{-kt} \tag{2.5.2}$$

其中，I_t 是时间 t 时的荧光强度，k 为衰减常数，当在时间 τ 时荧光强度 I_τ 衰减至 I_0 的的 1/e，则 τ 即荧光寿命。

2.5.2 共聚焦荧光显微镜

共聚焦显微镜（Confocal Microscopy）的概念由 M. Minsky 于 1957 年提出，1979 年 G. F. Brakenhoff 由高数值孔径透镜装置上改装成功共聚焦显微镜，1987 年第一台激光扫描共聚焦显微镜出现。20 世纪 90 年代后，光学、电子学及计算机科技的进步不断推动着共聚焦显微镜技术的完善，广泛应用于医学、生物学、植物学、半导体及材料科学等领域。

共聚焦荧光显微镜[76,77]（Confocal Fluorescence Microscopy）即共聚焦技术的一个典型应用，根据技术结构的不同又分为数字共聚焦显微镜（Digital Confocal Microscopy, DCM）和激光扫描共聚焦显微镜（Laser Scanning Confocal Micrpscopy, LSCM）。数字共聚焦显微镜是在传统荧光显微镜的基础上使用计算机算法，将样品焦平面和焦平面外的光信息分离，进行图像分析，该方法使用的照明激发光谱宽（氙灯或汞灯）、操作方便、成本低、灵活性强，具有广泛的应用前景。激光扫描共聚焦显微技术更为成熟，使用单色性好的激光作为激发光源，通过共轭的聚焦系统对样品进行点扫描，经软件处理获得的荧光图片，该方法成

像清晰、对比度高。本文工作使用激光扫描共聚焦显微技术，选择合适的激发激光，测量稀土离子掺杂晶体的荧光发射光谱。

与传统显微镜相比，激光扫描共聚焦显微镜具有以下优势：

i. 侧向分辨率高；

ii. 轴向分辨率高，可获得光学断层扫描，适用于较厚的样品；

iii. 逐点扫描，去除杂散光的影响；

iv. 对比度高，便于测量信号较弱的样品。

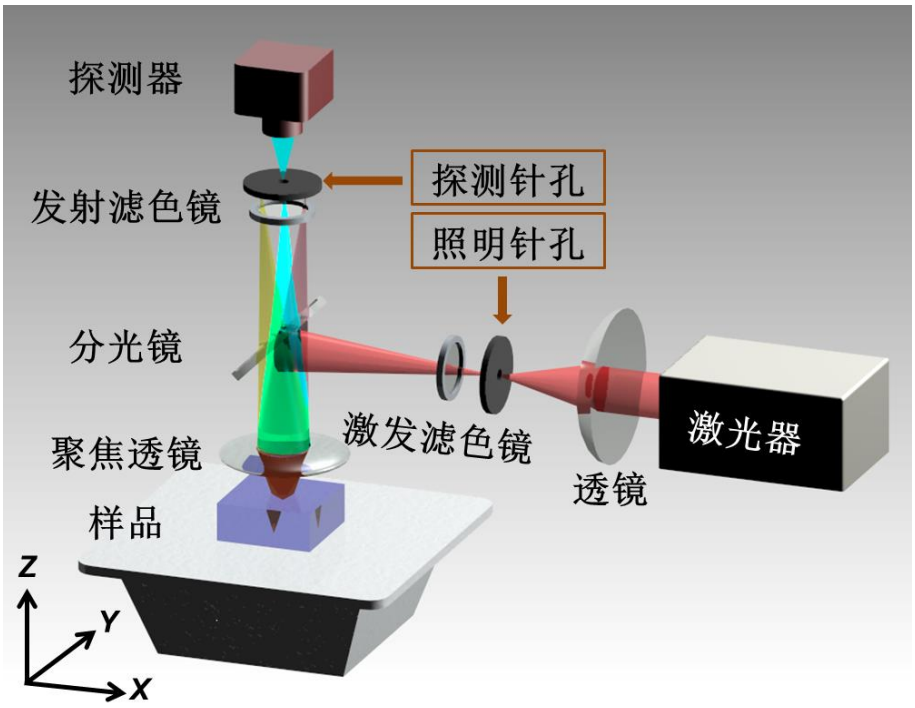

图 2.5.2 激光扫描共聚焦荧光显微镜的原理图

激光扫描共聚焦显微镜的原理如图 2.5.2 所示。相干的激光光源通过照明针孔被显微物镜聚焦照射在样品焦平面上一点，该焦点发射的荧光被同一个显微物镜收集，沿原光路返回由分光器，经探测针孔到达探测器，该焦点以外的任何发射光都被探测针孔阻挡。探测针孔与照明针孔对于焦点是共轭的，被探测点即共焦点，其所在平面即共焦平面。激光对样品焦平面（*xy* 平面）进行逐点扫描，也可以沿深度（*z* 轴）不断移动，最终经计算机显示为一幅三维荧光图像，

本文采用西班牙马德里自治大学的共聚焦荧光显微镜进行测试，实验装置主要由四个部分构成：

1. 激光光源，对不同的荧光物质，采用特定波长的激光器作为光源。激光的功率、模式等参数可以根据样品的激发要求进行设置；
2. 聚焦系统，根据样品的尺度和荧光光谱特征，选择适合的显微物镜作为聚焦物镜。例如在 Nd^{3+}离子荧光测量实验中，采用放大倍数 100×，数值孔径为 0.85 的长工作距离消色差显微物镜作为聚焦物镜，在荧光激发和发射光谱所处的近红外波段透过率大于 80%。
3. 扫描模块，采用 *XYZ* 三维电动系统，在 *XYZ* 方向的分辨率均为 0.1 μm，由程序控制电动平台移动，可获得三维荧光图谱。
4. 探测与分析，采用光谱仪（Horiba Jobin Yvon iHR320）收集发射荧光，分析荧光光谱的特性，包括谱线形状、峰值位置、荧光强度和谱线展宽。

2.6 荧光测温技术

荧光测温技术[78-80]是一种通过分析荧光谱线对材料进行温度表征的技术，具有无接触、分辨率高、灵敏度高等优点。荧光测温技术已被应用于纳米颗粒，荧光分子等进行温度表征[81-84]，具有广泛的应用前景。

2.6.1 荧光的温度敏感性

发射荧光的性质取决于电子能级跃迁过程[80]，玻尔兹曼分布决定了荧光发射与温度有关[85]。荧光强度（Intensity）、带宽（Bandwidth）、峰值位置（Peak Position）、光谱形状（Band-Shape）、偏振（Polarizaiton）及荧光寿命（Lifetime）都与温度有一定的关系，图 2.6.2 给出温度不同时，荧光参数的变化[78]。

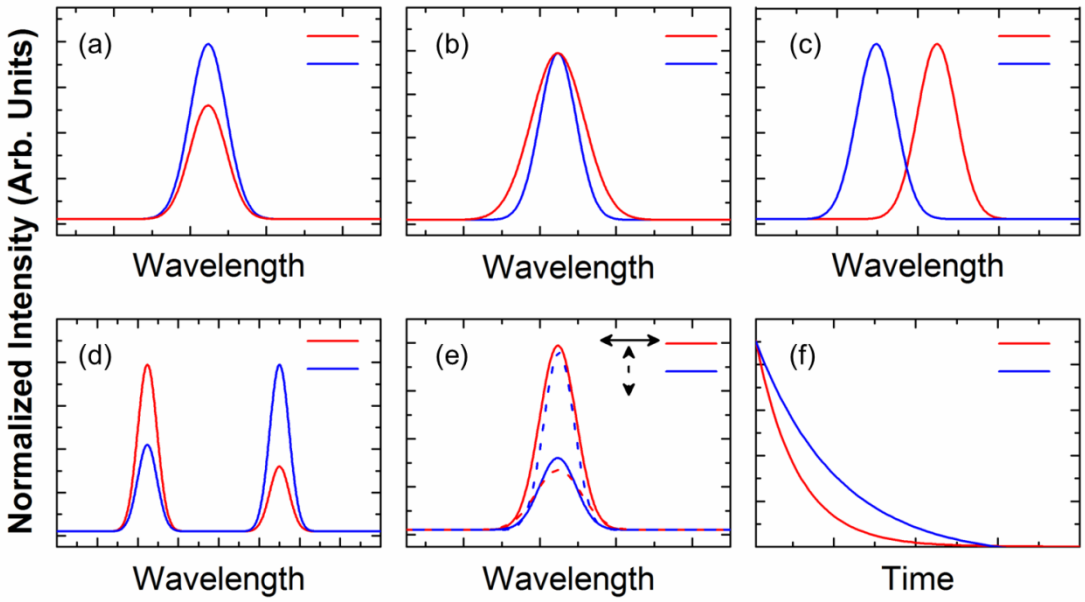

图 2.6.2 不同温度下，荧光参数的变化（a）荧光强度、（b）带宽、（c）峰值位置、（d）光谱形状、（e）偏振、（f）荧光寿命。红色和蓝色分别代表温度的高和低

其中红色和蓝色分别代表温度的高和低，另外（e）中实虚线分别代表相互垂直的两个偏振方向。可以得出以下结论：

a) 当温度升高时，由于产生荧光淬灭及非辐射跃迁衰减概率的增大，导致单位时间内激发的荧光光子的数量减少，所以荧光的强度降低；

b) 荧光谱线的带宽由材料的性质和温度决定。一般地，随着材料温度升高，声子密度相应增大，导致均匀的荧光谱线的展宽。室温下，这种谱线展宽和温度呈线性关系；

c) 荧光谱线的峰值位置由发射相对应的两个电子能级决定，这受材料的折射率、原子间距/密度等诸多温度相关因素的影响。因此，荧光峰值位置与温度有着密切的关系；

d) 发射光谱的形状体现为各个荧光谱线之间的相对强度。一般地，荧光谱线所对应的电子能级能量较接近为热耦合能级时，温度变化会引起发射光谱形态的变化，即两个荧光发射峰的强度比率发生变化；

e) 各向异性物质的荧光呈现各向异性的极化，因此发射光谱的形状和强度与其偏振紧密相关。荧光的偏振各向异性在此定义为两个相互垂直偏振态的荧光强度的比值 P。温度改变会引起的偏振各向异性的变化，因此可以用比值 P 的变化分析温度变化。

f) 荧光寿命的倒数即荧光衰减常数，描述荧光强度衰减的快慢。衰减常数的大小受一系列与温度相关因素的影响，如声子辅助能量转移过程、多声子衰变等。因此，荧光寿命受温度变化影响而变化。

上述荧光参数都可以用来表征温度的变化，其中光谱形状可以通过荧光强度比率法来测量，操作简单，应用广泛[79,86]。

2.6.2 荧光强度比率法

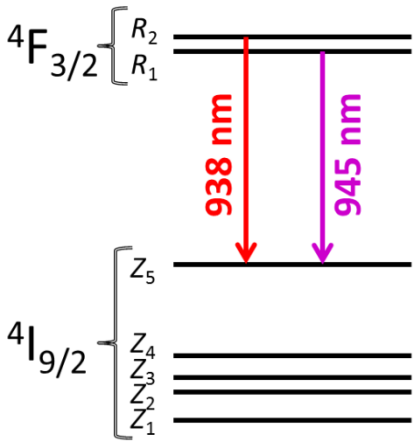

图 2.6.3 Nd:YAG 晶体中钕离子 $^4F_{3/2}\rightarrow{}^4I_{9/2}$ 能级跃迁简图，标明了具有温度敏感性的两个发射线 938 nm 和 945 nm

荧光强度比率法利用两个不同的激发态到低能级的荧光辐射的强度比，如图 2.6.3 所示，为 Nd:YAG 中 Nd^{3+}离子的 $^4F_{3/2}\rightarrow{}^4I_{9/2}$ 能级跃迁，对应两个发射谱线 938 nm 和 945 nm 的斯塔克次能级分别为 R_2 和 R_1。这两个谱线具有高的温度敏感性，因为它们和 $^4F_{3/2}\rightarrow{}^4I_{9/2}$ 能级跃迁产生的其它发射谱线相分离，易于分析。另外，产生荧光辐射的 $^4F_{3/2}$ 亚稳态的两个斯塔克次能级之间的能带宽度（对于 Nd:YAG 晶体来说，约为 80 cm^{-1}）约为 k_BT_m 的三分之一（207 cm^{-1}，其中 k_B 为玻尔兹曼常数，T_m 为温度），因此这两个发射谱线具有显著的温度特性。图 2.6.4（a）展示了 Nd:YAG 晶体在 60℃和 10℃下的发射光谱，温度高时 938 nm 所占的比例明显提高[87]。

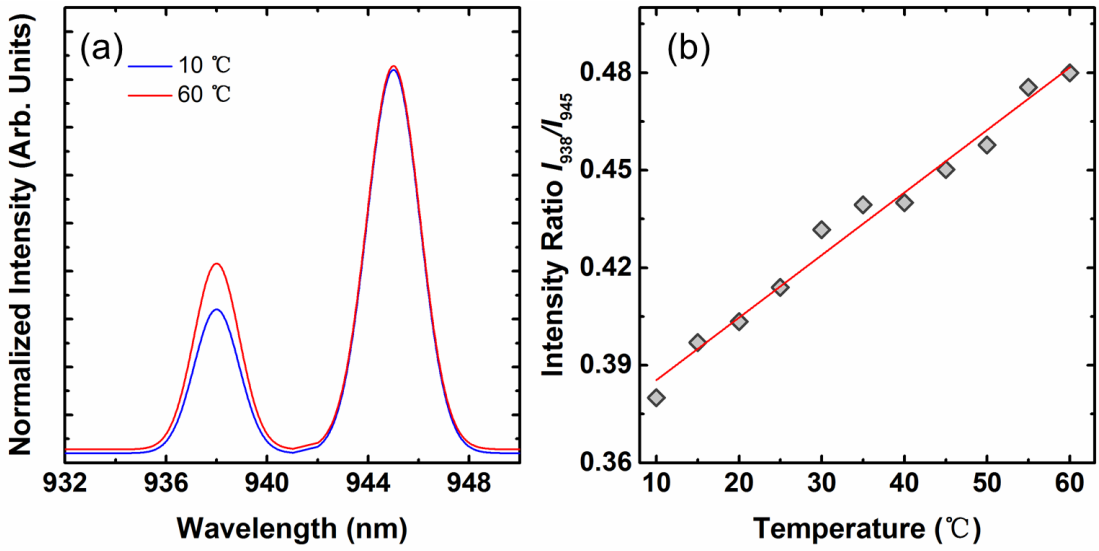

图 2.6.4（a）归一化的荧光发射图谱，红色和蓝色谱线对应样品温度分别为 60℃和 10℃，（b）发射线 938 nm 和 945 nm 强度比率随温度的变化，红色直线为线性拟合结果

荧光发射峰的强度（I）与其相应的发射能级的粒子数（N）成正比，关系如下，

$$\frac{I_2}{I_1}=\frac{N_{R2}}{N_{R1}}=A\cdot\exp\left(-\frac{\Delta E}{k_BT_m}\right) \tag{2.6.1}$$

其中 A 为一个常数，描述了能级 R_1 和 R_2 与温度无关的电子性质和光谱性质，ΔE 为能级 R_1 和 R_2 的能量差值。图 2.6.4（b）为荧光强度比率 R 随温度变化的示意

图，当温度变化较小时，近似呈线性增长趋势。

为描述荧光比率随温度变化的敏感性，定义热敏度 S[78]为：

$$S=\frac{1}{R}\frac{dR}{dT}，\quad R=\frac{I_1}{I_2} \tag{2.6.2}$$

参考文献

1. H. Nishihara, M. Haruna, and T. Suhara, Optical Integrated Circuits (Ohmasha, 1989).
2. K. Okamoto, Fundamentals of Optical Waveguides (Academic Press, 2000).
3. G. Lifante, Integrated Photonics: Fundamentals (John Wiley & Sons, 2003).
4. M. L. Calvo and V. Lakshminarayanan, Optical Waveguides: From Theory to Applied Technologies (CRC Press, 2007).
5. 曹庄琪. 导波光学, 科学出版社, 2007.
6. P. D. Townsend, P. J. Chandler, and L. Zhang, Optical Effects of Ion Implantation (Cambridge University Press, 1994).
7. F. Chen, Laser Photonics Rev. **6**, 622–640 (2012).
8. M. Goorsky, Ion Implantation (InTech, 2012).
9. H. Hu, A. P. Milenin, R. B. Wehrspohn, H. Hermann, and W. Sohler, J. Vac. Sci. Technol. A **24**, 1012–1015 (2006).
10. R. Ramponi, M. Malangoni, and R. Osellame, Appl. Phys. Lett. **78**, 2098–2100 (2001).
11. S. F. Wong, E. Y. B. Pun, and P. S. Chung, Photonics Tech. Lett. **14**, 80–82 (2001).
12. P. K. Tien, R. Ulrich, and R. J. Martin, Appl. Phys. Lett. **14**, 291–294 (1969).
13. F. Bruno, M. Guidice, R. Recca, and F. Testa, Appl. Opt. **30**, 4560–4564 (1991).
14. G. Poberaj, M. Koechlin, F. Sulser, A. Guarino, J. Hajfler, and P. Günter, Opt. Mater. **31**, 1054–1058 (2009).
15. T. Yamashiki and K. Tsuda, Opt. Lett. **28**, 316–318 (2003).
16. C. Mack, Fundamental Principles of Optical Lithography: The Science of Microfabrication (John Wiley & Sons, 2011).
17. Y. Y. Ren, Y. Tan, F. Chen, D. Jaque, H. J. Zhang, J. Wang, and Q. M. Lu, Opt. Express **18**, 16258–16263 (2010).
18. Y. Yao, Y. Jia, F. Chen, Sh. Akhmadaliev, and S. Zhou, Appl. Opt. **53**, 195–199 (2014).

19. R. DegI'Innocenti, S. Reidt, A. Guarino, D. Rezzonico, G. Poberaj, and P. Günter, J. Appl. Phys. **100**, 113121 (2006).
20. Y. Jia, N. Dong, F. Chen, J. R. Vázquez de Aldana, S. Akhmadaliev, and S. zhou, Opt. Express **20**, 9763–9768 (2012).
21. Z. Bi, L. Wang, X. Liu, S. Zhang, M. Dong, Q. Zhao, X. Wu, and K. Wang, Opt. Express **20**, 6712–6719 (2012).
22. T. Nishikawa, A. Ozawa, Y. Nishida, M. Asobe, F. L. Hong, and T. W. Hänsch, Opt. Express **17**, 17792–17800 (2009).
23. J. Sun, Y. Gan, and C. Q. Xu, Opt. Lett. **36**, 549–551 (2011).
24. Y. Jia, C. E. Rüter, Sh. Akhmadaliev, S. Zhou, F. Chen, and D. Kip, Opt. Mater. Express **3**, 433–438 (2013).
25. D. Choudhury, A. Rodenas, L. Paterson, F. Díaz, D. Jaque, and A. K. Kar, Appl. Phys. Lett., **103**, 041101 (2013).
26. Y. Cheng, K. Sugioka, and K. Midorikawa, Opt. Lett. **29**, 2007–2009 (2004).
27. F. Chen and J. R. Vázquez de Aldana, Laser Photonics Rev. **8**, 251–275 (2014).
28. D. Choudhury, J. R. Macdonald, and A. K. Kar, Laser Photonics Rev., **8**, 827–846 (2014).
29. A. A. Bettiol, S. Venugopal Rao, E. J. Teo, J. A. van Kan, and F. Watt, Appl. Phys. Lett. **88**, 171106 (2006).
30. A. Benayas, D. Jaque, Y. Yao, F. Chen, A. A. Bettiol, A. Rodenas, and A. K. Kar, Opt. Lett. **35**, 3898–3900 (2010).
31. Y. Yao, N. Dong, F. Chen, S. K. Vanga, and A. A. Bettiol, Opt. Lett. **36**, 4173–4175 (2011).
32. K. M. Davis, K. Miura, N. Sugimoto, and K. Hirao, Opt. Lett. **21**, 1729–1731 (1996).
33. A. Zoubir, C. Lopez, M. Richardson, and K. Richardson, Opt. Lett. **29**, 1840–1842 (2004).
34. I. Spaleniak, S. Gross, N. Jovanovic, R. J. Williams, J. S. Lawrence, M. J. Ireland, and M. J. Withford, Laser Photonics Rev. **8**, L1–L5 (2014).

35. L. Shah, A. Y. Arai, S. M. Eaton, and P. R. Herman, Opt. Express **13**, 1999–2006 (2005).
36. J. Burghoff, S. Nolte, and A. Tünnermann, Appl. Phys. A **89**, 127–132 (2007).
37. R. R. Thomson, S. Campbell, I. J. Blewett, A. K. Kar, nd D. T. Reid, Appl. Phys. Lett. **88**, 111109 (2006).
38. J. R. Macdonald, R. R. Thomson, S. J. Beecher, N. D. Psaila, H. T. Bookey, and A. K. Kar, Opt. Lett. **35**, 4036–4038 (2010).
39. A. Ródenas and A. Kar, Opt. Express **19**, 17820–17833 (2011).
40. R. He, I. H. Palmero, C. Romero, J. R. Vázquez de Aldana, and F. Chen, Opt. Express **22**, 31293–31298 (2014).
41. T. Calmano, A.-G. Paschke, J. Siebenmorgen, S. T. Fredrich-Thornton, H. Yagi, K. Petermann, and G. Huber, Appl. Phys. B **103**, 1–4 (2011).
42. S. L. Li, P. Han, M. Shi, Y. Yao, B. Hu, M. Wang, and X. Zhu, Opt. Express **19**, 23958–23964 (2011).
43. G. Torchia, A. Rodenas, A. Benayas, E. Cantelar, L. Roso, and D. Jaque, Appl. Phys. Lett. **92**, 111103 (2008).
44. S. J. Beecher, R. R. Thomson, D. T. Reid, N. D. Psaila, M. Ebrahim-Zadeh, A. K. Kar, Opt. Lett. **36**, 4548–4550 (2011).
45. Y. Tan, F. Chen, J.R. Vázquez de Aldana, G.A. Torchia, A. Benayas, D. Jaque, Appl. Phys. Lett. **97**, 031119 (2010).
46. C. Zhang, N. N. Dong, J. Yang, F. Chen, J. R. Vázquez de Aldana, Q. M. Lu, Opt. Express **19**, 12503–12508 (2011).
47. J. Burghoff, C. Grebing, S. Nolte, and A. Tünnermann, Appl. Phys. Lett. **89**, 081108 (2006).
48. N. Dong, Y. Tan, A. Benayas, J. R. Vázquez de Aldana, D. Jaque, C. Romero, F. Chen, and Q. Lu, Opt. Lett. **36**, 975–977 (2011).
49. Y. Jia, J. R. V´azquez de Aldana, Q. Lu, D. Jaque, and F. Chen, J. Lightwave Technol. **31**, 3873–3878 (2013).
50. H. Liu, Y. Tan, J. R. Vázquez de Aldana, and F. Chen, Opt. Lett. **39**, 4553–4556 (2014).

51. Y. Ren, F. Chen, and J. R. Vázquez de Aldana, Opt. Express **21**, 11562–11567 (2013).
52. H. Liu, F. Chen, J. R. Vázquez de Aldana, and D. Jaque, Opt. Lett. **38**, 3294–3297 (2013).
53. H. Liu, J. R. Vázquez de Aldana, M. Aguiló, F. Díaz, F. Chen, and A. R. Seguíc, Opt. Eng. **53**, 097105 (2014).
54. J. Siebenmorgen, K. Petermann, G. Huber, K. Rademaker, S. Nolte, and A. Tünnermann, Appl. Phys. B **97**, 251–255 (2009).
55. J. Siebenmorgen, T. Calmano, K. Petermann, and G. Huber, Opt. Express **18**, 16035–16041 (2010).
56. H. J. W. M. Hoekstra, Opt. Quant. Electron. **29**, 157–171 (1997).
57. M. D. Feit, J. A. Fleck, Appl. Opt. **17**, 3390–3998 (1987).
58. http://www.rsoftdesign.com
59. D. Marcuse, Bell Syst. Tech. J. **56**, 703–718 (1977).
60. 周炳坤，高以智，陈倜嵘，陈家骅. 激光原理，国防工业出版社，2012.
61. T. H. Maiman, Nature **187**, 493–494 (1960).
62. E. Snitzer, Phys. Rev. Lett. **7**, 444–446 (1961).
63. W. Koechner. 固体激光工程（孙文，江泽文，程国祥译），科学出版社，2002.
64. C. Crivas, Prog. Quant. Electron. **35**, 159–239 (2011).
65. 姚建铨，徐德刚. 全固态激光及非线性光学频率变换技术，科学出版社，2007.
66. 李相银，姚玉敏，李卓，崔骥. 激光原理技术及应用，哈尔滨工业大学出版社，2003.
67. L. D. Boni, E. L. Wood, C. Toro, F. E. Hernandez, Plasmon. **3**, 171–176 (2008).
68. Y. Jia, C. Cheng, J. R. Vázquez de Aldana, G. R. Castillo, B. del Rosal Rabes, Y. Tan, D. Jaque, and F. Chen, Sci. Rep. **4**, 5988 (2014).
69. Y. Tan, H. Zhang, C. Zhao, S. Akhmadalie, S. Zhou, and F. Chen, Opt. Lett. **40**, 637–640 (2015).
70. K. S. Novoselov, A. K. Geim, S. V. Morozov, D. Jiang, Y. Zhang, S. V. Dubonos, I. V. Grigorieva, and A. A. Firsov, Science **306**, 666–669 (2004).

71. S. Yamashita, J. Lightwave Technol. **30**, 427 (2012).

72. Q. Bao, H. Zhang, Y. Wang, Z. Ni, Y. Yan, Z. X. Shen, K. P. Loh, and D. Y. Tang, Adv. Funct. Mater. **19**, 3077–3083 (2009).

73. D. Popa, Z. Sun, T. Hasan, F. Torrisi, F. Wang, and A. C. Ferrari, Appl. Phys. Lett. **98**, 073106 (2011).

74. 王立强，石岩，汪洁，郑华. 生物技术中的荧光分析，机械工业出版社，2010.

75. B. Valeur and M. N. Berberan-Santos, J. Chem Educ. **88**, 731–738 (2011).

76. J. B. Pawley, Handbook of Biological Confocal Microscopy (Springer, 2006).

77. A. P. Kusumbe, S. K. Ramasamy, A. Starsichova, and R. H. Adams, Nat. Protocol **10**, 1904–1914 (2015).

78. D. Jaque and F. Vetrone, Nanoscale **4**, 4301–4326 (2012).

79. C. D. S. Brites, P. P. Lima, N. J. O. Silva, A. Millán, V. S. Amaral, F. Palacio, and L. D. Carlos, Nanoscale **4**, 4799–4829 (2012).

80. G. F. Imbusch and B. Henderson, Optical Spectroscopy of Inorganic Solids, (Oxford Science Publications, 2006).

81. F. Vetrone, R. Naccache, A. Zamarrón, A. Juarranz de la Fuente, F. Sanz-Rodríguez, L. Martinez Maestro, E. Martín Rodriguez, D. Jaque, J. García Solé, and J. A. Capobianco, ACS Nano **4**, 3254–3258 (2010).

82. S. F. León-Luis, U. R. Rodríguez-Mendoza, I. R. Martín, E. Lalla, and V. Lavín, Sens. Actuators B Chem. **176**, 156–164 (2013).

83. A. Benayas, B. del Rosal, A. Pérez-Delgado, K. Santacruz-Gómez, D. Jaque, G. A. Hirata, and F. Vetrone, Adv. Opt. Mater. **3**, 687 (2015).

84. N. Ishiwada, T. Ueda and T. Yokomori, Luminescence, **26**, 381–389 (2011).

85. J. R. Lakowicz, Principles of Fluorescence Spectroscopy, (Springer, 2010).

86. J. Petit, B. Viana, and P. Goldner, Opt. Express **19**, 1138–1146 (2011).

87. R. He, J. R. Vázquez de Aldana, G. L. Pedrola, F. Chen, and D. Jaque, Opt. Lett. **41**, 2061–2064 (2016).

88. V. K. Rai, Appl. Phys. B **88**, 297–303 (2007).

第三章 飞秒激光写入锗酸铋晶体制备光波导及分支器

锗酸铋（BGO）是 Bi_2O_3-GeO_2 系化合物的总称，常特指其中一种化合物 $Bi_4Ge_3O_{12}$，是我国研制的一种性能优异的闪烁晶体，曾用于诺贝尔奖获得者丁肇中的实验中。BGO 晶体属于立方晶系，无色透明，密度大（7.13 g/cm^3），具有不易潮解，化学稳定性好，机械性质稳定等优势，在核医学、核电子学、空间物理及高能物理等领域有广泛的应用[1,2]。

迄今为止，科学家们已经利用离子注入、聚焦质子束写入、飞秒激光加工等方法在 BGO 晶体中制备平面以及通道光波导结构 [3-8]。

本章主要包括以下研究内容：

1.利用飞秒激光写入在 BGO 晶体中制备双线型光波导；

2.利用飞秒激光写入在 BGO 晶体中制备包层光波导；

3.利用飞秒激光写入在 BGO 晶体中制备折射率升高型光波导；

4.利用飞秒激光写入在 BGO 晶体中制备波导分支器。

3.1 BGO 晶体双线型通道光波导

本实验利用飞秒激光写入技术在 BGO 晶体中制备双线型通道光波导，并对其导波特性和热稳定性进行研究。结果表明高温退火可以大幅降低波导的传输损耗，提高波导的导波性能。

3.1.1 实验过程

本实验中所选用的 BGO 晶体六个表面经光学抛光加工处理，尺寸为 10 × 9.5 × 2 mm^3。具体实验过程如下：

i. 波导的制备

利用飞秒激光写入技术对 BGO 晶体进行扫描，制备由两条平行的写入痕迹组成的双线型通道光波导。飞秒激光写入实验采用西班牙萨拉曼卡大学（Universidad de Salamanca, Spain）的钛宝石飞秒激光系统（Spitfire, Spectra Physics, USA）。飞秒激光的工作中心波长为 800 nm，脉宽为 120 fs，重复频率为 1 kHz，最高单脉冲能量为 1 mJ，单脉冲能量可通过经中性滤波片、半波片以及线偏振片等光学元件进行连续调节。样品被放置在水平方向（*XY*）分辨率为 100 nm，垂直方向（*Z*）分辨率为 1 μm 的 *XYZ* 三维电动平台上，通过调节电动平台的运行速度来设置扫描速率。飞秒激光垂直于 BGO 晶体表面（10 × 9.5 mm^2），通过一个 40×的显微物镜（Leica，N.A. = 0.65），聚焦在晶体内部深度为~125 μm 处进行扫描。为研究单脉冲能量和写入痕迹间隔对光波导性能的影响，以不同参数写入四个光波导（Nos. 1-4），具体参数如表 3.1.1 所示。图 3.1.1 是采用金相显微镜（Axio Imager, Carl Zeiss）在透射光照射下拍摄的双线型光波导端面的图片。

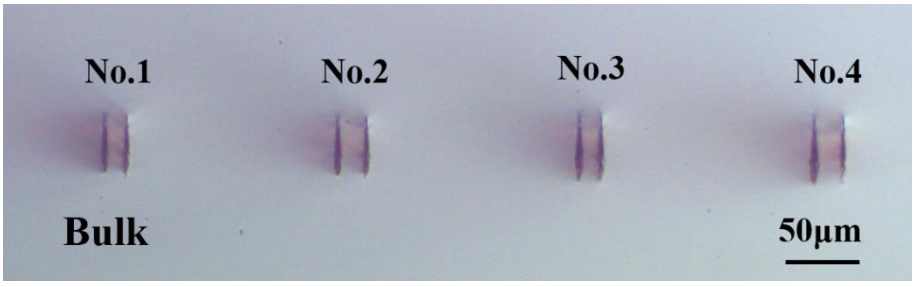

图 3.1.1 BGO 晶体双线型通道光波导的端面显微镜照片

表 3.1.1 飞秒激光写入 BGO 晶体制备双线型通道光波导的参数

波导	脉冲能量（μJ）	扫描速度（μm/s）	双线间隔（μm）
No. 1	1.68	50	15
No. 2	1.68	50	20
No. 3	2.52	50	15
No. 4	2.52	50	20

ii．导波特性的测量

利用端面耦合系统研究了波导的导波特性，其中光源采用波长 632.8 nm 的线偏振 He-Ne 激光，由半波片调控偏振方向，经由显微物镜（25×, N.A. = 0.4）聚焦后，激光被耦合入射到 BGO 晶体端面，通过调节放置晶体的 *XYZ* 三维调节平台使得激光入射到波导中，然后由另一个显微物镜收集出射光，使用 CCD 来采集分析波导的出射光的模式，利用功率计来测量出射光的功率。

iii．热退火处理

样品被放置在开放式退火炉中进行了五步退火处理，系统地研究了从 260ºC 到 600ºC 的退火行为，退火温度依次为 260，260，360，500，600ºC，退火时间均为 1 小时。每次退火后都对波导的导波特性进行重新测量。

3.1.2 结果与讨论

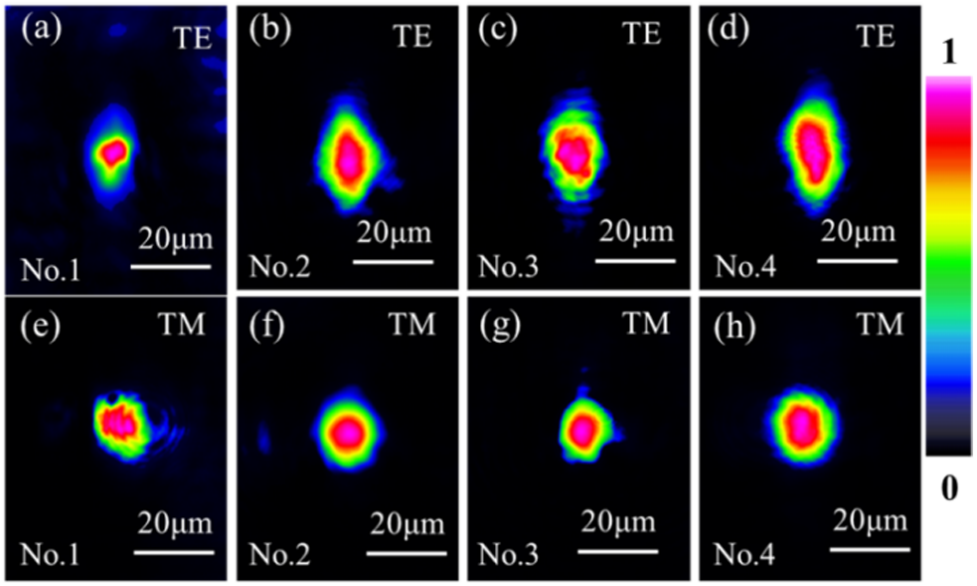

图 3.1.2 BGO 双线型通道光波导 Nos. 1-4 在 632.8 nm 波长下的近场光强分布

图 3.1.2 为 BGO 晶体双线型通道光波导在 632.8 nm 下的近场光强分布图，

波导 Nos. 1-4 均支持 TE 和 TM 偏振下的单模传输，而在先前报道的飞秒激光写入晶体所制备的双线型光波导中，如 Nd:YAG 晶体[9]和 Nd:GGG 晶体[10]，一般仅支持 TM 偏振方向的导波传输。通过对波导的最大受光角度的测试，可估算出在 TM 偏振光下，最大折射率变化值（Δn）分别为~9.4×10^{-4} (No. 1)，~9.8×10^{-4} (No. 2)，~9.7×10^{-4} (No. 3)，~1.86×10^{-3} (No. 4)，利用此数据重构了双线型波导 No. 4 的二维折射率分布图（图 3.1.3（a））。其中波导区域的折射率由于应力的挤压作用升高约$\Delta n_{core} = +4.6 \times 10^{-4}$，两条写入痕迹处折射率降低约$\Delta n_{track} = -1.4 \times 10^{-3}$。根据此折射率分布，基于有限差分光束传播法，利用模拟软件 Rsoft®[11]，模拟了双线型波导 No. 4 在 632.8 nm 波长的 TM 偏振光下的传输模式（图 3.1.3（b））。通过对比图 3.1.2（h）和图 3.1.3（b），可以证明实验结果和理论模拟结果相互吻合，进而验证了重构的折射率分布的合理性。

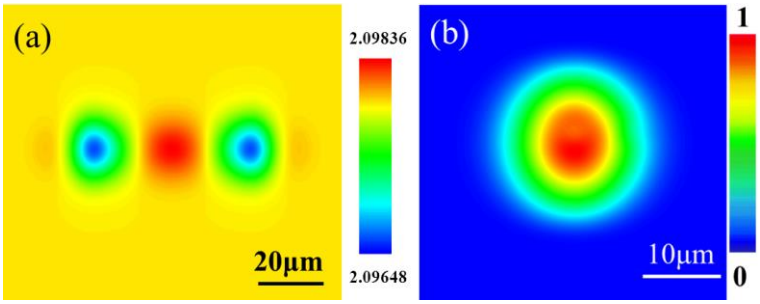

图 3.1.3 BGO 晶体双线型光波导 No. 4 的（a）折射率重构及（b）模拟近场光强分布

光波导的插入损耗主要由下述三个因素引起：耦合损耗，菲涅尔反射及传输损耗。其中，通过端面耦合所测得数据可以计算波导的插入损耗；波导的耦合损耗可以借助入射光模式和波导模式的转换效率进行估算，本节中不同尺寸的双线型光波导的耦合损耗分别为~1.7 dB (写入痕迹间隔为 15 μm 的 No. 1 和 No. 3)，或~2.7 dB (写入痕迹间隔为 20 μm 的 No. 2 和 No. 4)；光在两个端面发生菲尼尔反射引起的损耗计算结果为~1.2 dB。TE 偏振下四个双线型光波导的传输损耗（α）测量计算结果分别为：~26.1，~12.7，~20.5 和~11.1 dB/cm（Nos. 1-4）。较高的传输损耗可能是由于飞秒激光写入过程中引入的晶格缺陷造成的。退火处理是一种常用的优化光波导性能的方法。经过第一步 260℃下退火 1 小时处理，双线型光波导在 TE 偏振下的损耗分别降低至~17.0，~10.9，~16.4，和~8.8 dB/cm（Nos.

1-4）。第二步 260℃下退火 1 小时处理后，波导在 TE 偏振下的导波性质没有明显的改善。而在接下来的高温退火后，TE 偏振下波导不再支持 632.8 nm 激光的导波传输，波导结构被破坏。而在 TM 偏振下，由于双线型通道光波导在 TE 和 TM 偏振方向下的折射率分布不同，经过退火处理的光波导在 TM 偏振光下的传输损耗变化趋势不同于 TE 偏振方向，波导的损耗为~22.2，~11.5，~17.6，和~6.9 dB/cm（Nos. 1-4），经五步退火处理后，传输损耗大幅下降，结果如图 3.1.4 所示。

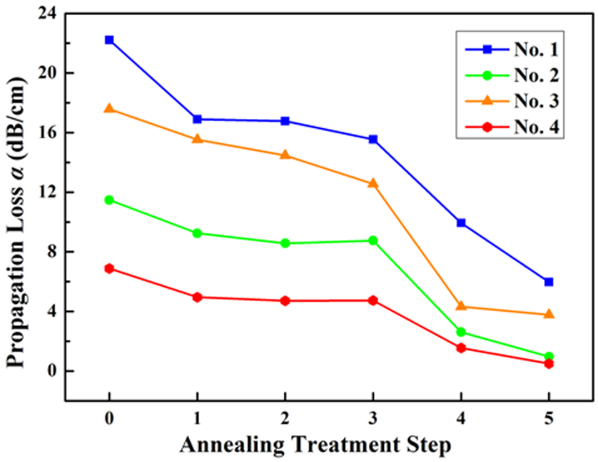

图 3.1.4 BGO 晶体双线型光波导 Nos. 1-4 在 TM 偏振光下经五步退火处理后的传输损耗。

结果如下：

第一步：260℃下退火 1 小时，光波导的传输损耗明显降低至~16.9，~9.2，~15.5 和~5.0 dB/cm（Nos. 1-4）；

第二步：260℃下退火 1 小时，光波导的传输损耗基本维持不变，表明波导在此温度下具有热稳定性；

第三步：360℃下退火 1 小时，维持第二步退火后的结果，表明波导在此温度下具有热稳定性；

第四步：500℃下退火 1 小时，光波导的传输损耗明显降低至~16.9，~9.2，~15.5 和~5 dB/cm（Nos. 1-4）；

第五步：600℃下退火 1 小时，光波导的传输损耗继续降低至~6.0，~1.0，~3.8，和~0.5 dB/cm（Nos. 1-4）。

根据文献中的报道[7]，飞秒激光写入 BGO 晶体中制备的双线型波导的传输损耗约为 4.2 dB/cm，小于本节中制备的光波导，这与飞秒激光制备的参数有关，例如文献中的飞秒激光脉冲能量为 2 mW，远远大于本节所采用的能量。但我们通过适当的热退火处理有效地将宽度为 15 μm 和 20 μm 的双线型光波导的传输损耗分别降低了 70%和 90%。其中，波导 No. 4 的波导损耗低至~0.5 dB/cm，表现出优异的导波性质。

通过比较不同参数制备的四个双线型通道光波导 Nos. 1-4 的传输损耗（α）的大小，可以得到 $\alpha_4 < \alpha_2 < \alpha_3 < \alpha_1$。分析光波导宽度和飞秒激光单脉冲能量对波导传输损耗的影响可得：

I) 光波导宽度（即两条飞秒写入痕迹之间的间隔）。波导宽度为 20 μm 的两个波导传输损耗小于波导宽度为 15 μm 的两个波导；

II) 单脉冲能量。具有相同宽度的两个波导，单脉冲能量高的，传输损耗低，即 $\alpha_4 < \alpha_2$ 和 $\alpha_3 < \alpha_1$，这可以归因于当单脉冲能量高时，两条写入痕迹之间的应力作用更明显。

3.1.3 小结

本实验采用飞秒激光写入技术，在 BGO 晶体中成功制备了双线型通道光波导，并通过端面耦合技术表征了波导的导波特性。结果表明，不同的飞秒激光参数制备的双线型通道光波导 Nos. 1-4 的导波性质不同，但均支持 TE 和 TM 偏振光下的单模传输。波导的传输损耗较高，经过一系列的退火处理优化，波导的传输性能均得到了大幅提升，其中单脉冲能量为 2.52 μJ，写入痕迹间隔为 20 μm 的光波导 No. 4 在 632.8 nm 的 TM 偏振光下的传输损耗可以低至 0.5 dB/cm，为本节实验条件下的最优化制备参数。本工作表明飞秒激光写入所制备的 BGO 晶体双线型通道光波导性质优异，有望利用于制备集成光学器件。本节相关工作结果发表于 *Applied Optics* **52**, 3713–3718 (2013)。

3.2 BGO 晶体包层通道光波导

在上一节实验中，利用飞秒激光写入技术制备了双线型通道光波导，本节实验中我们利用飞秒激光写入的方法在 BGO 晶体中制备包层通道光波导，并测试波导的导波特性。包层光波导和双线型光波导相比，具有偏振不敏感性。

3.2.1 实验过程

本实验中选用六个表面均经光学抛光加工处理的 BGO 晶体，尺寸为 10 × 9.5 × 2 mm^3。具体实验过程如下：

i. 波导的制备

在波导制备上，依然采用西班牙萨拉曼卡大学的钛宝石飞秒激光系统，其基本工作参数如 3.1 节所述。不同的参数为，单脉冲能量为 1.68 μJ，扫描速率为 500 μm/s，相邻写入痕迹间距约为 3 μm。图 3.2.1 展示了 BGO 晶体包层通道光波导的显微镜图片，波导位于由 75 条相互平行但位于不同深度的飞秒写入痕迹所包围的区域内部，直径约为~100 μm。

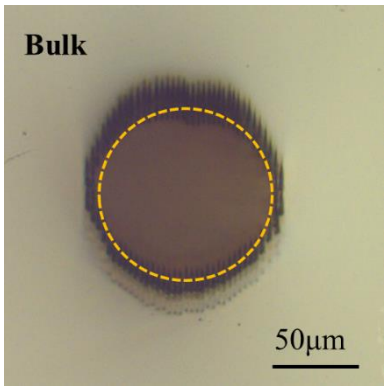

图 3.2.1 飞秒激光写入 BGO 晶体所制备的包层通道光波导的显微镜图片

ii. 导波特性的测量和热退火处理

同 3.1.1 节中，通过端面耦合技术对 BGO 晶体包层通道光波导的导波性质进行了表征，并使用热退火处理对波导的性质进行了优化。

3.2.2 结果与讨论

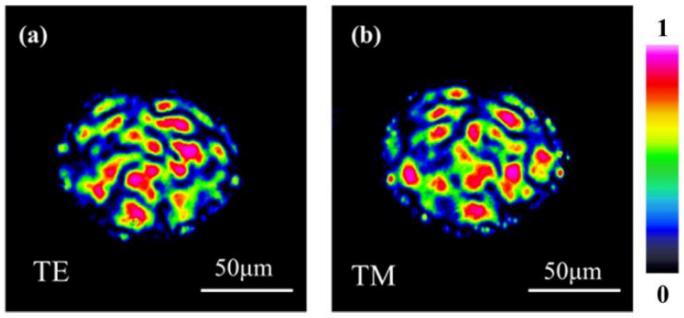

图 3.2.2 BGO 晶体包层光波导在（a）TE 和（b）TM 偏振下的近场光强分布图

图 3.2.2 为 BGO 晶体包层光波导在 632.8 nm 波长的 TE 和 TM 偏振光下的近场光强分布图。TE 和 TM 偏振下的模式分布类似，均为多模传输。该包层光波导的耦合损耗和传输损耗为分别为~1.2 dB/cm 和~3.7 dB/cm，并且在 TE 和 TM 下无差别。经过 260℃退火处理一个小时后，降为~3.1 dB/cm；继续在 260℃退火处理一个小时后，降为~2.1 dB/cm，表明经过退火处理，飞秒激光写入过程中引入的晶格缺陷得到了修复；而在下一步的 360℃退火处理后，波导导波模式被破坏，损耗升高至~4.2 dB/cm；进一步地，500℃和 600℃退火处理彻底破坏了波导结构，波导不再支持 632.8 nm 下的导波传输。本节飞秒激光写入的速率采用 500 μm/s，远小于 3.1 节中的 BGO 晶体双线型通道光波导所采用的 50 μm/s，这大大减少了加工时间，但由飞秒激光引起的应力变化也大幅减小。当使用高温下退火时，应力引起的折射率变化得到了恢复，飞秒写入区域与衬底材料折射率差别变小，无法支持光的传输，即波导退化（擦除）。通过对飞秒激光参数的优化，包层光波导的导波性质可以得到提升。

3.2.3 小结

本实验采用飞秒激光写入技术，在 BGO 晶体中制备了包层通道光波导结构。包层光波导具有偏振不敏感性，支持各个偏振方向下的导波传输，且飞秒激光写入痕迹组成一个准连续的折射率降低的包层，更好地将光限制在波导内部传输。260℃退火处理可将波导的传输损耗降至~2.1 dB/cm。本节相关工作结果发表于 *Applied Optics* **52**, 3713–3718 (2013)。

3.3 BGO 晶体折射率升高型通道光波导

前面 3.1 和 3.2 节飞秒激光写入制备的双线型和包层光波导的共同特征为在飞秒写入痕迹处折射率降低，由此降低区域包围的区域为波导区域。本节采用同样的飞秒激光系统，通过改变写入参数，在 BGO 晶体中直接写入折射率升高的痕迹，形成通道光波导，并对其导波性质进行研究。该类波导具有直接写入，形态灵活可调的优点。

3.3.1 实验过程

本实验中所选用的 BGO 晶体，尺寸为 $10 \times 10 \times 2\ mm^3$，其一对表面及一对端面均经过光学抛光处理。具体实验过程如下：

i. 波导的制备

依然采用西班牙萨拉曼卡大学的钛宝石飞秒激光系统，激光的基本参数不变，中心波长为 800 nm，脉宽为 120 fs，重复频率为 1 kHz。飞秒激光垂直于 BGO 晶体表面（$10 \times 10\ mm^2$），聚焦在晶体内部深度为~50 μm 处进行扫描。为减少加工时间的同时优化两个连续的飞秒激光脉冲之间的空间重叠，扫描速率设定为 500 μm/s。为实现飞秒激光写入区域折射率升高，并支持在 4 μm 中红外波长下的导波，我们对相邻写入痕迹之间的间隔及脉冲能量这两个加工进行了调试，其中写入痕迹间隔以 100 nm 的精度可调，单脉冲能量可通过经中性滤波片、半波片以及线偏振片等光学元件进行连续调节。最终，单脉冲能量设定为 0.14 μJ、相邻写入痕迹间隔采用 3 μm 时达到最优化。

在上述最优化飞秒激光参数下，飞秒激光写入痕迹为条状，长度约为 18.5 μm，宽度约为 1 μm，写入区域折射率升高。为制备尺寸适当的，具有对称性的通道光波导，我们采用多次重复扫描技术，对晶体进行多次扫描，多条写入痕迹相连形成一个折射率升高的矩形区域，周围的衬底区域的折射率相对较低，成功形成通道光波导。本实验中，我们制备了两个矩形光波导结构，各由 6 条和 24 条写入痕迹组成，尺寸分别为 $16.4 \times 18.3\ \mu m^2$ 和 $32.2 \times 37.0\ \mu m^2$，其端面显微镜图如图 3.3.1 所示。

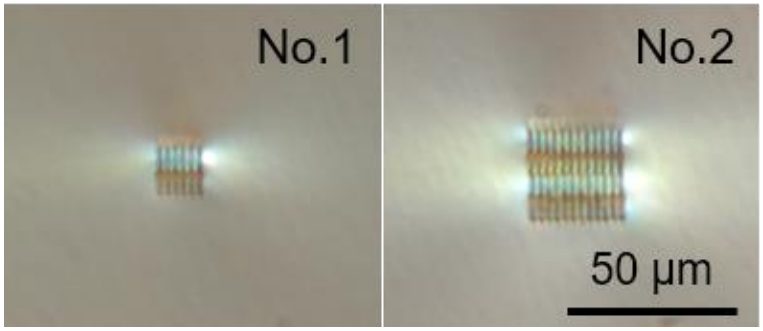

图 3.3.1 BGO 晶体折射率升高型光波导的显微镜照片，写入痕迹数量分别为 6 条和 24 条

ii. 导波特性的测量

利用端面耦合系统，光源为可调谐激光系统（MIRTM 8025, Daylight Solutions, Inc.）所提供的波长为 4 μm 的线偏振光，由偏振片调控偏振方向，经由中红外显微物镜（ZnSe, LFO-5-12-3.75, N.A. = 0.13）聚焦后，激光被耦合入射到 BGO 晶体端面，通过调节固定晶体的 *XYZ* 三维调节平台使得激光入射到波导的端面，然后由另一中红外显微物镜收集由波导另一端面的出射光，使用中红外 CCD（WinCamD, DataRay Inc.）来分析记录波导的传输模式，使用中红外功率计来测量出射激光的功率。通过计算入射光束和波导模式的重合，对波导的耦合效率进行了估算，进而计算在 4 μm 下的通道光波导的传输损耗。

3.3.2 结果与讨论

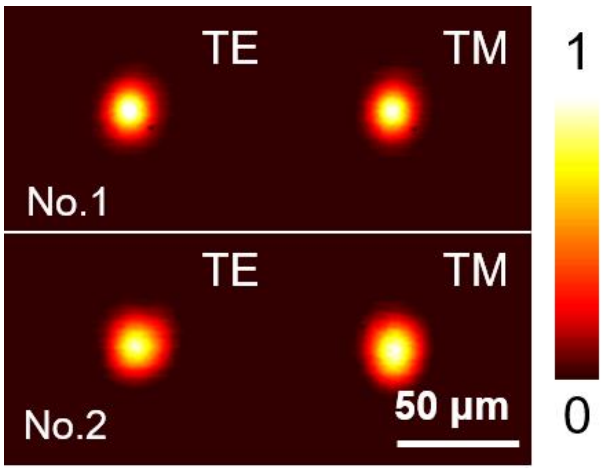

图 3.3.2 BGO 晶体折射率升高型光波导在 4 μm 下的近场光强分布图

图 3.3.2 为 BGO 晶体通道光波导 Nos. 1-2 在 4 μm 下的近场光强分布图，两

个不同尺寸的矩形波导均支持 TE 和 TM 偏振下的单模传输。而先前报道的飞秒激光写入晶体所制备的折射率升高型光波导中，一般仅支持某一特定偏振方向的导波传输[12,13]。同时通过对波导的最大受光角的测试，可估算出在飞秒激光写入痕迹处，即波导处，最大折射率变化值（Δn）约为$(5.3\pm1)\times10^{-3}$。

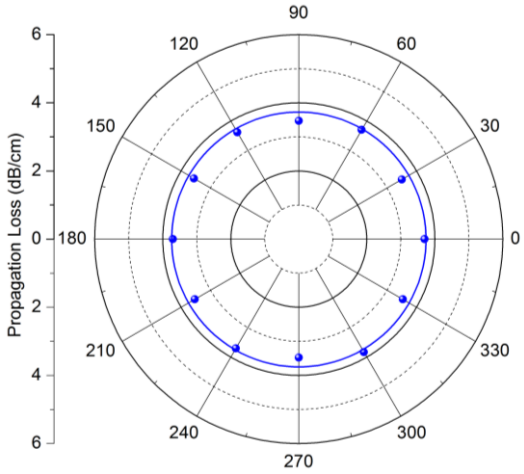

图 3.3.3 BGO 晶体折射率升高型光波导 No. 2 在各偏振方向耦合下的传输损耗

通过端面耦合所测得数据可以计算波导的插入损耗，波导的耦合损耗估算为~0.97 dB，两个端面的菲尼尔反射引起的损耗为~1.07 dB，计算可得波导 No. 1 和 No. 2 在 4 μm 的 TE/TM 偏振光下的传输损耗分别 3.39 和 3.70 dB/cm (TE)，3.32 和 3.47 dB/cm (TM)。TE 和 TM 偏振方向下的传输损耗差别小于~7%，表明该波导对光的偏振不敏感。图 3.3.3 为 BGO 晶体通道光波导 No. 2 在不同偏振方向的 4 μm 入射光耦合下的传输损耗，该结果进一步证明了，BGO 晶体通道光波导在任意偏振角度下传输损耗近乎相等，具有偏振不敏感性。

3.3.3 小结

本实验采用飞秒激光写入技术，在 BGO 晶体中成功制备了折射率升高型通道光波导。通过端面耦合技术表征了波导的导波特性。结果表明，与已有报导的飞秒激光写入晶体制备折射率升高型光波导相比，BGO 晶体通道型光波导结构稳定，支持各个偏振方向的中红外波段导波，具有优异的导波性能。本节相关工作结果发表于 *Optics Express* **22**, 31293–31298 (2014)。

3.4 BGO 晶体波导分支器

本文 3.3 节所制备的折射率升高型通道光波导制备快捷、性质优异，有利于制备复杂的器件。本节在 BGO 晶体中制备了二维（1 × 2）及三维（1 × 3, 1 × 4）的波导分支器，实现了 4 微米的中红外激光下的波导分支功能。

3.4.1 实验过程

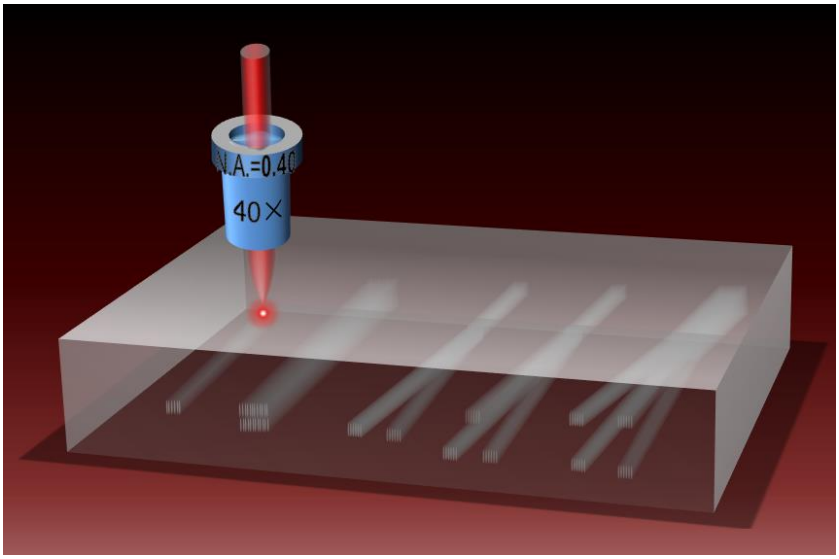

图 3.4.1 飞秒激光写入 BGO 晶体制备波导分支器的示意图

本实验中所选用的 BGO 晶体，尺寸为 10 × 10 × 2 mm^3。具体实验过程如下：

分支器的制备采用的仪器和参数均与 3.3 节相同，图 3.4.1 为装置示意图。对于二维分支器（1 × 2），输入端由 6 条写入痕迹组成（同 3.3 节中的通道光波导 No. 1），输入端长 3 mm，在 3 mm 处分为两条对称的分支，夹角为 0.4°，深度和输入端相同，两条分支输出端的间距为 50 μm。该写入过程通过电脑编程控制三维样品台的行进方向和路程，结合激光器开关的控制，一次可写入多条分支器结构。进一步地，我们设计了三维分支器（1 × 3, 1 × 4），其输出端各分支均与 3.3 节中波导 No. 1 相同，由 6 条扫描痕迹组成，且各个分支端面组成矩形，具有对称性，其中 1 × 4 分支器的输出端组成一个 2 × 2 的波导阵列。

波导分支器的参数如表 3.4.1 所示：

表 3.4.1 飞秒激光写入制备 BGO 晶体波导分支器的参数

分支器	结构	输入端长度（mm）	输入端扫描次数	分支扫描次数	夹角（°）	输出端相连分支间距（μm）
Sp. 1	1 × 2	3	6	6	0.415	50
Sp. 2	1 × 3	3	6	6	0.415	50
Sp. 3	1 × 4	3	24	6	0.415	50
Sp. 4	1 × 4	3	24	6	0.830	100

在 BGO 晶体中制备波导分支器后，我们对样品进行了抛光，样品的最终尺寸为：10 × 9.9 × 2 mm^3。利用显微镜观察了分支器的形态。图 3.4.2 展示了 1 × 2 分支器 Sp. 1 的输入、输出端面和上表面俯视图。利用端面耦合系统，对分支器在 4 μm 波长激光下的导波特性进行了研究。

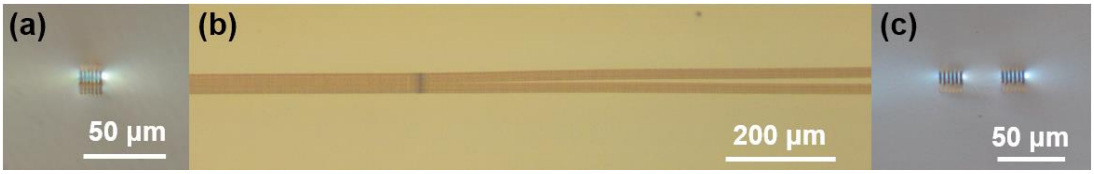

图 3.4.2 BGO 晶体波导分支器 Sp. 1 的显微镜照片（a）输入端，（b）俯视图，（c）输出端

3.4.2 结果与讨论

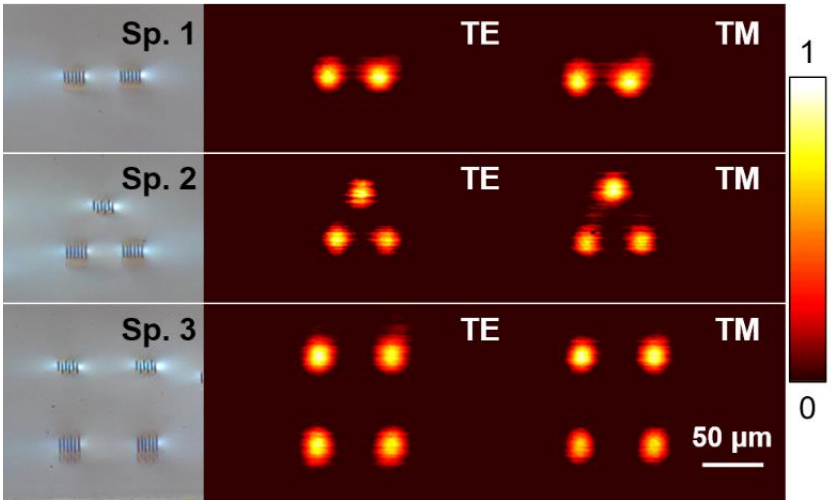

图 3.4.3 BGO 波导分支器 Sps. 1-3 的输出端端面显微镜图及在 4 μm 下的近场光强分布

图 3.4.3 为 BGO 晶体波导分支器 Sps. 1-3 的输出端端面显微镜图及在 4 μm 下的近场光强分布图，均支持 TE 和 TM 偏振光下的单模分支传输。根据 3.3 节中重构的飞秒激光写入区域的折射率变化，使用模拟软件 Rsoft®绘制具有实际尺寸和折射率分布的分支器结构以模拟分支器中 4 μm 激光的传输过程，图 3.4.4 展示了分支器 Sp. 4 的模拟结果。首先，由输出端近场光强分布可以看出实验结果和模拟结果高度吻合；其次，由 TE 偏振下的 4 μm 激光在分支器中的传输模式演变图可以看出，光束由一束分为四个分支后依然呈单模模式，并沿着分支继续传输，最终在出射端形成 2 × 2 阵列模式。通过对各个分支的出射光分析，得出各个分支的光强分支比例为 27 : 26 : 23 : 24。

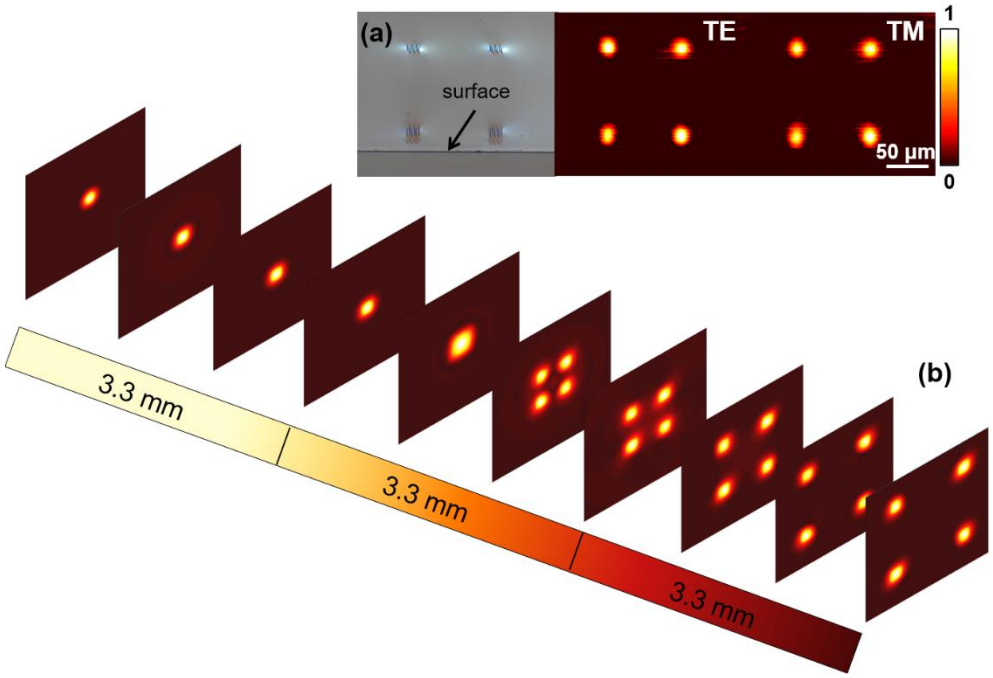

图 3.4.4 BGO 晶体波导分支器 Sp. 4 的（a）输出端端面显微镜图及在 4 μm 下的近场光强分布，（b）模拟 4 μm 激光在波导分支器中的传输模式演变图

表 3.4.2 飞秒激光写入制备 BGO 晶体波导分支器的传输损耗 α (dB/cm)

	Sp. 1	Sp. 2	Sp. 3	Sp. 4
TE	3.35	3.70	3.81	3.95
TM	3.23	3.47	3.59	3.71

分支器的传输损耗计算结果如表 3.4.2 所示，平均大小约为 3.6 dB/cm，且 TE 和 TM 偏振下差别较小，约为 7%。通过进一步对在各个偏振光下的传输损耗的研究表明，BGO 晶体飞秒激光波导分支器具有偏振不敏感型，如图 3.4.5 所示，在不同偏振方向下的传输损耗差别很小。分支器在将一束光束分支为多束时，由于光线的偏折，入射端与分支之间的耦合等因素，会产生额外的损耗，通过对比具有相同折射率构造的波导和分支器的传输损耗，我们可以得到三维分支器的分支损耗小于~0.3 dB，该值远远小于在熔融石英中报道的 1 × 3 分支器的分支损耗（~6 dB）[14]。

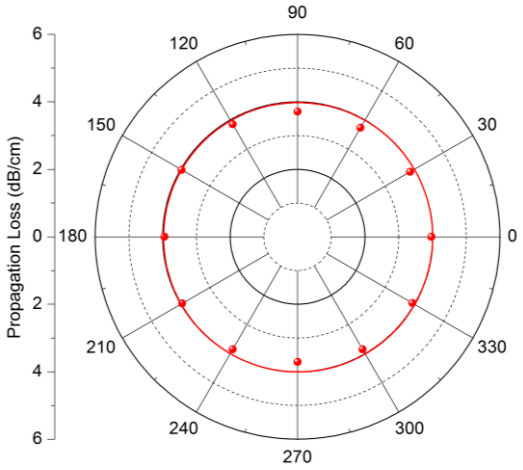

图 3.4.5 BGO 晶体 1 × 4 波导分支器 Sp. 4 在不同偏振方向下的传输损耗

3.1.3 小结

本实验采用飞秒激光写入技术在 BGO 晶体中成功制备了二维及三维波导分支器。结果表明，1 × 2，1 × 3，1 × 4 波导分支器均支持单模传输，具有偏振不敏感性，且分支比例接近 1:1，分支损耗较小约为~0.3 dB。本实验所制备的 BGO 波导分支器性能优异，可作为有效的分支器件。本节相关工作结果发表于 *Optics Express* **22,** 31293–31298 (2014)。

参考文献

1. 吕刚，陈淑芬，孔金学，蔡起善. 压电与声光 **5**, 16–21 (1983).
2. 廖晶莹，叶崇志，杨培志. 化学研究 **15**, 52–58 (2004).
3. S. M. Mahdavi, P. J. Chandler, and P. D. Townsend, J. Phys. D **22**, 1354–1357 (1989).
4. J. Yang, C. Zhang, F. Chen, S. Akhmadaliev, and S. Q. Zhou, Appl. Opt. **50**, 6678–6681 (2011).
5. I. Bányász, S. Berneschi, N. Q. Khánh, T. Lohner, K. Lengyel, M. Fried, Á. Péter, P. Petrik, Z. Zolnai, A. Watterich, G. Nunzi-Conti, S. Pelli, and G. C. Righini, Nucl. Instrum. Methods Phys. Res. Sect. B **286**, 8084 (2012).
6. R. He, Sh. K. Vanga, A. A. Bettiol, and F, Chen, Opt. Eng. **54**, 057108 (2015).
7. B. Qian, Y. Liao, G. P. Dong, F. F. Luo, L. B. Su, S. Z. Sun, and J. R. Qiu, Chin. Phys. Lett. **26**, 070601 (2009).
8. C. Miese, S. Gross, M. J. Withford, and A. Fuerbach, Opt. Mater. Express **5**, 323–329 (2015).
9. J. Siebenmorgen, K. Petermann, G. Huber, K. Rademaker, S. Nolte, and A. Tünnermann, Appl. Phys. B **97**, 251–255 (2009).
10. C. Zhang, N. N. Dong, J. Yang, F. Chen, J. R. Vázquez de Aldana, and Q. M. Lu, Opt. Express **19**, 12503–12508 (2011).
11. http://www.rsoftdesign.com
12. J. Burghoff, C. Grebing, S. Nolte, and A. Tünnermann, Appl. Phys. Lett. **89**, 081108 (2006).
13. A. Rodenas and A. K. Kar, Opt. Express **19**, 17820–17833 (2011).
14. K. Song, Y. Fan, and Y. H. Zhang, Microw. Opt. Technol. Lett. **49**, 595–597 (2007).

第四章 飞秒激光写入掺钕钒酸钇晶体光波导调 Q 脉冲激光

掺钕钒酸钇（Nd:YVO_4）属四方晶系[1]，锆石英结构，正单轴晶，晶格常数为 a = b = 0.712 nm，c = 0.629 nm，密度为 4.22 g/cm^3，1064 nm 波长下折射率 n_o = 1.9573，n_e = 2.1652。Nd:YVO_4 晶体是一种性能优良的激光材料[2]，与最常用的固体激光晶体 Nd:YAG 相比具有以下优势：受激发射截面大，吸收系数高，对 809 nm 波长存在很强的宽吸收带，吸收光谱宽，对泵浦波长依赖性小，与 Nd:YAG 晶体相比有更高的斜效率，是激光二极管泵浦全固态微小型激光器的理想工作材料，在材料加工、波谱学、医学检测、光通讯、和数据存储等领域有着广泛应用[3-7]。

迄今为止，科学家采用离子注入、飞秒激光加工等多种技术在 Nd:YVO_4 晶体中制备平面或条形光波导，并实现连续波导激光的输出[8-13]。

石墨烯是一种由以 sp2 杂化方式形成的蜂窝状平面薄膜，只有一个原子层的厚度，是近年来备受关注的新型二维材料，被广泛研究和应用于在电子学、光学、磁学、生物医学、催化和储能等领域[14-18]。石墨烯几乎完全透明，单层石墨烯的吸收率为 2.3%，而在强光的照射下，石墨烯具有可饱和吸收性，其可饱和阈值低，调制深度高，可作为可饱和吸收体实现脉冲激光的产生[19-22]。

本章主要介绍利用飞秒激光写入技术在 Nd:YVO_4 晶体中制备双线型、包层及双包层光波导结构，并通过端面耦合系统对其导波特性、激光特性进行研究，利用石墨烯作为可饱和吸收体，在波导结构中实现调 Q 波导激光的产生。

4.1 Nd:YVO_4 晶体双线型通道光波导调 Q 脉冲激光

本实验利用飞秒激光写入技术在 Nd:YVO_4 晶体中制备双线型通道光波导，并利用石墨烯作为可饱和吸收体，实在波导结构中实现调 Q 激光振荡。

4.1.1 实验过程

本实验中所用的 Nd:YVO_4 晶体为 *a* 切向，Nd^{3+}离子掺杂浓度为 2 at.%，尺寸为 2 (*a*) × 7 (*b*) × 9 (*c*) mm^3。其六个表面均经光学抛光加工处理。具体实验过程如下：

i．波导的制备

首先利用西班牙萨拉曼卡大学的钛宝石飞秒激光系统在 Nd:YVO_4 晶体中写入双线型结构。飞秒激光器基本工作参数与前面章节相同，飞秒激光沿晶体 *a* 轴入射，能量采用 2.1 μJ，经显微物镜（40×, N.A. = 0.65）聚焦至样品表面下深度约~110 μm，扫描方向沿 *b* 轴，扫描速率为 50 μm/s。在不同的深度（*a* 轴方向）和不同的横向距离（*c* 轴方向）处，分别写入四条痕迹，其中两横向写入痕迹间距为 20 μm，两纵向写入痕迹首尾相连，形成两列平行痕迹，成为双线型结构。在写入痕迹附近由于应力的挤压作用折射率升高。

ii．波导的导波性质测量

采用 1064 nm 的连续激光，基于端面耦合系统，利用显微物镜将激光耦合进波导中，利用另一显微物镜对波导的出射光进行采集后分析。

iii．石墨烯调 Q 激光的产生

基于端面耦合系统，我们采用可调谐钛宝石激光器（Coherent 110, USA）作为泵浦源，根据Nd^{3+}离子吸收峰特点，泵浦光波长被调至 820 nm，泵浦激光经半波片和格兰泰勒棱镜进行偏振方向和功率调节后，采用焦距为 25 mm 的球面凸透镜将泵浦光聚焦于波导入射端面，谐振腔由光学抛光的入射端面和出射端面组成，出射激光经 20×长工作距离显微镜物镜（N.A. = 0.40）收集，经过滤波片、孔阑的元件后，由 IR CCD、光谱仪等仪器分别进行采集测量。由此激光泵浦系统，可以实现连续激光的输出。

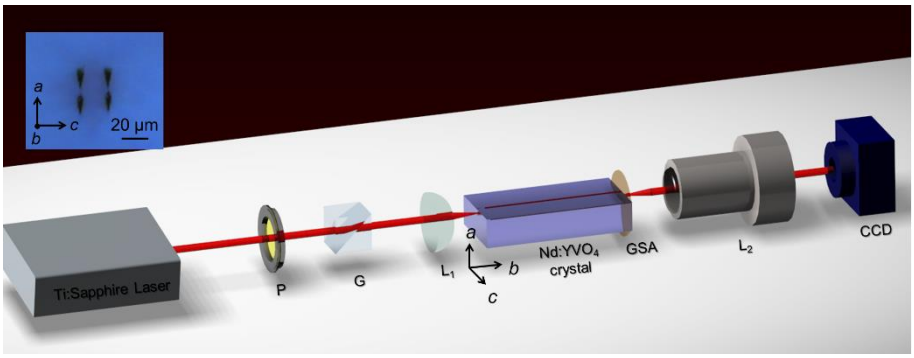

图 4.1.1 石墨烯调 Q 激光实验装置示意图，P：半波片，G：格兰泰勒棱镜，L_1：透镜，GSA：附有石墨烯薄膜的石英片，L_2：显微物镜。插图为波导端面显微镜图

为进行调 Q 产生脉冲激光，我们选用石墨烯作为可饱和吸收体，首先由 XFNANO Materials Tech Co., Ltd, Nanjing 通过气相沉积法将多层石墨烯生长在金属基底材料（铜/镍）上，后由 Raman 谱测定石墨烯的层数（本实验采用 5 层石墨烯），再将石墨烯薄膜转移到厚度约为 2 毫米的圆形石英基底上。覆有石墨烯薄膜的石英片对 1064 nm 光的透过率为 81%。利用压力将石墨烯薄膜镜片紧密地贴在 $Nd:YVO_4$ 晶体的出射端面。出射激光通过 CCD、功率计、分辨率为 0.4 nm 的光谱仪和示波器（Tektronix TDS 202 2B, 200 MHz）等仪器进行测量分析。图 4.1.1 为石墨烯调 Q 产生脉冲激光的实验装置图。

4.1.2 结果与讨论

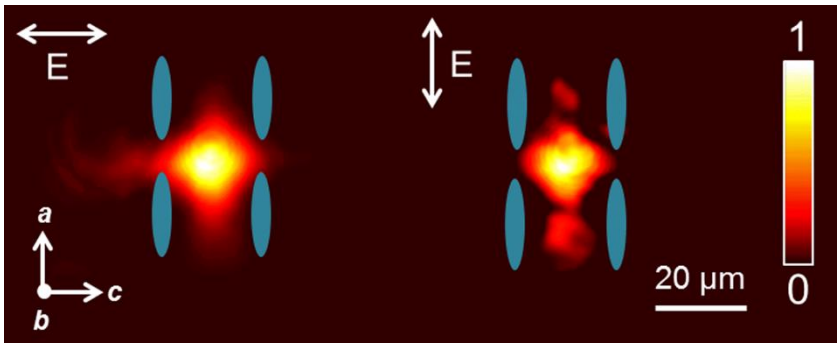

图 4.1.2 $Nd:YVO_4$ 晶体通道波导连在 1064 nm 下的近场模式分布。蓝色区域标示了飞秒激光写入痕迹的位置

在飞秒激光写入痕迹处折射率降低，晶格扩张，进而产生应力作用，使得写

入痕迹之间区域折射率升高，形成波导。图 4.1.2 为 Nd:YVO_4 晶体通道光波导在 1064 nm 的 TE 和 TM 偏振光下的近场模式分布，均呈现单模模式。波导在 TE 和 TM 偏振光下的传输损耗分别为~1.2 dB/cm 和~1.9 dB/cm。

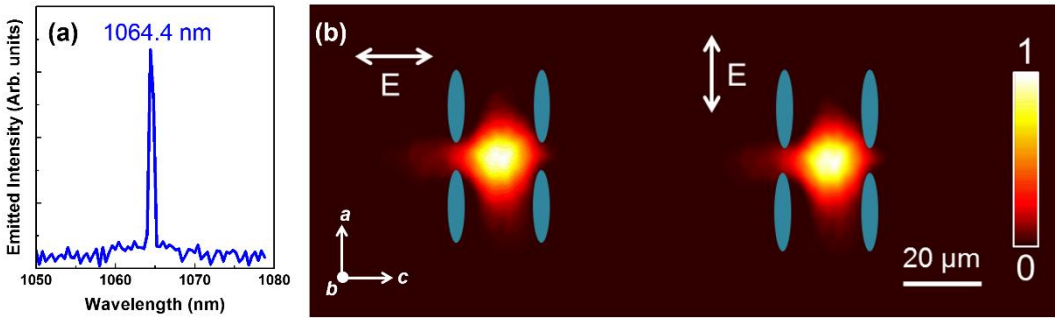

图 4.1.3（a）Nd:YVO_4 晶体波导激光的光谱图；（b）波导激光在 TE 和 TM 偏振下的近场模式分布

利用端面耦合系统，采用 820 nm 连续激光泵浦，多层石墨烯作为可饱和吸收体，在 Nd:YVO_4 通道光波导中实现了调 Q 脉冲激光的输出。图 4.1.3 为波导经石墨烯调 Q 产生的脉冲激光的表征。其中产生脉冲激光的中心波长为~1064.4 nm（图 4.1.3（a）），对应稀土离子 Nd^{3+}的 $^4F_{3/2}\rightarrow{}^4I_{11/2}$ 能级跃迁，半高宽为 0.8 nm，产生激光的近场模式分布在 TE 和 TM 两个垂直的偏振方向均为单模。

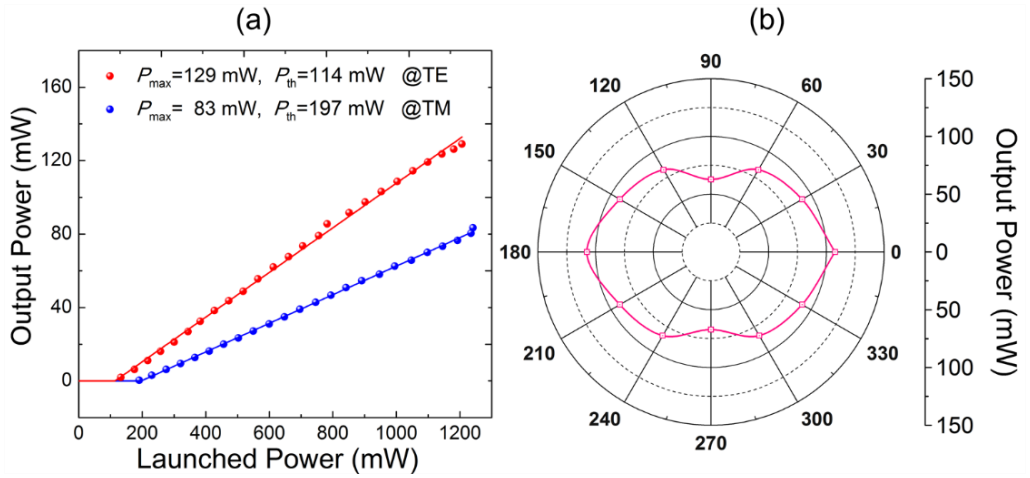

图 4.1.4（a）TE 和 TM 偏振下 Nd:YVO_4 晶体通道波导调 Q 脉冲激光的平均输出功率随泵浦光功率的变化，实线为实验数据的线性拟合；（b）在不同偏振的 950 mW，820 nm 激光泵浦下产生的 Nd:YVO_4 晶体波导调 Q 脉冲激光的平均输出功率分布

脉冲激光的平均输出功率随入射光光强变化如图 4.1.4（a）所示。通过对实验结果的拟合分析可得，在 TM 偏振方向下产生激光的阈值为 197 mW，在最大泵浦功率为 1.24 W 时，激光的最大平均输出功率为 83 mW，光转换效率为 6.7%；TE 偏振方向下产生激光的阈值较低，为 114 mW，在最大泵浦功率达到 1.2 W 时，得到激光的最大平均输出功率为 129 mW，光转换效率为 10.8%。TE 偏振下的波导激光性能优于 TM 偏振，这是由于 TE 偏振下的传输损耗低，可归因于飞秒激光写入过程引起的各向异性。对此我们进一步的研究了同一功率不同偏振的泵浦光下产生激光的平均输出功率的大小，如图 4.1.4（b）所示，TE 偏振下输出功率最高，TM 偏振下输出功率最低。

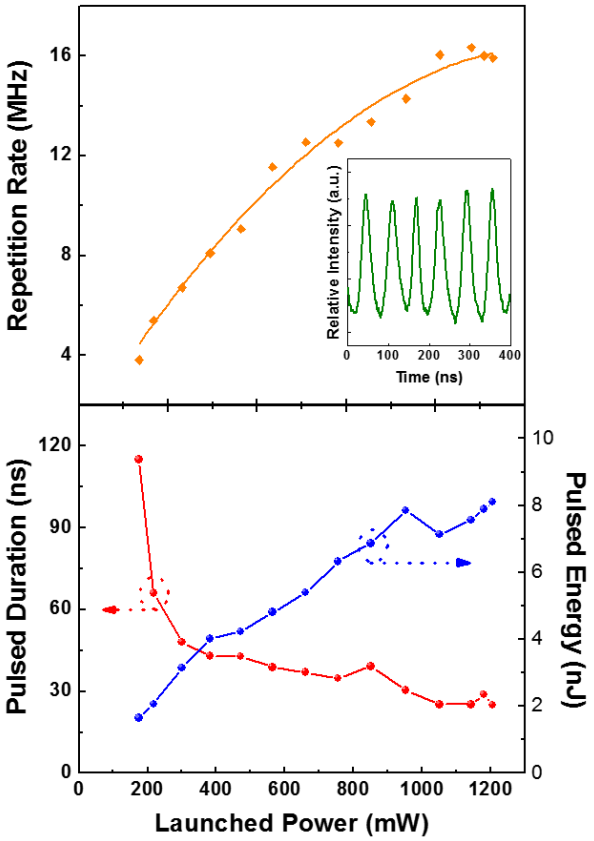

图 4.1.5 TE 偏振下调 Q 脉冲激光的重复频率、脉冲宽度和单脉冲能量随泵浦功率的变化。插图为一个典型的调 Q 脉冲激光的脉冲序列，对应的泵浦光功率为 1.05W，平均输出功率 114 mW，重复频 16.0 MHz，脉冲宽度 25.2 ns，单脉冲能量 7.1 nJ

对激光脉冲的分析表明，在泵浦功率最大时，TE 和 TM 偏振下可达到的最

小脉冲宽度、最高重复频率、最大单脉冲能量分别为 25.0 ns, 16.3 MHz, 8.1 nJ @ 1.2 W （TE）和 31.5 ns, 13.8 MHz, 6.0 nJ @1.24 W （TM）。图 4.1.5 为 Nd:YVO_4 晶体波导中调 Q 激光重复频率、脉冲宽度、脉冲能量在 TE 偏振下随泵浦功率变化的情况。结果表明，脉冲激光的重复频率随着泵浦功率升高，由 3.8 MHz 增长至 16.3 MHz，变化趋势近似呈典型的线性增长，脉冲激光的脉宽有 115.0 ns 下降至 25.0 ns，单脉冲能量由 1.6 nJ 升至 8.1 nJ。随着泵浦功率增加，调 Q 激光脉冲宽度逐渐减小，脉冲能量逐渐增加，这主要是由于入射激光功率增加，谐振腔内光密度增强，在石墨烯可饱和吸收作用下，使得脉冲激光周期减小，脉冲宽度降低，最终脉冲能量增加。

4.1.3 小结

本实验采用飞秒激光写入技术，在 Nd:YVO_4 晶体中制备双线型通道光波导。基于端面耦合系统，利用多层石墨烯作为可饱和吸收体，成功实现脉冲重复频率达 16.3 MHz，脉冲能量为 8.1 nJ，脉冲宽度仅为 25ns 的调 Q 波导激光输出。本节相关工作结果发表于 *Optics Materials* **46**, 414–417 (2015)。

4.2 Nd:YVO_4 晶体单包层及双包层波导调 Q 脉冲激光

在上一节的实验中，利用飞秒激光写入技术，在 Nd:YVO_4 晶体中制备了双线型通道光波导。本节实验在 Nd:YVO_4 晶体中制备包层及双包层波导，实现脉冲波导激光振荡，相比于双线型通道光波导，双包层波导具有更优良的导波和激光性能。

4.2.1 实验过程

本实验中所用的 Nd:YVO_4 晶体为 *a* 切向，Nd^{3+}离子掺杂浓度为 2 at.%，尺寸为 2 (*a*) × 7 (*b*) × 9 (*c*) mm^3。其六个表面均经光学抛光加工处理。具体实验过程如下：

i. 波导的制备

本节实验依然利用西班牙萨拉曼卡大学的钛宝石飞秒激光系统在 Nd:YVO_4 晶体中进行写入包层及双包层结构。飞秒激光器基本工作参数与 4.1 节相同。为保证形成准连续的写入痕迹的同时降低应力累积过程，缩减加工时间，扫描速率设定为 500 μm/s。根据经验，相邻写入痕迹之间的间隔设定为 3 μm。波导的端面显微镜图如图 4.2.1 所示，分别制备了直径为 114 μm 和 42 μm 的两个包层光波导（No. 1 和 No. 2），以及由内外两个同心圆组成的双包层波导 No. 3，其内外径分别为 42 μm 和 114 μm。

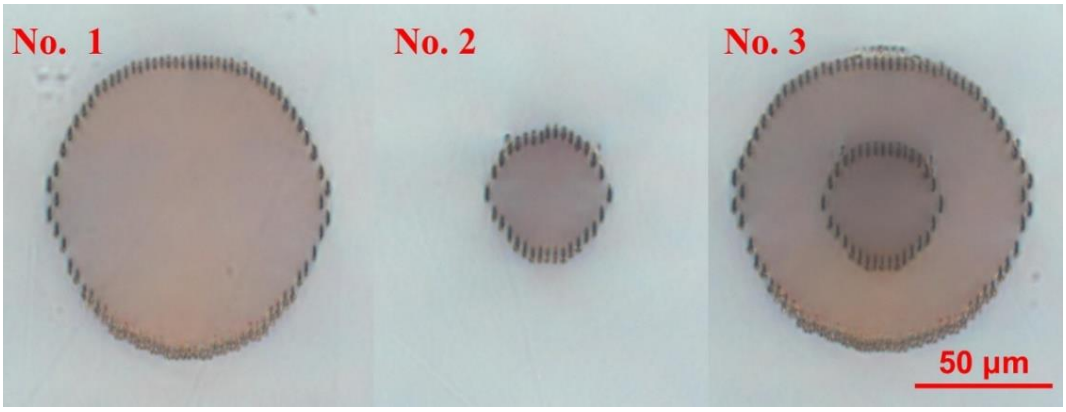

图 4.2.1 包层及双包层光波导 Nos. 1-3 的端面透射显微镜图像

ii．波导导波特性测试

基于端面耦合系统，利用 1064 nm 的连续激光器作为光源，利用显微物镜（20×, N.A. = 0.40）将入射光耦合进波导，利用另一显微物镜对出射激光进行采集。利用格兰泰勒棱镜调节入射光的偏振。

iii．调 Q 脉冲激光的产生

采用多层石墨烯作为可饱和吸收体，基于端面耦合系统实现调 Q 脉冲激光的输出，实验装置如 4.1 节图 4.1.1 所示。图 4.2.2 展示了附有石墨烯薄膜的石英片。

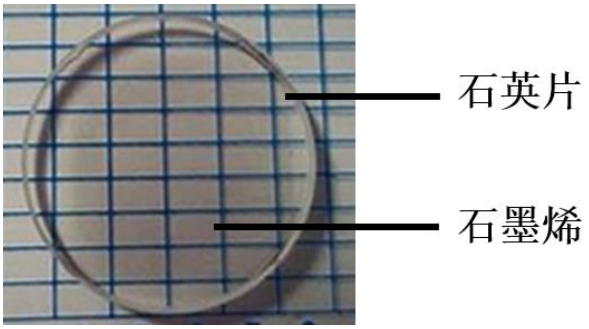

图 4.2.2 附有多层石墨烯薄膜的石英片

4.2.2 结果与讨论

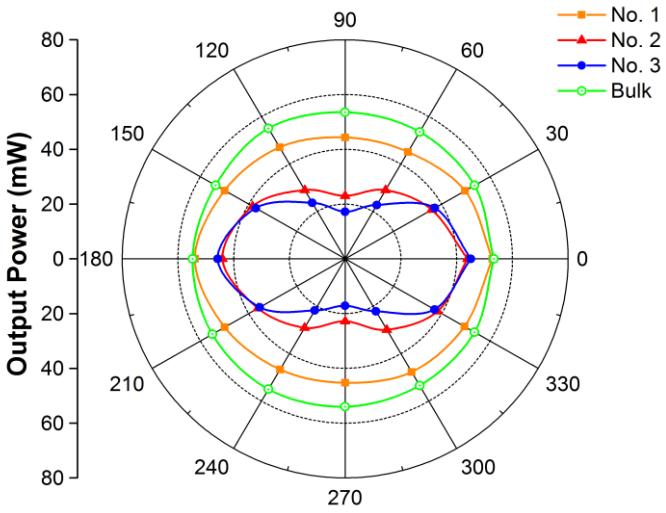

图 4.2.3 不同偏振下的 1064 nm，100 mW 连续激光经 Nd:YVO_4 晶体体材料和波导 Nos. 1-3 传输后的输出功率

图 4.2.3 为 1064 nm 连续激光由固定功率（100 mW）在波导 Nos. 1-3 及体材料中传输后，出射光功率随偏振的变化图。结果表明：

i. 在 Nd:YVO_4 体材料中，激光透过晶体后，出射光无偏振差别，表明了体材料各向同性的吸收性质；

ii. 在光波导 Nos. 1-3 中，各个偏振方向下的出射功率不同，在 TE 偏振下出射功率最高，而在 TM 偏振下出射功率最低，这体现了飞秒激光写入过程中引起的局部各向异性；

iii. 具体分析光波导 Nos. 1-3 在 TE 和 TM 偏振光下出射功率的差别（ΔP），有 ΔP (No. 1) < ΔP (No. 2) < ΔP (No. 3)。我们认为造成该偏振差异的原因是飞秒激光写入痕迹的不对称性，及波导内部的残余应力的共同作用结果；

iv. 光波导 No. 1 在 TE 和 TM 偏振下的差别约为 16%。光波导 No. 2 飞秒激光写入条件与光波导 No. 1 相同，但尺寸较小，平均作用力更大，造成的偏振差异更大，为 47%。光波导 No. 3 由双包层结构组成，受两个飞秒激光写入包层的共同作用，偏振差异最大，为 61%。

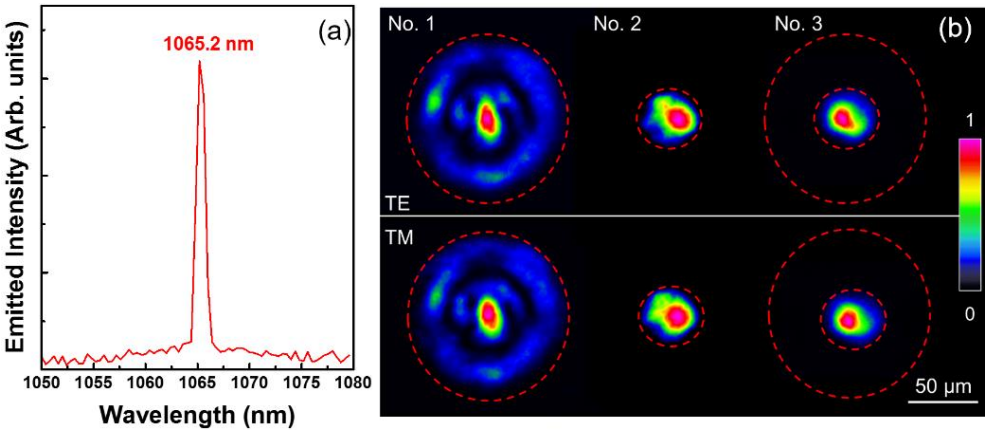

图 4.2.4（a）Nd:YVO_4 晶体光波导调 Q 脉冲激光光谱；（b）波导激光的近场光强分布

图 4.2.4 为飞秒激光写入 Nd:YVO_4 晶体调 Q 脉冲激光的表征。实验发现，不同偏振方向下，波导激光光谱一致，中心波长为 1065.2 nm，对应所掺杂稀土离子 Nd^{3+}离子 $^4F_{3/2}\rightarrow{}^4I_{11/2}$ 能级跃迁，其半高宽为 0.8 nm，如图 4.2.4（a）所示。包层及双包层光波导 Nos. 1-3 均成功实现调 Q 波导激光输出，TE 和 TM 偏振方

向下波导激光模式如图 4.2.4（b）所示。直径较小的包层光波导 No. 2 和双包层波导结构 No. 3 中激光呈低阶模式，No. 3 中激光振荡被限制在内包层中。

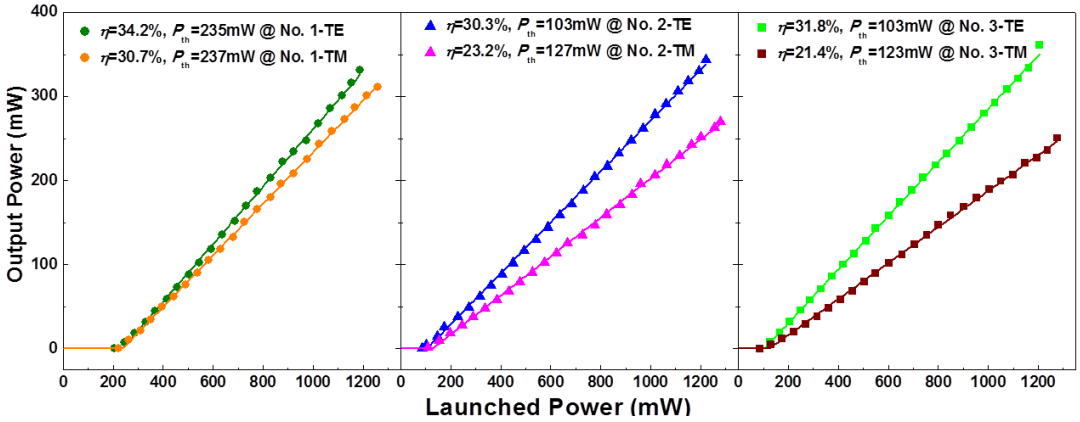

图 4.2.5 Nd:YVO_4 晶体波导 Nos. 1-3 激光平均输出功率随泵浦激光功率的变化

图 4.2.5 为基于端面耦合系统，820 nm 激光泵浦的石墨烯调 Q 波导 Nos. 1-3 脉冲激光平均输出功率随泵浦功率变化。实验数据分析程中，显微镜物镜、滤波片、镀石墨烯膜石英片等光学元件透过率与反射率均被考虑在内，通过对实验数据的线性拟合可以得出不同偏振方向下光波导的出射激光斜效率与激光阈值。实验结果表明：

i. 尺寸小的波导，激光阈值更低。直径为 114 μm 的光波导 No. 1 在 TE 和 TM 偏振方向下的激光阈值 P_{th} 分别为 235 mW 和 237 mW，直径或内直径为 42 μm 的光波导 No. 2 和 No. 3 在 TE 和 TM 偏振方向下的激光阈值分别为 103 mW/127 mW (No. 2) and 103 mW/123 mW (No. 3)。这体现了波导激光相对于体材料激光的优势，即波导内部的高功率密度可大大降低激光阈值；

ii. 光波导 Nos. 1-3 在 TE/TM 偏振方向下激光最高平均输出功率分别为 332 mW/312 mW，344 mW/270 mW，和 361 mW/251 mW，相应激光斜效率分别为 34.2%/30.7%，30.3%/23.2，和 31.8%/21.4%。在 TE 方向，三个波导表现相差较小，约为 8%。而在 TM 偏振方向，波导 No. 1 最优，No. 3 最差，相差约 20%。这与上文中提到的波导的损耗结果有关（图 4.2.3）；

iii. 本实验中测得最大平均激光输出功率为光波导 No. 3 在 1.2 W 的 TE 偏振光泵浦下输出的激光，为 361 mW，阈值为 103 mW。

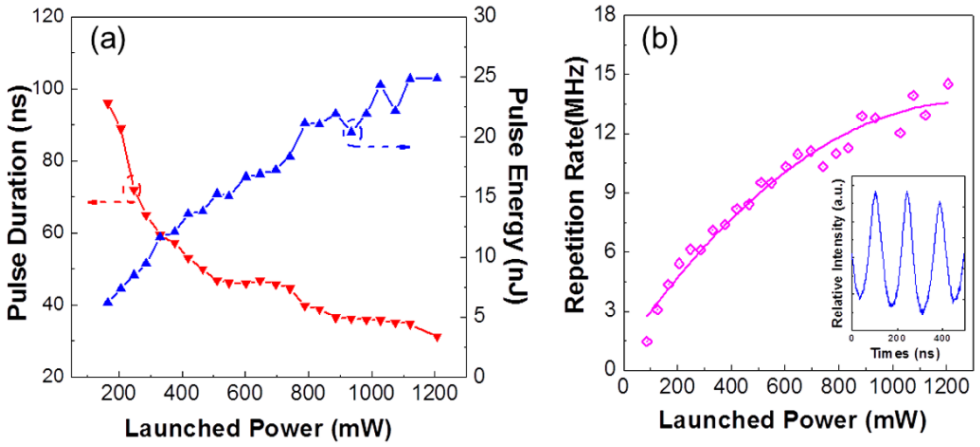

图 4.2.6 Nd:YVO_4 晶体双包层波导 No. 3 脉冲激光的（a）脉冲宽度、单脉冲能量和（b）重复频率泵浦激光功率的变化，插图为脉冲序列

图 4.2.6 对双包层光波导在 TE 偏振下的调 Q 脉冲激光进行了表征。随着泵浦功率的逐渐增加，脉冲宽度由 96 ns 下降至 31 ns，单脉冲能量由 6.2 nJ 上升至 24.9 nJ，重复频率由 1.5 MHz 上升至 14.5 MHz。插图展示了一个典型的调 Q 脉冲序列，相应的激光平均输出功率为 86 mW，单脉冲能量为 12.1 nJ，脉宽为 57 ns，重复频率为 7.1 MHz。

4.2.3 小结

本实验中，我们利用飞秒激光写入技术，在 Nd:YVO_4 晶体中制备了单包层和双包层圆形光波导。基于端面耦合系统，采用 820 nm 连续激光泵浦，石墨烯作为可饱和吸收体，实现波导调 Q 脉冲激光输出。Nd:YVO_4 晶体双包层光波导具备优异的激光特性，最大输出功率为 361 mW，激光阈值为 103 mW，重复频率为 14.5 MHz，单脉冲能量为 24.9 nJ，脉宽为 31 ns。该实验说明双包层结构可应用于制备集成光学器件中的小型化激光器。本节相关工作结果收录于会议论文集中 Advanced Solid State Lasers, OSA Technical Digest (online) (Optical Society of America, 2014), paper AM5A.3.

参考文献

1. 姚建铨，徐德刚. 全固态激光及非线性光学频率变换技术，科学出版社，2007.
2. J. R. O'Connor, Appl. Phys. Lett. **9**, 407 (1966).
3. R. A. Fields, M. Birnbaum, and C. L. Fincher, Appl. Phys. Lett. **51**, 1885 (1987).
4. Y. F. Chen, Opt. Lett. **29**, 2172–2174 (2004).
5. Y. F. Lü, W. B. Cheng, Z. Xiong, J. Lu, L. J. Xu, G. C. Sun, and Z. M. Zhao, Laser Phys. Lett. **7**, 787–789 (2010).
6. A. Di Lieto, P. Minguzzi, A. Pirastu, S. Sanguinetti, and V. Magni, Appl. Phys. B **75**, 463–466 (2002).
7. A. Minassian and M. J. Damzen, Opt. Commun. **230**, 191–195 (2004).
8. F. Chen, X. L. Wang, K. M. Wang, Q. M. Lu, and D.Y. Shen, Appl. Phys. Lett. **80**, 3473 (2002).
9. F. Chen, X. L. Wang, K. M. Wang, Q. M. Lu, and D. Y. Shen, Opt. Lett. **27**, 1111–1113 (2002).
10. F. Chen, L. Wang, Y. Jiang, X. L. Wang, K. M. Wang, G. Fu, Q. M. Lu, C. E. Ruter, and D. Kip, Appl. Phys. Lett. **88**, 071123 (2006).
11. W. F. Silva, C. Jacinto, A. Benayas, J. R. Vazquez de Aldana, G. A. Torchia, F. Chen, Y. Tan, and D. Jaque, Opt. Lett. **35**, 916–918 (2010).
12. Y. Tan, F. Chen, J. R. Vazquez de Aldana, G. A. Torchia, A. Benayas, and D. Jaque, Appl. Phys. Lett. **97**, 031119 (2010).
13. Y. C. Jia, F. Chen, and J. R. Vazquez de Aldana, Opt. Express **20**, 16801–16806 (2012).
14. J. H. Warner, F. Schäffel, A. Bachmatiuk, and M. H. Rümmeli, Graphene, Fundamentals and emergent applications, (Elsevier, 2012).
15. A. K. Geim and K. S. Novoselov, Nat. Mater. **6**, 183–191 (2007).
16. C. Lee, X. D. Wei, J. W. Kysar, and J. Hone, Science **321**, 385–388 (2008).
17. A. A. Balandin, S. Ghosh, W. Z. Bao, I. Calizo, D. Teweldebrhan, F. Miao and C. N. Lau, Nano Lett. **8**, 902–907 (2008).

18. 陈永胜，黄毅. 石墨烯：新型二维碳纳米材料，科学出版社，2013.
19. Q. Bao, H. Zhang, Y. Wang, Z. Ni, Y. Yan, Z. X. Shen, K. P. Loh, D. Y. Tang, Adv. Funct. Mater. **19**, 3077–3083 (2009).
20. H. Zhang, D. Y. Tang, R. J. Knize, L. M. Zhao, Q. L. Bao, and K. P. Loh, Appl. Phys. Lett. **96**, 111112 (2010).
21. D. Popa, Z. Sun, T. Hasan, F. Torrisi, F. Wang, and A. C. Ferrari, Appl. Phys. Lett. **98**, 073106 (2011).
22. Y. Tan, C. Cheng, S. Akhmadaliev, S. Q. Zhou and F. Chen, Opt. Express **22**, 9101–9106 (2014).

第五章 荧光强度比率分析法测量光波导的温度

温度是影响波导性能的一个重要因素，除波导所处外部环境，波导在运行过程中本身的热量累计也是不可忽略的重要方面。大量的研究表明[1-4]，在高功率激光振荡过程中，泵浦引起的温度升高限制了激光器的性能；温度变化会引起折射率的变化，使得波导的结构和导波性能受到影响；由于热量累计引起的温度梯度产生应力场，会对波导的性能及寿命造成损害；非线性晶体光波导频率转换的产生依赖于相位匹配，温度的变化会引起转换效率的降低。因此对于波导的温度表征及调控具有重要的研究意义。传统的热成像方法，如红外热成像[5]（Infrared Thermal Imaging）、扫描热显微镜[6]（Scanning Thermal Microscopy，SThM）、热透镜法[7]（Thermal Lens based Interference Methods），因为种种限制，如接触式测量、表面型测量、分辨率低等，无法满足对波导结构的探测。

荧光强度比率分析法[8]，指利用两个不同的激发态到低能级的荧光强度比率与温度的关系分析温度的方法。共聚焦荧光热成像法[9]（Confocal Luminescence Thermal Imaging，CLTI），即利用共聚焦荧光显微镜测量三维高分辨率荧光光谱，结合无接触、对样品无损耗的荧光强度比率分析法，得到高分辨率的三维热成像。该方法已被广泛应用于纳米颗粒，荧光分子等进行温度表征[10,11]，但尚未成功应用于波导温度的表征。本章利用共聚焦荧光热成像法，对波导的温度进行热成像。

钇铝石榴石（$Y_3Al_5O_{12}$，YAG）晶体，属于立方晶系，oh-m3m 点群，光学性质各向同性。利用稀土离子掺杂使钕离子（Nd^{3+}）替代晶体点阵中的部分钇离子（Y^{3+}），可获得掺钕钇铝石榴石晶体（Nd:YAG）[12]。Nd:YAG 是综合性能最高、最常用的固体激光材料之一，具有高增益、低阈值、高效率、高机械强度等优点，广泛应用于医疗、军事和科研等领域[13-15]。科学家们先后利用离子注入/辐照、聚焦质子束直写、飞秒激光加工等方法在 Nd:YAG 晶体中制备了光波导，并实现连续或脉冲激光振荡[16-20]。与体材料激光相比，Nd:YAG 波导激光具有阈值低、效率高等优点，可应用于高功率集成激光器件。

磷酸盐玻璃以 P_2O_5 为主要成分，以$(PO_4)_3$-四面体相互连接成网络，具有低色散的特点。磷酸盐玻璃可以掺入高浓度的稀土离子而不产生淬灭，掺杂较均匀，且上转换损耗较低、增益高。因此，磷酸盐玻璃是稀土离子掺杂放大器和激光器

的理想介质，其中铒镱共掺磷酸盐玻璃（Er:Yb:phosphate glass）常用于放大器及红外激光器[21-24]。铒（Er^{3+}）离子能级丰富，但吸收截面较小，Er^{3+}离子亚稳态能级的离子成对现象易引起浓度淬灭效应。镱（Yb^{3+}）离子在 980 nm 泵浦下的吸收截面大、吸收带宽（800 nm-1100 nm），Yb^{3+}离子的 $^2F_{5/2}$ 能级和 Er^{3+}离子的 $^4I_{11/2}$ 能级重叠部分大，铒镱共掺使得 Er^{3+}离子被 Yb^{3+}离子包围从而降低 Er^{3+}离子的浓度淬灭效应。因此，利用 Yb^{3+}离子作为敏化剂，可以大幅提高对泵浦光的吸收效率。大量研究表明，铒镱共掺磷酸盐玻璃光波导可用于制备高增益、高效率的激光器及放大器[25-27]。

激光振荡和放大过程中，温度变化对其性能有不良的影响，而具有高功率密度的波导激光器和放大器的热效应更为显著。本章利用共聚焦荧光热成像方法对 Nd:YAG 晶体及铒镱共掺磷酸盐玻璃中通道光波导的温度变化进行研究。通过测量波导的微荧光图谱，研究泵浦导致的波导温度变化，获取波导三维热成像。并提出利用时间调制泵浦光的方法降低泵浦引起的温度变化。

5.1 Nd:YAG 晶体光波导的温度表征

本节工作主要采用飞秒激光加工在 Nd:YAG 晶体制备通道光波导，并利用荧光强度比率分析法表征其在导波过程中的温度变化。

5.1.1 实验过程

本实验中所使用 Nd:YAG 晶体中 Nd^{3+}离子掺杂浓度为 1 at.%，晶体尺寸为 $10 \times 10 \times 2\ mm^3$，其六个平面均经光学抛光。具体实验过程如下：

i．波导的制备

首先，采用飞秒激光对样品进行写入加工。此过程是使用西班牙萨拉曼卡大学的钛宝石飞秒激光系统完成，基本设置和前面章节相同，工作中心波长为 800 nm，脉宽为 120 fs，重复频率为 1 kHz，扫描速度为 500 μm/s，脉冲功率为 0.21 nJ，相邻写入痕迹之间间隔为 3 μm，共写入 7 条痕迹，组成一个半圆形结构。波导位于由 7 条折射率降低的写入痕迹和样品空气表面所包裹的内部区域。图 5.1.1（a）展示了波导的端面显微镜图。

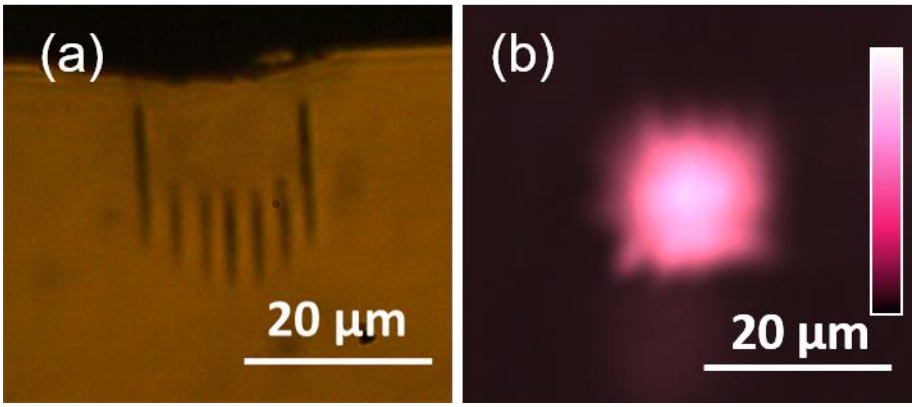

图 5.1.1（a）波导端面显微镜图，（b）800 nm 下的波导近场模式分布

ii．波导特性测试

基于端面耦合系统，利用二极管激光器，通过光纤将 800 nm 的激光耦合到波导的端面，出射激光利用显微镜物镜汇聚后用 CCD、功率计等仪器进行数据采集分析。图 5.1.1（b）展示了波导在 800 nm 下的近场模式分布。

iii. 高功率紫外固化 LED 系统

图 5.1.2 高功率紫外固化 LED 系统

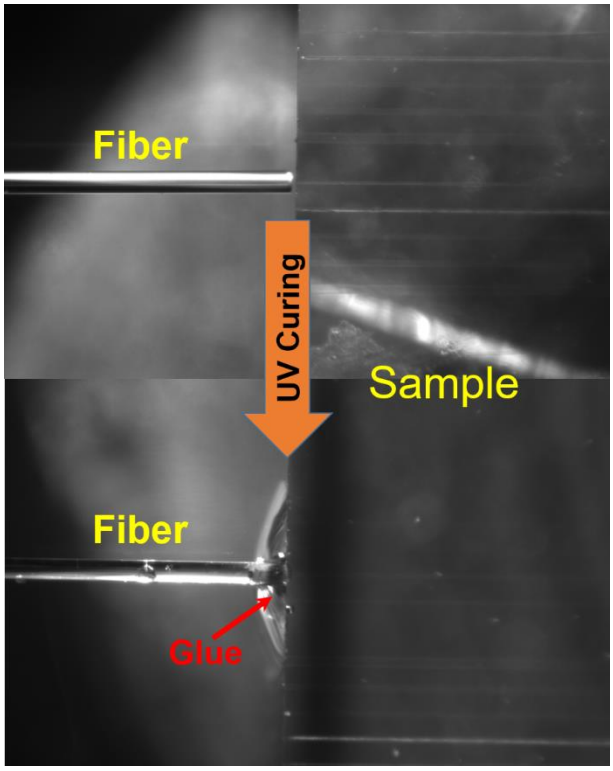

图 5.1.3 紫外固化前后端面耦合的俯视显微镜图，样品中直线为飞秒激光写入痕迹

为将入射光纤与波导集成在一个系统内，成为一个可移动的整体器件，我们采用高功率紫外固化 LED 系统（CS2010，Thorlabs. Inc.），如图 5.1.2 所示。首先，将样品固定于载玻片上，放置于三维样品调节平台上，使用光纤进行端面耦

合，出射端使用 CCD 采集波导的近场模式分布，样品平台正上方垂直放置光学显微镜连接 CCD 观测光纤和波导的耦合；其次，将透明光学胶（Norland NOA61）滴到光纤和样品接触处，使用高功率紫外光照射，光学胶在几秒钟内开始凝结，在几分钟内完全固化为强韧的粘结，图 5.1.3 为俯视显微镜图，光学胶凝固后无色透明；最后，使用光学胶将入射光纤探出的部分约 1 cm 处固定在载玻片上，使得载玻片、样品和光纤组成一个集成元件，可移动、安插在光路中。

iv. 泵浦+探测系统

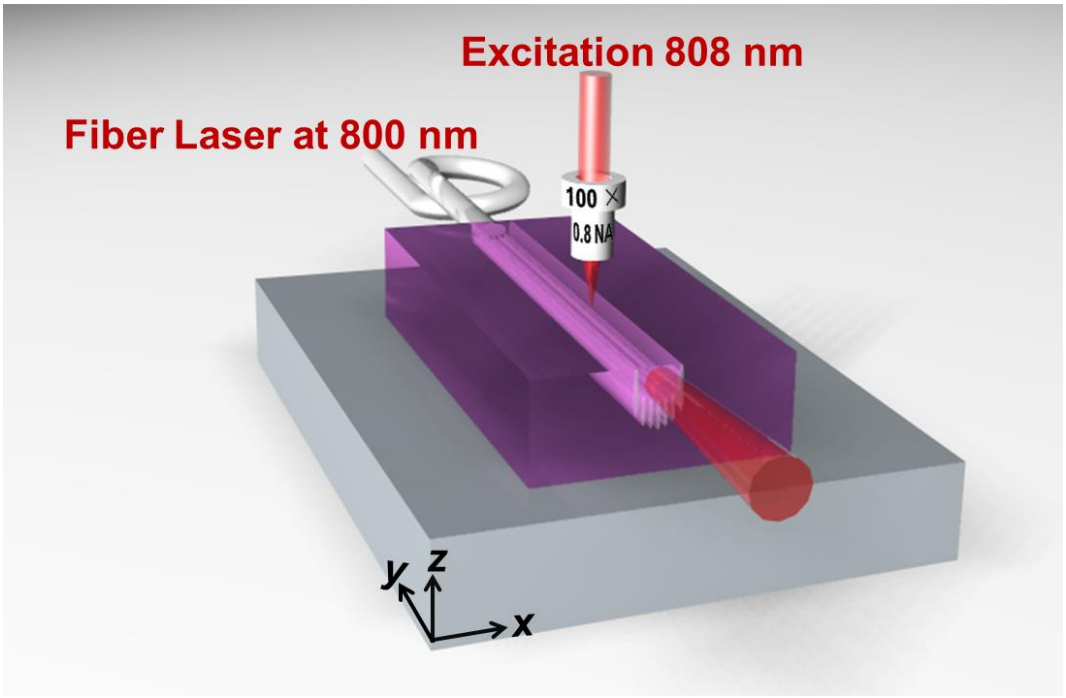

图 5.1.4“泵浦+探测”荧光测温系统的装置示意图

基于端面耦合和共聚焦荧光显微镜技术，我们利用“泵浦+探测”系统测量波导在 800 nm 泵浦下的温度变化，如图 5.1.4 所示，将上节中制备的光纤—波导元件放置在共聚焦荧光显微镜的 *xyz* 三维电动平台上，808 nm 的探测光由上方经长工作距离物镜（100×, N.A. = 0.80）聚焦后垂直射入样品表面，所产生的荧光经同一个物镜汇聚收集后由光谱仪（Horiba Jobin Yvon, iHR320）进行采集分析。通过控制放置样品的三维电动平台进行移动，可以得到三维荧光光谱图，对波导不同位置、长度、深度的温度变化进行表征。

5.1.2 结果与讨论

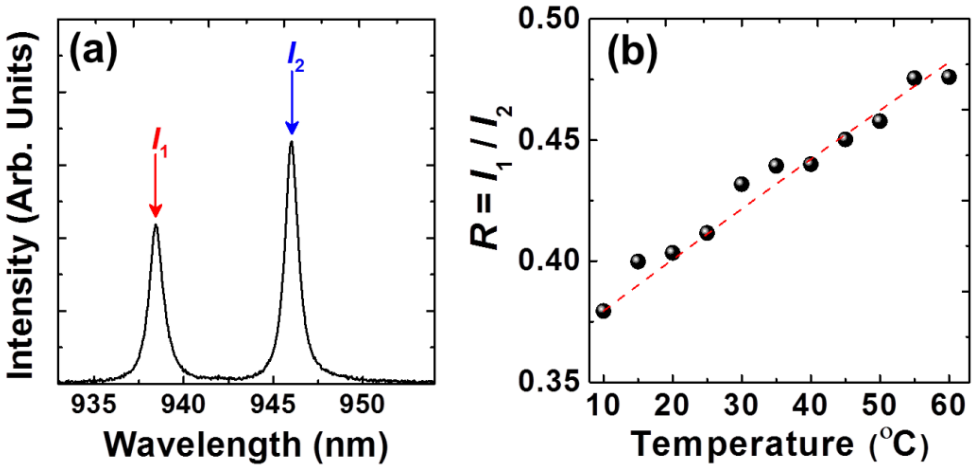

图 5.1.5（a）Nd:YAG 荧光发射谱，I_1 和 I_2 为荧光比率所采用的两个峰；（b）荧光强度比值 R 随温度的变化，实线为线性拟合结果

Nd:YAG 晶体中掺杂的稀土离子 Nd^{3+}离子在 $^4F_{3/2}\rightarrow{}^4I_{9/2}$ 能级跃迁，所产生的荧光光谱图如图 5.1.5 所示。有关 Nd:YAG[28]的微荧光性质和导波性质的研究指出，I_1（938 nm）和 I_2（945 nm）两个发射线是理想的温度探针，可用来探测温度的微小变化；对 Nd:YAG 纳米颗粒的研究结果表明[29]，这两个发射线的荧光强度比率可以用以温度表征。图 5.1.5（b）描述了样品在不同温度下的荧光强度比值 $R = I_1/I_2$，我们采用其线性拟合结果作为校准曲线，计算可得比荧光比率的灵敏度约为 0.5% $°C^{-1}$。此系统中使用的探测光功率低于 20 mW，所引起的温度变化可忽略。

图 5.1.6 为 Nd^{3+}荧光谱中 945 nm 荧光峰的表征，选取距离样品入射端面 100 μm 处，垂直于波导传输方向的截面进行二维荧光光谱测量，泵浦激光功率为 100 mW。结果表明：由于飞秒激光写入过程引起的应力场变化及晶格损伤，使得写入痕迹及其附近区域折射率等性质发生变化，进而影响了该区域的荧光性质，引起谱线红移、谱线展宽，图中清晰展示了飞秒激光写入痕迹的位置；对比泵浦激光开关时荧光强度比率 R，可得出在飞秒激光写入痕迹与空气所包围的波导区域，R 增大，即温度升高。

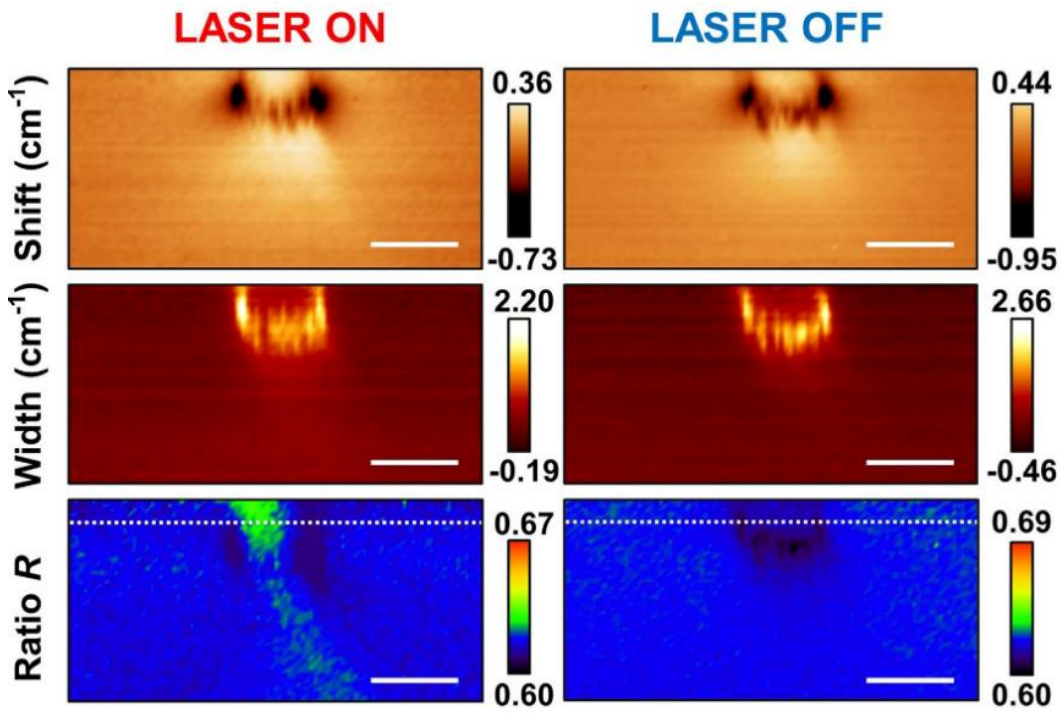

图 5.1.6 泵浦激光开（左列）或关（右列）时，Nd^{3+}荧光谱中 945 nm 荧光峰的频移和展宽的空间分布，及荧光强度比值 *R* 的空间分布。标尺均为 20 μm

进一步地，我们提取图 5.1.6 中距离波导表面 5 μm 深度的虚线位置的数据，绘制了荧光强度比值 *R* 曲线，见图 5.1.7（a）。当无泵浦光时，飞秒写入痕迹处 *R* 大幅下降，而在波导区域 *R* 稍微降低，基本与衬底区域一致；当打开泵浦光时，*R* 发生了明显的变化，衬底区域 *R* 少许增大，波导内部区域大幅升高，这可归因于波导中 800 nm 的泵浦光引起的温度变化。利用 Laser Off 时曲线为背景曲线，根据图 5.1.5（b）的校准曲线可以计算出泵浦光在波导中传输时的温度变化，如图 5.1.7（b）所示。由于样品对于 800 nm 激光的吸收，在波导附近区域温度轻微升高，主要的温度变化仍被限制在波导的内部。同样地，对于图 5.1.6 中的二维荧光强度比率图进行分析可得到图 5.1.7（c），飞秒激光写入痕迹形成一个准连续的热阻抗将热量限制在波导内部，使得温度升高 10℃左右。文献[30]中指出超快激光写入透明材料引起的损伤具有降低的热导率，本文结果与文献中结论一致。图 5.1.6 和 5.1.7 的结果表明，在本工作采用 100 mW，800 nm 激光泵浦下所引起的轻微温度变化对于波导及其附近区域的应力场和晶格损伤等没有产生影响。若增大泵浦功率，引起温度升高，则应力场的变化及自退火效应不可忽略。

由图 5.1.7（b）我们可以推算得波导边缘的热梯度约为 0.5℃/μm，比文献中[31]激光陶瓷 Nd:YAG 的热梯度高一个数量级。

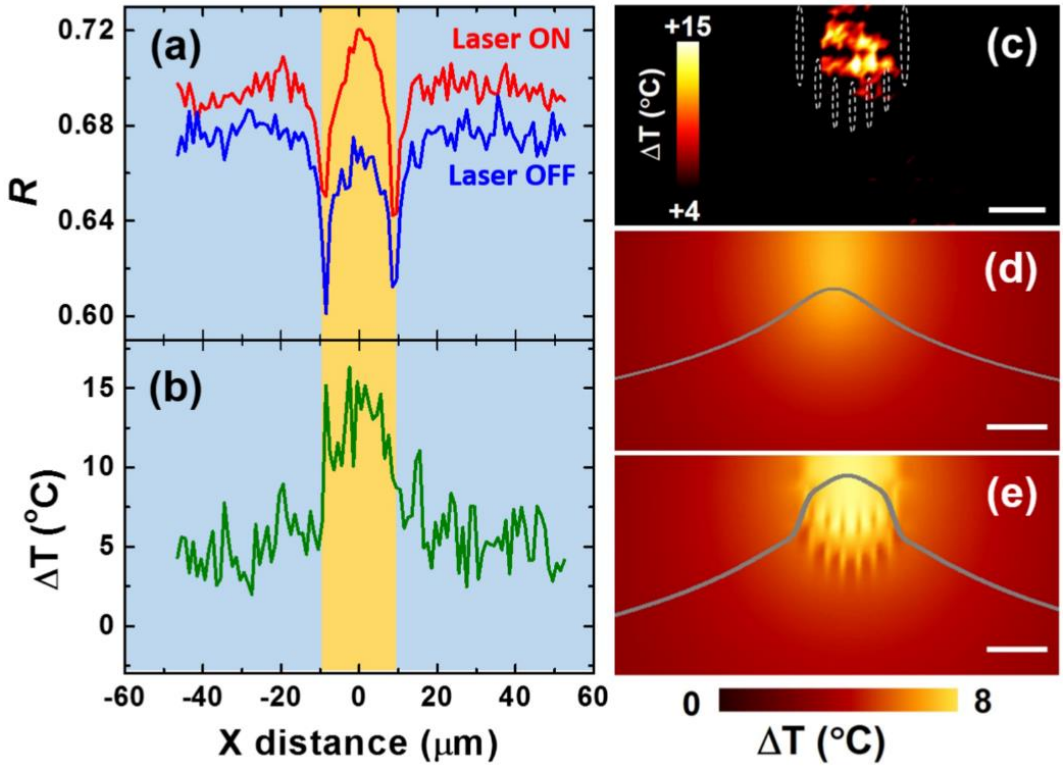

图 5.1.7 泵浦激光开或关时，图 5.1.6 中虚线距离波导表面 5 μm 深度处的 a）荧光强度比值 *R* 及（b）温度变化。黄色区域标示波导所处位置；（c）Nd:YAG 波导截面热成像，虚线位置表示了飞秒激光写入痕迹的位置;（d）采用均匀热导率或（e）在写入痕迹处热导率降低的两种模型下，模拟的波导温度变化，选取距离表面 5 μm 深度处数据绘制为灰色温度曲线；（c）-（e）中标尺为 10 μm

为研究飞秒激光写入痕迹处热导率的降低对于泵浦激光引起波导温度变化的空间分布的影响，我们利用有限差分法对热扩散方程进行了模拟计算。计算所涉及的热学性质和光谱性质与文献[32]中相同。图 5.1.7（d）假设热导率没有变化，达到热平衡时的温度变化分布图。由于热扩散效应，波导外部温度也有升高，故应该假设飞秒激光写入痕迹处的热导率降低。经过模拟参数的调整优化，热导率降低 80%时模拟结果和测量结果达到一致，温度变化分布图如图 5.1.7（e）所示。文献[28,33]中报道的超快激光写入 Nd:YAG 晶体引起的损伤约为 50%～70%，与本文结果相近。通过对比理论计算和实验数据，可以得出：波导的周围区域温度小

幅上升，主要温度变化位于波导内部。虽然模拟结果定性地支持了实验数据，但是在定量分析上两者仍然存在差异——实验结果温度升高最大为 15℃，而模拟结果为 8℃，该差异可部分归因于波导中 Nd^{3+}离子的热载荷变化，与晶格缺陷有关的热源等。但理论计算和实验数据同时证明，泵浦光在 Nd:YAG 晶体光波导中引起几度的温度升高。

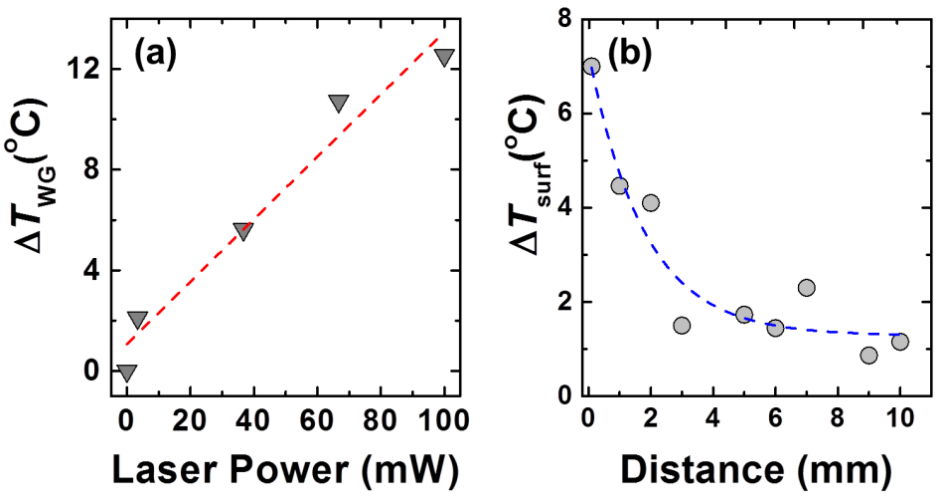

图 5.1.8（a）波导内部的最大温度变化值 ΔT_{WG} 随泵浦光功率的变化；（b）波导表面温度变化 ΔT_{surf} 沿波导传播方向的变化

图 5.1.8（a）展示了波导内部的最大温度变化 ΔT_{WG} 随泵浦光功率升高而呈线性增长。图 5.1.8（b）为波导表面温度变化 ΔT_{surf} 沿波导传播方向变化的曲线，起点为泵浦光入射端面。随着传输距离的延长，波导温度变化呈指数下降。

为进一步地证明波导的温度变化，我们采用热敏上转换纳米颗粒 Er:Yb:LaF_3 对波导进行温度表征，该材料的已被报道，适用于高灵敏度荧光比率热感[9]。如图 5.1.9（a）所示，将粉末状的纳米颗粒放置在样品表面，探测光波长为 980 nm，通过双光子吸收，收集 Er^{3+}离子的 500-550 nm 波段的荧光，泵浦光开和关时的归一化荧光光谱如图 5.1.9（b）所示。根据两个发射峰 525 nm 和 545 nm 的强度比率我们可以得出，当打开泵浦光时，545 nm 发射线所占的比例升高，这已被证明是由 Er:Yb:LaF_3 纳米颗粒温度的升高引起的。根据文献[21]中给出的校准曲线，我们计算得出纳米颗粒的温度变化，即波导表面温度变化 ΔT_{surf}，随泵浦光功率的变化，如图 5.1.9（c）所示。泵浦功率为 100 mW 时，波导表面温度变化

ΔT_{surf}为 7℃，与 5.1.8（c）中温度相一致。

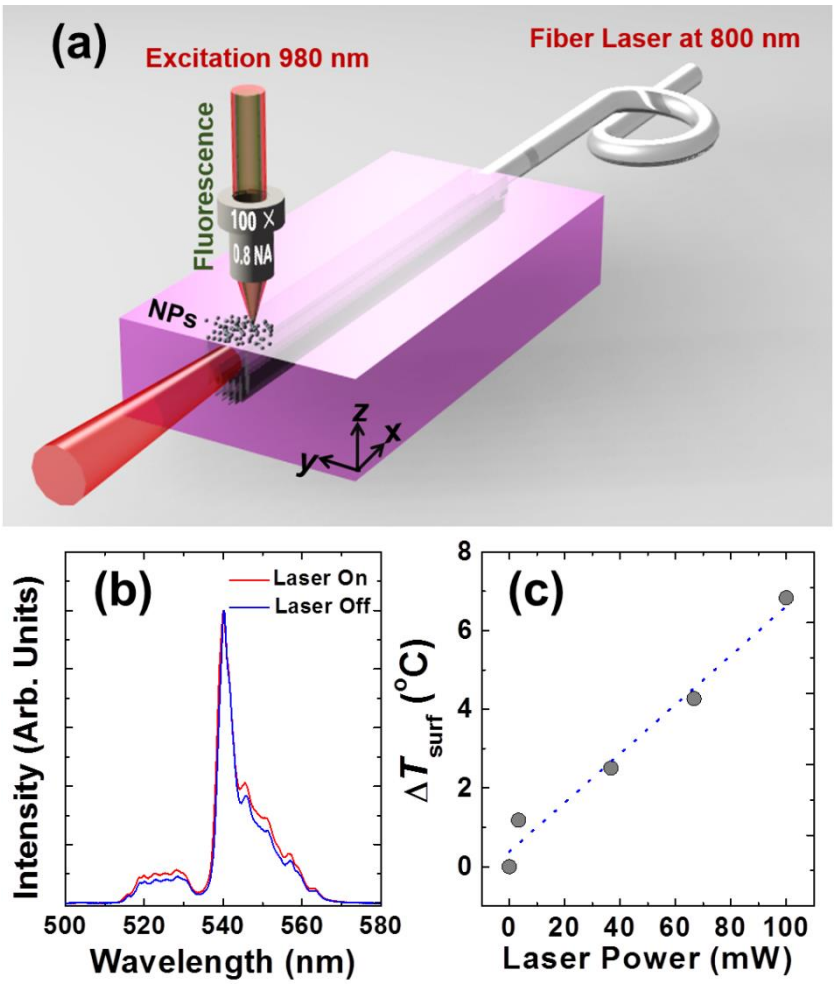

图 5.1.9（a）上转换纳米颗粒表征波导温度的装置示意图;（b）泵浦光开和关时归一化的上转换发射光谱；（c）波导表面温度变化 ΔT_{surf}随泵浦光功率的变化

5.1.3 小结

本节工作主要是利用荧光强度比率分析法，结合高分辨率共聚焦荧光显微技术测量 Nd:YAG 波导的热成像。在 100 mW 的 800 nm 激光泵浦下，波导内部温度升高约 10℃左右。飞秒激光写入痕迹处折射率降低，使其内部包裹区域形成波导，同时其热导率大幅降低，形成热阻抗将热量限制在波导内部。本工作表明“泵浦+探测”系统可用于探测和监控波导导波或激光过程中的温度变化。本节相关工作结果发表于 *Optics Letters* **41**, 2061–2064 (2016)。

5.2 铒镱共掺磷酸盐玻璃光波导的三维热成像

基于“泵浦+探测”系统，对于铒镱共掺磷酸盐玻璃光波导进行三维高分辨率热成像，并对泵浦光进行调控以降低热效应。

5.2.1 实验过程

i．波导的制备和导波特性测量

实验选用六面光学抛光的铒镱共掺磷酸盐玻璃，掺杂浓度为 1.5 wt.% Er_2O_3 和 4.5 wt.% Yb_2O_3，抛光后晶体尺寸为 17 × 9 × 2 mm^3。使用西班牙萨拉曼卡大学的钛宝石飞秒激光系统在铒镱共掺磷酸盐玻璃中写入光波导，除脉冲功率为 0.36 nJ 外，飞秒激光的设置与 5.1 节相同。波导由 7 条写入痕迹和样品空气表面所包裹组成，直径约 17 μm。图 5.2.1（a）展示了波导的端面显微镜图。波导内部折射率与衬底折射率相同为 n_g，飞秒激光写入痕迹处折射率下降 Δn，空气折射率 $n_a = 1$，图 5.2.1（a）中虚线描述了距表面 5 μm 深度处的折射率分布。利用光纤端面耦合将 800 nm 激光耦合进波导端面，出射近场模式分布如图 5.2.1（b）所示，光被飞秒激光写入痕迹所形成的壁垒限制在波导内部传输。

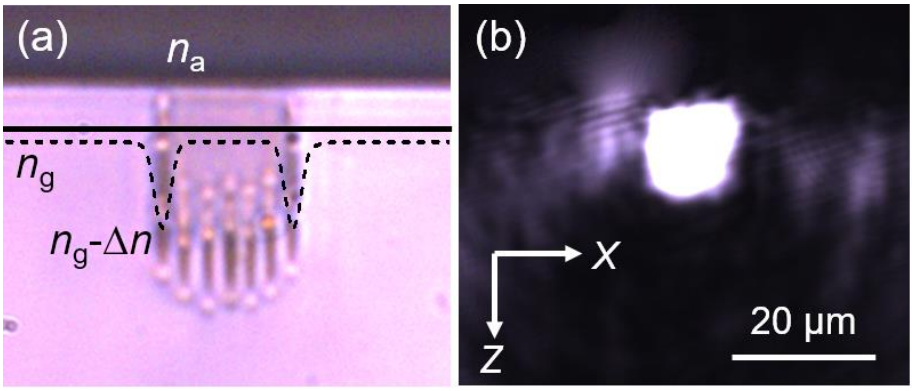

图 5.2.1（a）波导端面显微镜图；（b）800 nm 下的波导近场模式分布

ii．波导热成像

采用 5.1 节所介绍的“泵浦+探测”端面耦合系统，利用二极管激光器，通过光纤将 980 nm 的激光耦合到波导的端面，另一 980 nm 的探测光经显微物镜

（100×, N.A.=0.80）汇聚后垂直聚焦于样品表面，根据激光和各光学元件的参数可得探测光的三维分辨率约为 2.5 μm^3。

iii．双光子吸收

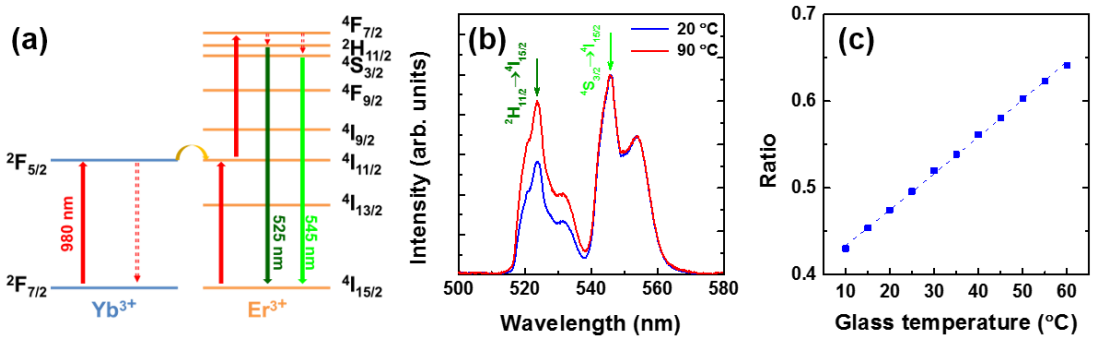

图 5.2.2（a）980 nm 泵浦下的 Er^{3+}，Yb^{3+}离子级跃迁图；(b)不同温度下的荧光发射光谱；（c）荧光强度比率随玻璃温度的变化，虚线为数据的线性拟合曲线

铒镱共掺磷酸盐玻璃中 Yb^{3+}作为敏化剂，大大提升了对 980 nm 泵浦光的吸收效率。如图 5.2.2（a）所示，本文所利用的双关子吸收产生绿光荧光所涉及到的能量吸收、跃迁和转移过主要有：

i. $^2F_{7/2}\rightarrow{}^2F_{5/2}$ Yb^{3+}受激吸收跃迁

ii. $^2F_{5/2}\rightarrow{}^2F_{7/2}$ Yb^{3+}辐射跃迁

iii. $^4I_{15/2}\rightarrow{}^4I_{11/2}$ Er^{3+}受激吸收跃迁

iv. $^2F_{5/2}(Yb^{3+})+{}^4I_{15/2}(Er^{3+})\rightarrow{}^2F_{7/2}(Yb^{3+})+{}^4I_{11/2}(Er^{3+})$ 能量转移

v. $^2F_{5/2}(Yb^{3+})+{}^4I_{11/2}(Er^{3+})\rightarrow{}^2F_{7/2}(Er^{3+})+{}^4I_{15/2}(Er^{3+})$ 能量转移

vi. $^4H_{11/2}\rightarrow{}^4I_{15/2}$ Er^{3+}上转换发光（中心波长 525 nm）

vii. $^4S_{3/2}\rightarrow{}^4I_{15/2}$ Er^{3+}上转换发光（中心波长 545 nm）

iii．荧光强度比率 *R* 的测量

图 5.2.2（b）展示了铒镱共掺磷酸盐玻璃在 500 nm-580 nm 波段的荧光发射光谱，我们采用两个发射线 525 nm 和 545 nm 的荧光强度比率 $R=\frac{I_{525}}{I_{545}}$ 来测量波导中的温度变化。由不同温度下的荧光发射谱线可以看出，525 nm 在温度升高时所占的比率明显变大。将样品放置在温控平台上，温度从 10℃逐步升高至 60℃，

每 5℃测量一次荧光发射光谱，所得荧光强度比率随玻璃温度的变化如图 5.2.2（c）所示，可近似使用线性拟合获得校准曲线。荧光强度比率灵敏度 S 由公式 5.2.1[35]计算可得为~ 0.9% $℃^{-1}$。

$$S = \frac{1}{R}\frac{dR}{dT} \tag{5.2.1}$$

5.2.2 结果与讨论

实验操作在室温（20℃）下进行，980 nm 探测光功率固定为 30 mW，与 5.1 节中 Nd:YAG 晶体所不同的是，由于磷酸盐玻璃导热系数较小（0.7 W/m·K @ 25℃），探测光引起样品温度升高不可忽略。根据上文所述荧光强度比率灵敏度 S 计算可得，在 30 mW 的 980 nm 探测光照射下，共聚焦焦点处的样品温度升高 40℃，在本文的测量过程中，这个温度被视为背景。在分析泵浦光所引起的荧光光谱变化时，我们分别测量泵浦光关闭（Laser Off）和打开（Laser On）时的数据，利用后者去除前者的影响，得到泵浦光所引起的温度变化 ΔT。

有关 Er^{3+}荧光温度计的研究[36]表明，激发光的功率密度对热灵敏度的测量具有重要的影响。通过对本节所使用的“泵浦+探测”系统中的功率密度的分析，热灵敏度为常数。其中，探测光的功率密度约为 2×10^6 W/cm^3，泵浦光的功率密度根据功率的大小约在 2×10^4 W/cm^3 — 4×10^4 W/cm^3 范围内，比前者小两个数量级。因此，在探测光功率密度远远大于泵浦光功率密度的情况下，不同功率的泵浦光所引起的热灵敏度差异可以忽略。而 Er^{3+}离子较高的荧光强度比率灵敏度有利于获得高分辨率的三维荧光热成像。

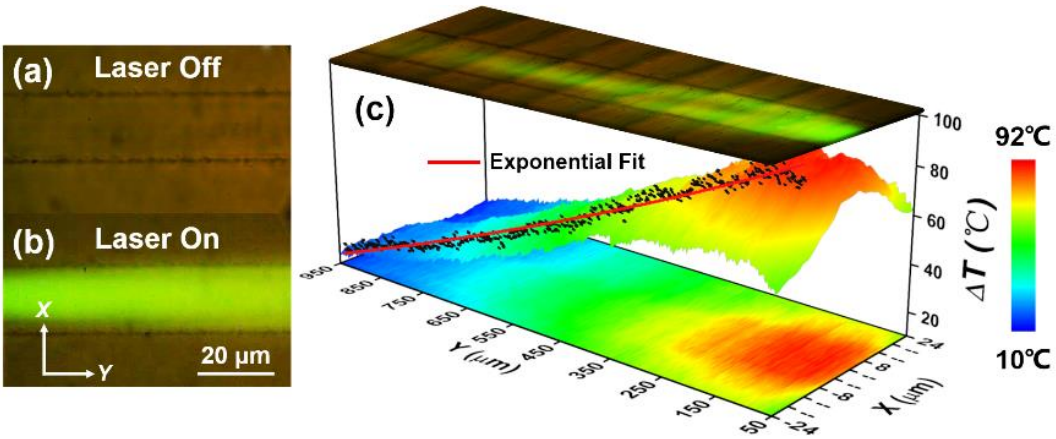

图 5.2.3 泵浦光开（a）和关（b）下的波导显微镜图；（c）沿波导传播方向 Y 的荧光热成像，

$Y = 0$ 处为泵浦光入射端面，上图为显微镜图，提取 $X = 0$ 处的数据利用指数函数进行拟合

XY 平面上铒镱共掺磷酸盐玻璃光波导的二维荧光热成像图如图 5.2.3 所示。图 5.2.3（a）和（b）为泵浦激光开和关时的波导显微镜图，两条直线即为波导最外侧的两条飞秒激光写入痕迹，其内部为波导区域，当泵浦光打开时，可看到上转换产生的绿色荧光被限制在波导内部传输。当 60 mW, 980 nm 的泵浦光入射时，在距离样品表面 5 μm 深度处测得二维荧光光谱图，计算得到温度变化分布图，见图 5.2.3（c），结果表明:

i. 沿波导传输方向 *Y*，波导内部温度升高值逐渐降低，主要集中在距入射端面 1 mm 以内，这个现象可归因于 Yb^{3+}离子对于 980 nm 泵浦光的强烈吸收：本节所采用的铒镱共掺磷酸盐玻璃在 980 nm 处的吸收系数 α_{abs} 为 8.2 cm^{-1}，截止传输长度为 L_{abs} = 1.2 mm (传输 L_{abs} 距离后，入射光的功率降为原来的 1/e)。图 5.2.3（c）中显微镜插图也可看出随着传输距离接近 1 mm，绿色荧光越弱。此外，数据拟合也显示波导温度变化沿波导传输方向 *Y* 成指数衰减。

ii. 在 60 mW, 980 nm 的泵浦光入射下，波导内部温度升高最大值达到 92 ℃，远远高于 5.1 节中 Nd:YAG 波导的 10℃，泵浦光导致的波导温度不可忽略，在设计和使用此类波导时应该考虑温度变化对其性能的影响。另外，一些文献中也报道过这类材料中的泵浦引起的温度升高，如铒镱共掺磷酸盐玻璃激光芯片[22]（74℃ @ 975 nm, 75 mW），二极管端面泵浦 Yb：YAG 晶体[37]（49℃ @ 968 nm, 13.5 W），Yb^{3+}:$CaGdAlO_4$ 晶体[38]（57℃ @ 980 nm, 0.6 W），铒镱共掺光纤[39]（38℃ @ 980nm, 68 mW）。本节泵浦所产生的温度变化远高于文献记载，是因为光波导结构将泵浦光限制在很小的区域（17 μm）内传输，泵浦功率密度较高。

iii. 由于热扩散效应，波导周围区域也有稍许的温度升高。

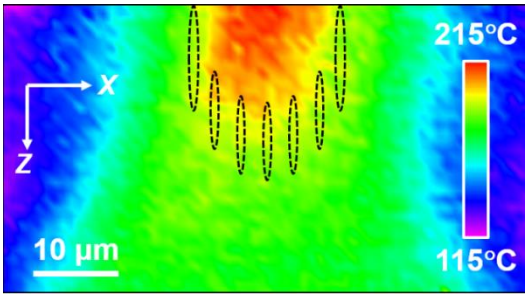

图 5.2.4 波导截面 *XZ* 平面的二维热成像，黑色虚线标示了飞秒激光写入痕迹的位置

图 5.2.4 为波导截面 *XZ* 平面上的温度变化，测量位置距离泵浦光入射端面为 50 μm，泵浦光功率为 120 mW。结果表明，波导内部温度大幅升高最大至 215℃，飞秒激光写入痕迹有效的限制了热量的传输，波导周围区域温度升高较小。飞秒激光写入痕迹的“热阻”效果也体现在波导周围区域温度升高的各向异性：沿 *Z* 方向，即平行于飞秒激光写入痕迹的方向，温度梯度约为~1.5℃/μm；而沿 *X* 方向，温度梯度为~1.9℃/μm，即飞秒激光写入痕迹表现为各向异性的“热壁垒”作用，这与 Belloudard 等[30]所报道的超快激光写入痕迹处热导率下降一致。

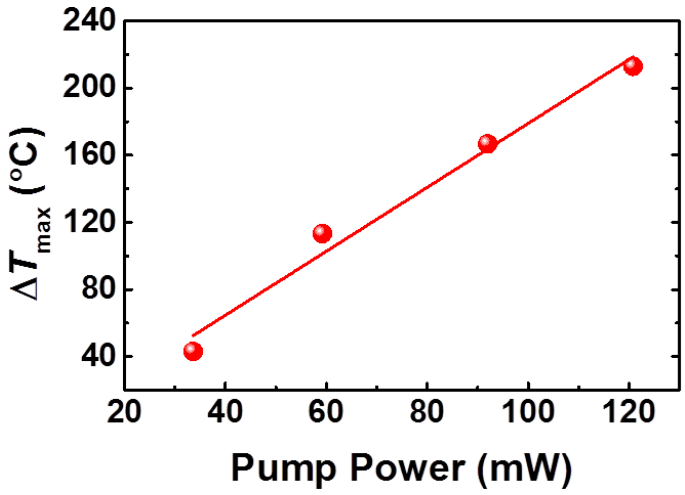

图 5.2.5 波导内最大温度变化值 ΔT_{max} 随泵浦功率的变化

图 5.2.5 为波导内最大温度变化值 ΔT_{max} 随泵浦功率的变化，随着泵浦功率的升高，ΔT_{max} 逐渐升高，在本文的实验条件下，成线性增长关系。这表明，即使泵浦光引起的温度升高超过 200℃（对应样品实际温度为 260℃），仍没有破坏波导的导波性能，否则该曲线应该呈现非线性变化。

以上结果表明，980 nm 激光泵浦下铒镱共掺磷酸盐光波导产生的温度升高不可忽略，影响了波导的性质。为了降低此热效应，我们对泵浦激光进行时间调制，如图 5.2.6 所示，脉冲间隔大于特征热弛豫时间 $\tau_{thermals}$ 时，相邻两个脉冲之间的热累计效应最小[22,39]，文献[40,41]中使用该方法优化激光芯片的激光性。我们将 980 nm 泵浦激光进行时间调制，形成为脉宽为 2 ms，峰值功率为 60 mW，脉冲间隔从 0.1 ms 到 10 ms 可调的脉冲激光。如图 5.2.6 所示，脉冲间隔远远大于

特征热弛时间 $\tau_{thermals}$ 时，热扩散作用在下一个脉冲到来之前将热量完全热耗散，无法产生热量累积；而脉冲间隔短于 $\tau_{thermals}$ 时，产生热量累计。对以上理论，我们通过实验进行了验证，如图 5.2.6（c）所示，泵浦激光导致波导温度变化值 ΔT 随脉冲间隔的增大单调递减。数据拟合显示，该递减趋势符合指数衰减，脉冲间隔特征值为 2 ms。结果表明，随着脉冲间隔的增大，相邻脉冲之间热量累计效应降低，波导内部温度变化值随之降低。

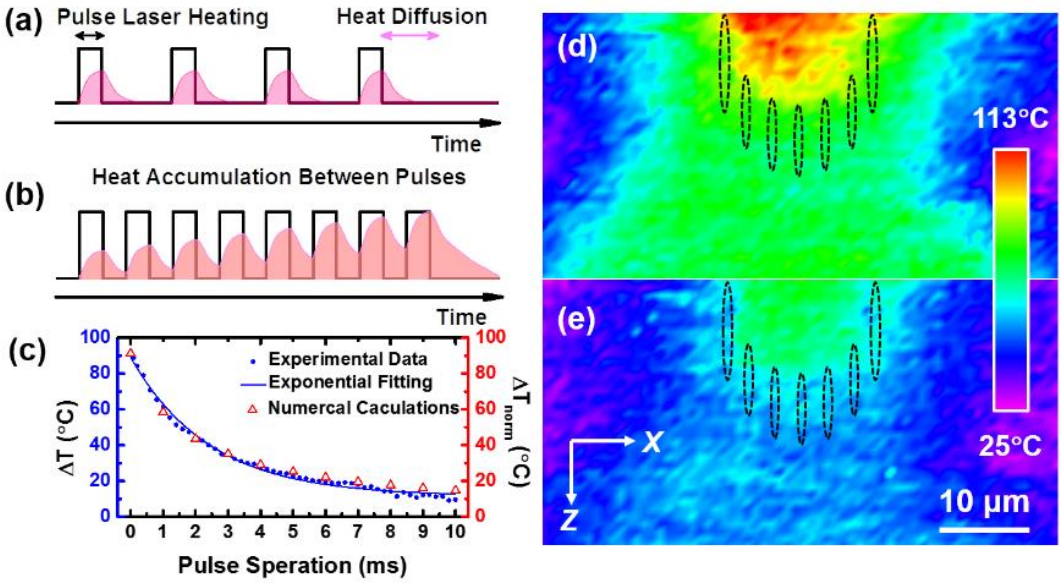

图 5.2.6 980 nm 泵浦脉冲激光序列加热和热扩散过程的示意图：（a）脉冲间隔足够长使得热扩散作用将热量在下一个脉冲到来之前扩散至初始状态；（b）脉冲间隔较短，产生热量累计。（c）归一化的实验（蓝色）和模拟（红色）所得波导温度随脉冲间隔的变化。峰值功率固定为 60 mW，脉宽固定为 2 ms。（d）为 60 mW 连续激光泵浦下的波导截面二维热成像。（e）为峰值功率 60 mW，脉宽 2 ms，脉冲间隔 2 ms 的脉冲激光泵浦下的波导截面二维热成像。黑色虚线标示了飞秒激光写入痕迹的位置

图 5.2.6（d）和（e）分别为连续和脉冲激光泵浦时波导截面二维热成像。连续激光为 60 mW，泵浦激光峰值功率为 60 mW，脉宽为 2 ms，脉冲间隔为 2 ms，脉冲能量为 120 nJ。结果表明：热成像分布基本一致，主要温度变化集中在波导内部，对于泵浦光的时间调制并没有影响到热量的空间分布，由飞秒激光写入痕迹组成的热阻限制了热量的扩散。另一方面，经时间调制后，波导温度升高现象

得到明显改善，其中波导温度升高最大值由 113℃降至 60℃，表明时间调制泵浦光的方法有利于降低波导的泵浦热效应。

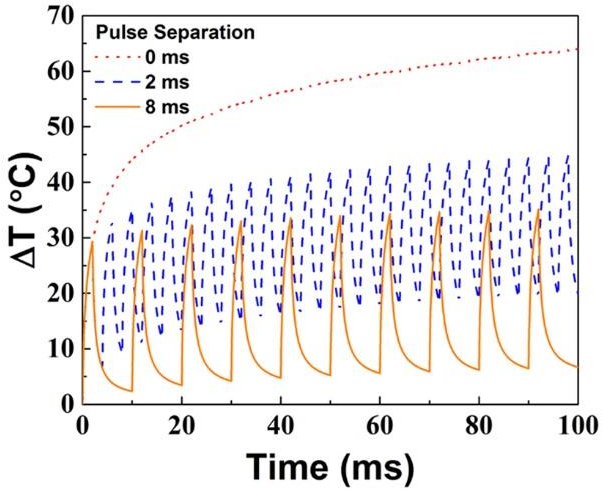

图 5.2.7 模拟波导温度随时间的变化，泵浦光分别为 60 mW 的连续激光（红色点），峰值功率 60 mW，脉宽 2 ms，脉冲间隔分别为 2 ms（蓝色虚线）和 8 ms（黄色实线）的脉冲激光

为进一步验证本文实验和观点的正确性，我们采用有限差分法对热扩散方程进行了模拟计算，其中所涉及的热学和光谱性质采用铒镱共掺磷酸盐玻璃文献[42,43]中的数据。如图 5.2.7 所示，不同时间调制下的泵浦激光所引起的波导温度变化随时间的变化大有不同：

i. 在连续激光泵浦下，当泵浦光吸收导致的加热速率与样品和环境温差导致的热耗散速率相同时，达到饱和；

ii. 当使用脉宽为 2 ms 的脉冲激光泵浦时，脉冲激光使得波导温度升高，随后热量在下一个脉冲到来之前耗散，但是脉冲间隔时间不足以使得全部热量耗散，产生热量累计，进而温度升高，但仍低于连续激光泵浦下的温度；

iii. 当使用脉宽为 8 ms（远大于特征热弛豫时间）时，脉冲激光同样使得波导温度升高，不同于第二种情况，热量几乎完全的消散，相邻脉冲之间基本无热量累计，因此所引起的波导温度升高也可忽略。

另外，模拟的波导温度变化随脉冲间隔的变化与实验数据（图 5.2.6（c））很好的吻合，进一步验证了本节观点。

5.2.3 小结

本实验采用飞秒激光写入技术在铒镱共掺磷酸盐玻璃中制备了表面型通道光波导。采用“泵浦+探测”系统，利用铒离子的双光子吸收，测量波导的三维微荧光特性，根据荧光强度比率法获得波导在 980 nm 激光泵浦下的三维高分辨率热成像。当泵浦光的功率为 120 mW 时，波导内部升温最高处达 200℃，且大部分热量集中在飞秒激光写入痕迹包裹的内部。为降低泵浦致波导温度升温，对泵浦光采用时间调制，并在理论和实验上证明了该方法的可行性。本工作为荧光比率分析法测量波导温度及调制温度变化打开了新的思路，该方法可利用于具有荧光特性的其他它光学器件的热效应研究，对于优化器件功能有重要的意义。本节相关工作结果发表于 *Optics Express* **24**, 16156–16166 (2016)。

参考文献

1. W. Koechner, Appl. Opt. **9**, 2548–2553 (1970).
2. A. J. Glass and A. H. Guenther, Appl. Opt. **12**, 637–649 (1973).
3. M. B. Bavil and E. Safari, J. Mech. Sci. Technol. **28**, 3231–3236 (2014).
4. G. Schreiber, H. Suche, Y. L. Lee, W. Grundkötter, V. Quiring, R. Ricken, and W. Sohler, Appl. Phys. B **73**, 501–504 (2014).
5. A. M. Guzman, M. Goryawala, J. Wang, A. Barreto, J. Andrian, N. Rishe, and M. Adjouadi, IEEE J. Biomed. Health Inf. **17**, 214–222 (2013).
6. R. J. Pylkki, P. J. Moyer, and P. E. West, J. Appl. Phys. **33**, 3385–3790 (1994).
7. Y. Yang, Z. Guo, S. Wang, D. Cai, J. Wen, and L. Wang, Acta Photonica Sinica **34**, 202–204 (2005).
8. P. Löw, B. Kim, N. Takama, and C. Bergaud, small **4**, 908-914 (2008).
9. C. D. S. Brites, P. P. Lima, N. J. O. Silva, A. Millán, V. S. Amaral, F. Palacio, and L. D. Carlos, Nanoscale **4**, 4799–4829 (2012).
10. H. S. Peng, S. H. Huang, and O. S. Wolfbeis, J. Nanopart. Res. **12**, 2729–2733 (2010).
11. E. C. Ximendes, W. Q. Santos, U. Rocha, U. K. Kagola, F. Sanz-Rodríguez, N. Fernández, A. da Silva Gouveia-Neto, D. Bravo, A. M. Domingo, B. del Rosal, C. D. S. Brites, L. Dias Carlos, D. Jaque, and C. Jacinto, Nano Lett. **16**, 1695–1703 (2016).
12. 姚建铨，徐德刚. 全固态激光及非线性光学频率变换技术，科学出版社，2007.
13. A. A. Kaminskii, Laser & Photon. Rev. **1**, 93-177 (2007).
14. Y. F. Lu, X. H. Zhang, J. Xia, G. Y. Jin, J. G. Wang, X. D. Yin, and A. F. Zhang, Laser Phys. Lett. **7**, 335–338 (2010).
15. A. Ikesue and Y. L. Aung, Nat. Photon. **2**, 721–727 (2008).
16. Y. Ren, N. Dong, F. Chen, A. Benayas, D. Jaque, F. Qiu, and T. Narusawa, Opt. Lett. **35**, 3276–3278 (2010).
17. Y. Yao, Y. Tan, N. Dong, F. Chen, and A. A. Bettiol, Opt. Express **18**, 24516–24521 (2010).

18. H. Liu, J. R. Vázquez de Aldana, B. del Rosal Rabes, and F. Chen, Opt. Mater. **39**, 125–129 (2015).
19. Y. Jia, Y. Tan, C. Cheng, J. R. Vázquez de Aldana, and F. Chen, Opt. Express **22**, 12900–12908 (2014).
20. H. Liu, C. Cheng, C. Romero, J. R. Vázquez de Aldana, and F. Chen, Opt. Express **23**, 9730–9735 (2015).
21. J. A. Hutchinson and T. H. Allik, Appl. Phys. Lett. **60**, 1424–1426 (1992).
22. Z. P. Cai, A. Chardon, H. Y. Xu, P. Feron, and G. M. Stephan, Opt. Commun. **203**, 301–313 (2002).
23. T. Yanagisawa, K. Asaka, K. Hamazu, and Y. Hirano, Opt. Lett. **26**, 1262–1264 (2001).
24. 车继波，杨亚培，刘爽，官周国，薛辉. Er^{3+} / Yb^{3+}共掺磷酸盐玻璃光纤放大器的增益综述. 激光技术 **30**, 82–85 (2006).
25. A. Shooshtari, P. Meshkinfam, T. Touam, M. P. Andrews, and S. I. Najafi, Opt. Eng. **37**, 1188–1192 (1998).
26. G. W. Shao, G. L. Jin, and Q. Li, Opt. Eng. **47**, 104201 (2008).
27. S. F. Wong, E. Y. B. Pun, and P. S. Chung, IEEE Photon. Technol. Lett. **14**, 80–82 (2002).
28. A. Ródenas, G. A. Torchia, G. Lifante, E. Cantelar, J. Lamela, F. Jaque, L. Roso, and D. Jaque, Appl. Phys. B **95**, 85–96 (2009).
29. A. Benayas, B. del Rosal, A. Pérez-Delgado, K. Santacruz-Gómez, D. Jaque, G. A. Hirata, and F. Vetrone, Adv. Opt. Mater. **3**, 687–694 (2015).
30. Y. Bellouard, E. Barthel, A. A. Said, M. Dugan, and P. Bado, Opt. Express **16**, 19520–19534 (2008).
31. A. Benayas, E. Escuder, and D. Jaque, Appl. Phys. B **107**, 697–701 (2012).
32. M. E. Innocenzi, H. T. Yura, C. L. Fincher, and R. A. Fields, Appl. Phys. Lett. **56**, 1831–1833 (1990).
33. A. Benayas, W. F. Silva, C. Jacinto, E. Cantelar, J. Lamela, F. Jaque, J. R. Vázquez de Aldana, G. A. Torchia, L. Roso, A. A. Kaminskii, and D. Jaque, Opt.

Lett. **35**, 330–332 (2010).

34. E. C. Ximendes, U. Rocha, C. Jacinto, K. U. Kumar, D. Bravo, F. J. Lopez, E. M. Rodriguez, J. Garcia-Sole, and D. Jaque, Nanoscale **8**, 3057–3066 (2016).
35. V. K. Rai, Appl. Phys. B **88**, 297–303 (2007).
36. L. Marciniak, K. Waszniewska, A. Bednarkiewicz, D. Hreniak, and W. Strek, J. Phys. Chem. C **120**, 8877–8882 (2016).
37. S. Chénais, S. Forget, F. Druon, F. Balembois, and P. Georges, Appl. Phys. B **79**, 221–224 (2004).
38. J. Petit, B. Viana, and P. Goldner, Opt. Express **19**, 1138–1146 (2011).
39. Y. Z. Xu, H. Y. Tam, S. Y. Liu, and M. S. Demokan, IEEE Photonics Technol. Lett. **10**, 1253–1255 (1998).
40. Y. P. Lan, Y. F. Chen, and S. C. Wang, Appl. Phys. B **71**, 27–31 (2000).
41. S. R. Bowman, S. P. O'Connor, and S. Biswal, IEEE J. Quantum Electron. **41**, 1510–1517 (2005).
42. J. F. Philipps, T. Töpfer, H. Ebendorff-Heidepriem, D. Ehrt, and R. Sauerbre, Appl. Phys. B **72**, 399–405 (2001).
43. B. Lai, L. Feng, J. Wang, and Q. Su, Opt. Mater. **32**, 1154–1160 (2010).

第六章 飞秒激光写入铌酸锂晶体包层通道光波导

铌酸锂晶体（$LiNbO_3$）属三方晶系，负单轴晶，熔点 1530 K，密度 4.628 g/cm^3，透光范围为 370 nm~5200 nm，具有较高的折射率，且双折射率差值大（$n_e = 2.203$, $n_o = 2.286$ @ 632.8 nm），非线性系数高，机械性能稳定，耐高温，抗腐蚀，具有优良的声光、电光、光折变、压电、铁电等性质。提拉法可以生长大尺寸、均匀性好的块状铌酸锂材料，成本低，易加工。铌酸锂晶体被广泛利用于光电调制、倍频、光参量振荡、红外探测、光折变等领域[1-6]。

迄今为止，人们已经利用质子交换、湿法刻蚀、飞秒激光写入、干法刻蚀、金属离子扩散、离子注入、脉冲激光沉积等方法制备铌酸锂光波导[7-13]。本章主要通过飞秒激光写入技术，在 $LiNbO_3$ 晶体中制备圆形包层通道光波导，研究波导的折射率分布、传输模式和传输损耗等导波特性。

6.1 实验过程

本实验采用 *x* 切 $LiNbO_3$ 晶体，尺寸为 1 (*x*) × 10 (*y*) × 10 (*z*) mm^3，其六面均经过光学抛光。具体实验过程如下：

i. 波导的制备

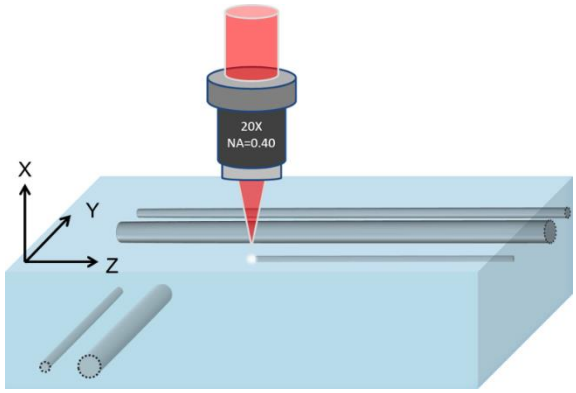

图 6.1 飞秒激光写入 $LiNbO_3$ 晶体制备包层光波导的示意图

利用飞秒激光技术对 $LiNbO_3$ 晶体进行加工，制备圆形包层通道光波导。飞秒激光的工作中心波长为 800 nm，脉宽为 120 fs，重复频率为 1 kHz。加工过程中，样品被放置在空间分辨率为 100 nm 的三维电动平台上，飞秒激光经过中性滤波片、半波片和线偏振片后，由显微物镜（20×, N.A.=0.40）垂直聚焦在 $LiNbO_3$ 晶体 *xz* 表面下深度~150 μm 处，扫描速率为 500 μm/s，相邻写入痕迹间距为 3 μm。铌酸锂晶体作为一种双折射晶体，沿不同切向写入的波导的性质具有一定的差别。我们分别在两个相对的 *xz* 表面，沿不同的方向写入了两组圆形包层通道光波导，图 6.1 为飞秒激光写入铌酸锂晶体的制备示意图。波导参数如表 6.1 所示。

表 6.1 飞秒激光写入 $LiNbO_3$ 晶体制备包层光波导的参数

波导	直径 (μm)	波导传输方向	飞秒激光能量（μJ）
No. 1	50	*z*	2.1
No. 2	110	*z*	2.1
No. 3	50	*y*	5.04
No. 4	110	*y*	5.04

ii．波导导波性能和退火处理

基于端面耦合系统对 $LiNbO_3$ 波导在可见光、近红外和中红外的导波性能进行测试。分别采用波长为 632.8 nm 的氦氖激光器，波长为 1064 nm 的固体激光器（MIL-III1064, CNI Optoelectronics Co. Ltd），和波长为 4 μm 的可调谐激光系统（MIRTM 8025, Daylight Solutions, Inc.）作为入射激光光源。激光在经过半波片或偏振片调节偏振方向后，由显微物镜或透镜聚焦到波导的端面，出射激光由显微物镜收集，经过孔阑后被 CCD 和功率计等设备采集和测量。

为优化波导的导波性能，将样品在开放式退火炉中以 260℃退火 1 小时。

6.2 结果与讨论

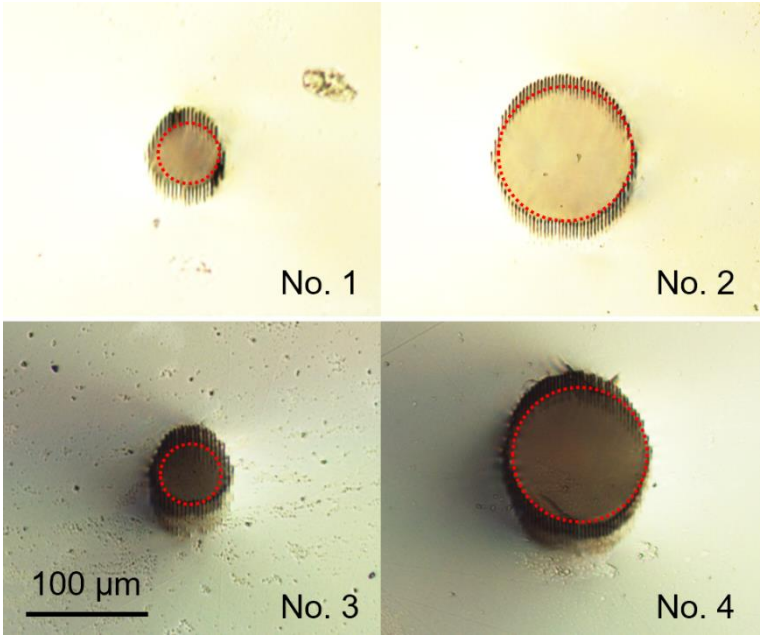

图 6.2 $LiNbO_3$ 晶体包层光波导 Nos. 1-4 的显微镜图，其中红色虚线为飞秒激光写入痕迹位置，其所包围的圆形区域为波导区域

图 6.2 为 $LiNbO_3$ 晶体包层光波导端面的显微镜照片。飞秒激光多次写入间隔为 3 μm 的痕迹，这些写入痕迹由于激光写入过程中双光子吸收引发雪崩电离等效应，折射率降低，组成一个准连续的包层结构，而内部所包裹区域形成光波导。

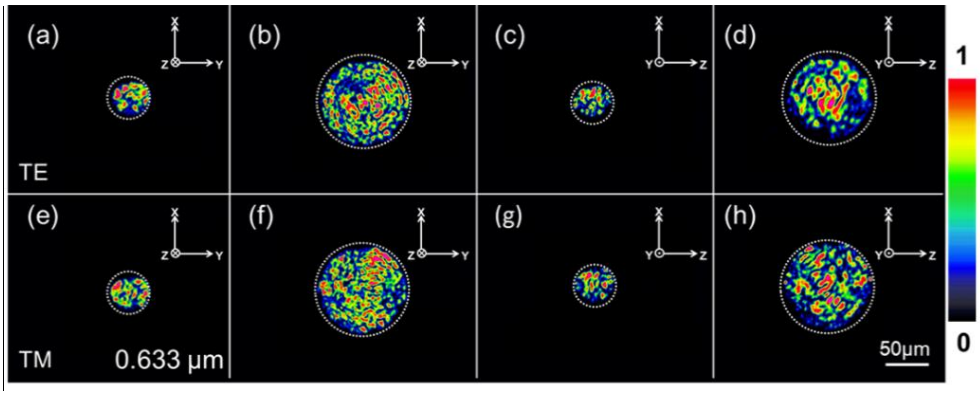

图 6.3 包层光波导在 632.8 nm 波长下近场光强分布：(a)−(d) TE 偏振和 (e)−(h) TM 偏振

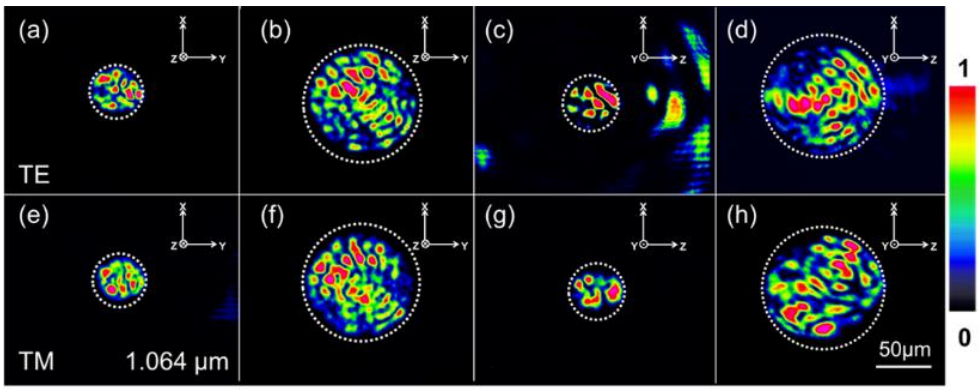

图 6.4 包层光波导在 1064 nm 波长下近场光强分布：(a)-(d) TE 偏振和 (e)-(h) TM 偏振

图 6.3、图 6.4 和图 6.5 分别为 632.8 nm、1064 nm 和 4 μm 波长下的 $LiNbO_3$ 包层光波导的近场光强分布，并标示了铌酸锂的晶轴和入射光的偏振方向（n_e 或 n_o），实验结果分析如下：

i) 近场光强分布具有清晰的边界，紧凑地分布于圆形包层（图 6.3、图 6.4 和图 6.5 中虚线）内，表明飞秒激光写入痕迹组成的圆形包层结构可以很好的将光限制在波导内部传输；

ii) 在 632.8 nm 和 1064 nm 下，50 μm 和 110 μm 的波导均支持多模传输，1064 nm 下的呈现低阶模式；随着波长增大，在 4 μm 下，直径为 50 μm 的波导 No. 1 和 No. 3 支持单模传输；而直径为 110 μm 的波导 No. 2 和 No. 4 仍为多模传输，这也表明通过适当的增大波导的直径，可使其支持直至红外 5.5 μm（$LiNbO_3$ 的最大透光波长）的导波传输。

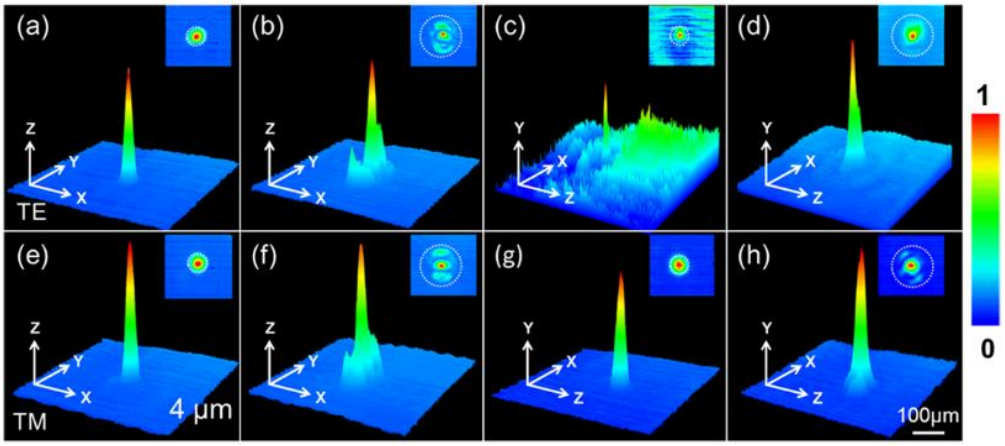

图 6.5 包层光波导在 4 μm 波长下近场光强分布：(a)-(d) TE 偏振和 (e)-(h) TM 偏振

iii) 本实验制备的光波导同时支持寻常光(n_o)和异常光(n_e)偏振方向的导波。在以往报道的飞秒激光写入 $LiNbO_3$ 制备的光波导中，折射率升高型波导仅仅支持 n_e 偏振方向的导波[14-16]，双线型光波导虽可以支持 n_e 和 n_o 两个偏振方向的导波，但是 n_o 方向损耗较大，对于光的限制较弱[17,18]。本实验所制备的圆形包层光波导在两个偏振方向均具有良好的传输特性。

表 6.2 $LiNbO_3$ 圆形包层光波导的最大折射率变化（10^{-3}）

波导	TE	TM
No. 1	4.1 (n_o)	4.1 (n_o)
No. 2	5.1 (n_o)	5.1 (n_o)
No. 3	1.6 (n_e)	3.4 (n_o)
No. 4	3.1 (n_e)	4.9 (n_o)

为进一步分析波导的性质，我们重构了波导的二维折射率分布。首先，利用数值孔径法，测量波导的最大折射率变化，结果列在表 6.2 中。其中可以看出，n_e 方向的折射率变化明显低于 n_o 方向的折射率变化，这也可以解释图 5（c），（d）中波导对于光的限制较弱的表现。根据二维圆形包层光波导的结构，重构了波导 No. 1 的折射率分布（图 6.6（a）），模拟了 TE 偏振方向的 4 μm 激光在波导 No. 1 中的传输，其传输模式如图 6.6（b）所示。模拟结果和实验结果相吻合，表明了重构的折射率分布的合理性。

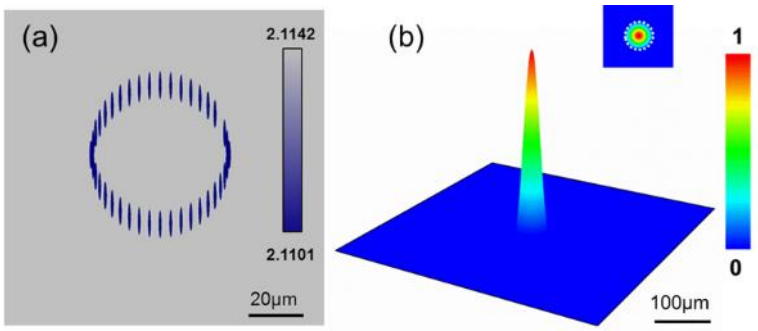

图 6.6 包层光波导 No. 1 在 TE 偏振的 4 μm 激光的（a）折射率重构，及（b）模拟的近场光强分布

表 6.3 $LiNbO_3$ 包层光波导的插入损耗（α）

波导	TE/TM	α (dB) before annealing			α (dB) after annealing		
		0.633 μm	1.064 μm	4 μm	0.633 μm	1.064 μm	4 μm
No. 1	TE	3.2	2.2	4.9	2.7	1.7	4.3
	TM	3.4	2.3	5.0	2.9	1.6	4.3
No. 2	TE	1.2	1.5	4.4	1.0	0.5	3.0
	TM	1.2	1.6	4.3	1.0	0.5	3.0
No. 3	TE	10.2	7.3	12.7	7.1	3.3	12.4
	TM	7.4	3.9	5.9	3.6	2.6	5.0
No. 4	TE	7.0	3.4	8.6	5.2	2.0	7.1
	TM	3.0	1.7	4.9	1.8	0.8	3.7

波导的插入损耗的计算结果如表 6.3 所示，在可见光（0.633 μm），近红外（1.064 μm）和中红外（4 μm）波段，都遵循以下规则:

I. 对于波导的尺寸，在 TE 和 TM 偏振下，直径为 110 μm 的波导的损耗均小于直径为 50 μm 的波导，即 $\alpha_1 > \alpha_2$，$\alpha_3 > \alpha_4$ @ TE 和 TM。

II. 对于波导 No. 1 和 No. 2，沿 TE 和 TM 偏振方向均对应于晶体的寻常光方向（n_o），波导在两个偏振方向的插入损耗差别较小，即 $\alpha_{1,\,TE} \approx \alpha_{1,\,TM}$，$\alpha_{2,\,TE} \approx \alpha_{2,\,TM}$。

III. 对于波导 No. 3 和 No. 4，TE 偏振方向为晶体的异常光（n_e）方向，TM

偏振方向为晶体的寻常光（n_o）方向，由于 n_e 方向折射率改变量较小，对光线的限制能力较差（见上文），导致沿 n_e 方向的插入损耗较大，即 $\alpha_{3,\ TE} > \alpha_{3,\ TM}$，$\alpha_{4,\ TE} > \alpha_{4,\ TM}$。

IV. 结合上述波导尺寸和偏振对波导损耗的影响，可以得出四个不同参数波导的损耗之间的大小关系：$\alpha_3 > \alpha_4 > \alpha_1 > \alpha_2$ @ TE, $\alpha_3 > \alpha_1 > \alpha_4 > \alpha_2$ @ TM。

退火后波导的插入损耗见表 6.3，退火后波导的性质得到了提高，且各个波导在不同偏振方向下的损耗仍然遵循上述规律，其中损耗最小的一个波导仍为 No. 2，在不同波长下的损耗分别为 1.0 dB @ 632.8 nm，0.5 dB @ 1064 nm 和 3.0 dB @ 4 μm。与之前报道的飞秒激光写入制备铌酸锂光波导相比较，二类双线型波导的传输损耗为 1 dB/cm[19] 或 4 dB/cm[20] @ 633 nm，及 0.6 dB/cm[21] @ 1064 nm，一类折射率升高型光波导在 1550 nm 下的最小插入损耗为 3.5 dB[22]。本实验的波导性质优异，具有良好的导波性质，较小的损耗。

6.3 小结

本实验采用飞秒激光写入技术，在 *x* 切铌酸锂晶体中成功制备了沿晶体不同晶向传输的圆形包层波导。通过对波导在可见光、近红外至中红外波段的导波性质的研究，实现了沿寻常光和异常光偏振方向的导波传输，其中直径为 50 μm 的波导支持在 4 μm 下的单模传输。经过 260℃高温退火一小时，波导的传输性质得到了提高，其中性质最优异的波导 No. 2 在 1064 nm 波长下的插入损耗低至 0.5 dB，表现了优良的传输性质。本实验说明铌酸锂晶体包层光波导是集成光子器件中高功率密度、小型化器件的重要选择。本节相关工作结果发表于 *Optical Materials Express* **3**, 13785–1384 (2013)。

参考文献

1. P. D. Townsend, P. J. Chandler, and L. Zhang, Optical Effects of Ion Implantation (Cambridge University Press, 1994).
2. K. K. Wong, Properties of Lithium Niobate (INSPEC, 2002).
3. 孔勇发，多功能光电材料——铌酸锂晶体，科学出版社，2005.
4. 杨春晖，光折变非线性光学材料：铌酸锂晶体，科学出版社，2009.
5. F. Chen, J. Appl. Phys. **106**, 081101 (2009).
6. S. Ringleb, K. Rademaker, S. Nolte, and A. Tünnermann, Appl Phys B **102**, 59–63 (2011).
7. Yu. N. Korkishko and V. A. Fedorov, J. Appl. Phys. **82**, 1010 (1997).
8. H. Hu, R. Ricken, W. Sohler, and R. B. Wehrspohn，IEEE Photon. Technol. Lett. **19**, 417–419 (2007).
9. A. Ródenas, L. M. Maestro, M. O. Ramírez, G. A. Torchia, L. Roso, F. Chen, and D. Jaque, J. Appl. Phys. **106**, 013110 (2009).
10. X. Xia, Q. Chen, C. Tsay, C. B. Arnold, and C. K. Madsen, Opt. Lett. **35**, 3228–3230 (2010).
11. M. Quintanilla, E. M. Rodríguez, E. Cantelar, F. Cussó, and C. Domingo, Opt. Express **18**, 5449–5458 (2010).
12. N. N. Dong, F. Chen, and D. Jaque, Opt. Express **18**, 5951–5956 (2010).
13. H. Hu, A. P. Milenin, R. B. Wehrspohn, H. Hermann, and W. Sohler, J. Vac. Sci. Technol. A **24**, 1012 (2006).
14. R. Osellame, M. Lobino, N. Chiodo, M. Marangoni, G. Cerullo, R. Ramponi, H. T. Bookey, R. R. Thomson, N. D. Psaila, and A. K. Kar, Appl. Phys. Lett. **90**, 241107 (2007).
15. J. Burghoff, C. Grebing, S. Nolte, and A. Tünnermann, Appl. Surf. Sci. **253**, 7899–7902 (2007).
16. J. Burghoff, H. Hartung, S. Nolte, and A. Tünnermann, Appl. Phys. A **86**, 165–170 (2007).
17. S. Zhang, J. Yao, Q. Shi, Y. Liu, W. Liu, Z. Huang, F. Lu, and E. Li, Appl. Phys.

Lett. **92**, 231106 (2008).

18. W. Horn, S. Kroesen, J. Herrmann, J. Imbrock, and C. Denz, Opt. Express **20**, 26922–26928 (2012).
19. Y. Liao, J. Xu, Y. Cheng, Z. Zhou, F. He, H. Sun, J. Song, X. Wang, Z. Xu, K. Sugioka, and K. Midorikawa, Opt. Lett. **33**, 2281–2283 (2008).
20. M. Heinrich, A. Szameit, F. Dreisow, S. Döring, J. Thomas, S. Nolte, A. Tünnermann, and A. Ancona, Appl. Phys. Lett. **93**, 101111 (2008).
21. J. Burghoff, S. Nolte, and A. Tünnermann, Appl. Phys., A Mater. Sci. Process. **89**, 127–132 (2007).
22. H. T. Bookey, R. R. Thomson, N. D. Psaila, A. K. Kar, N. Chiodo, R. Osellame, and G. Cerullo, IEEE Photon. Technol. Lett. **19**, 892–894 (2007).

第七章 总结

本论文主要介绍了利用飞秒激光微加工技术在透明光学材料中制备通道光波导和波导分支器件，并对其导波特性、激光性质和热成像等进行了详细的研究。主要研究的光学材料包括锗酸铋（BGO）晶体、钕掺杂钒酸钇（Nd:YVO_4）晶体、钕掺杂钇铝石榴石（Nd:YAG）晶体、铒镱共掺磷酸盐玻璃（Er:Yb:Phosphate glass）及铌酸锂（$LiNbO_3$）晶体。通过端面耦合系统，我们研究了所制备的波导及分支器的传输模式、损耗、折射率变化等；利用数值计算，模拟了波导及分支器结构的折射率分布和传输模式，对其制备参数进行了优化；利用石墨烯作为可饱和吸收体，实现了调 Q 脉冲激光振荡，并对其阈值、脉冲宽度、重复频率和单脉冲能量等激光特性进行了研究；利用荧光强度比率法对波导的温度进行了表征，详细研究了激光泵浦导致的波导温度变化。本论文为飞秒激光微加工技术应用于光波导器件的制备提供了理论和实验依据。

本章对本论文的主要研究内容进行了总结，并归纳主要创新点。

7.1 总结

I. 锗酸铋（BGO）晶体中的通道光波导及波导分支器

利用飞秒激光微加工技术在 BGO 晶体中制备了四条双线型通道光波导，其飞秒激光能量和双线间隔各不相同。基于端面耦合系统，测试了 632.8 nm 波长下光波导在 TE 和 TM 偏振下的导波特性。研究表明，双线型通道光波导支持 TE 和 TM 偏振下单模传输。折射率分析和传输模式模拟结果表明，在飞秒激光写入痕迹处折射率降低，两条写入痕迹中间所夹位置折射率升高，形成通道光波导。所制备的光波导损耗较高，且 TE 偏振下的损耗更高于 TM 偏振下，经过一系列的热退火处理，波导的传输特性得到了明显改善。优化的波导采用的飞秒激光制备参数为单脉冲能量为 2.52 μJ，写入痕迹间隔为 20 μm，所得到波导的传输损耗为 0.5 dB/cm。

利用飞秒激光微加工技术在 BGO 晶体中制备了包层通道光波导，波导的直径约为~100 μm。通过端面耦合技术得到波导在 632.8 nm 下的传输模式，经 260℃退火处理后，波导的传输损耗降至~2.1 dB/cm。相比于双线型波导，包层光波导具有偏振不敏感性。包层光波导由飞秒激光写入痕迹包围而成，可以更好的将光限制在波导内部传输。包层的形状有利于实现波导—光纤耦合。

利用飞秒激光微加工技术在 BGO 晶体中制备了折射率升高型通道光波导。在飞秒激光制备参数上，采用较低的单脉冲能量（0.14 μJ），使得写入区域性质得到了很好的保存。波导经飞秒激光多次扫描组成矩形区域，支持在 4 μm 中红外波长下 TE 和 TM 偏振的单模传输，且具有偏振不敏感性，在各偏振方向下导波性质一致。尺寸为 16.4 × 18.3 μm^2 和 32.2 × 37.0 μm^2 的波导传输损耗分别约为 3.5 dB/cm 和 3.4 dB/cm。与飞秒激光写入其它晶体制备的折射率升高型光波导相比，BGO 折射率升高型光波导具有优异的导波性质。

利用飞秒激光微加工技术在 BGO 晶体中制备了二维（1 × 2）及三维（1 × 3，1 × 4）波导分支器。分支器结构由上面介绍的折射率升高型光波导组成，在制备过程中通过程序控制设计不同的分支形态。通过端面耦合系统，研究了分支器在 4 μm 波长下的导波和分支性质。结果表明，BGO 波导分支器均支持无偏振差异的单模传输，且分支比例接近 1:1，分支损耗较小约为~0.3 dB，分支器损耗约为 3.6 dB/cm，具有良好的分支性质。

II. 钕掺杂钒酸钇晶体（Nd:YVO_4）晶体中的通道光波导与调 Q 脉冲激光

采用飞秒激光微加工技术在 Nd:YVO_4 晶体中写入双线型通道光波导。基于端面耦合系统，得到波导在 1064 nm 的 TE 和 TM 偏振光下的近场模式分布均呈现单模模式。波导在 TE 和 TM 偏振光下的传输损耗分别为~1.2 dB/cm 和~1.9 dB/cm，激光阈值分别为 114 mW 和 197 mW。利用多层石墨烯作为可饱和吸收体，实现调 Q 脉冲激光的输出，激光最大输出功率为 129 mW，相应地，脉冲频率最高达 16.3 MHz，此时获得最大脉冲能量为 8.1 nJ，最小脉冲宽度为 25 ns。

采用飞秒激光微加工技术，在 Nd:YVO_4 晶体中制备了内外包层结构直径分别为 42 μm 和 114 μm 的双包层波导，及相应的单包层光波导。基于端面耦合系统，采用 820 nm 连续激光泵浦，石墨烯作为可饱和吸收体，实现 1065.2 nm 波导调 Q 脉冲激光输出。结果表明，单包层和双包层光波导均实现脉冲激光振荡，且波导的尺寸越小，TE 和 TM 偏振下的激光输出差异更大，双包层 TE 偏振下获得最优异的激光特性，最大输出功率为 361 mW，激光阈值为 103 mW，重复频率为 14.5 MHz，单脉冲能量为 24.9 nJ，脉宽为 31 ns。

III. 荧光强度比率法测量光波导的温度

利用飞秒激光微加工在 Nd:YAG 晶体中制备表面型通道光波导，波导的直径约为 17 μm。采用“泵浦+探测”系统结合高分辨率共聚焦显微技术，研究在 800 nm 激光泵浦下的波导微荧光特性，利用荧光强度比率法获得 Nd:YAG 波导的热成像。结果表明，在 100 mW 的 800 nm 激光泵浦下，波导内部温度升高约 10℃左右。经过实验分析和理论模拟证明，飞秒激光写入痕迹处折射率降低，将光限制在波导区域传输；同时写入痕迹的热导率大幅降低，形成热阻抗将热量限制在波导内部。本工作表明“泵浦+探测”系统可用于探测和监控波导导波或激光过程中的温度变化。

采用飞秒激光写入技术在铒镱共掺磷酸盐玻璃中制备了表面通道光波导。采用“泵浦+探测”系统，利用铒离子的双光子吸收，测量波导的三维微荧光特性，根据荧光强度比率法分析获得波导在 980 nm 激光泵浦下的三维高分辨率热成像。当泵浦光的功率为 120 mW 时，波导内部升温最高处达 200℃，且大部分热量集中在飞秒激光写入痕迹包裹的内部。为降低泵浦致波导温度升温，对泵浦光采用时间调制，并在理论和实验上证明了该方法的有效性。本工作为荧光比率法测量

波导温度及调制温度变化打开了新的思路，该方法可利用于具有荧光特性的其他光学器件的研究。

IV. 铌酸锂($LiNbO_3$）晶体中的包层光波导

采用飞秒激光微加工技术，在 *x* 切铌酸锂晶体中成功制备了分别沿晶体 *y*，*z* 方向传输的包层光波导。通过端面耦合技术对波导在可见光、近红外至中红外波段的导波性质进行了测试。结果表明，直径为 50 μm 和 100 μm 的包层光波导均支持可见光直至中红外的导波传输，其中直径为 50 μm 的波导支持在 4 μm 下的单模传输。利用 260℃高温退火提升波导的传输性质，性质最优异的波导在 1064 nm 波长下的插入损耗低至 0.5 dB，表现了优良的导波性质。

7.2 主要研究创新点

1. 利用飞秒激光微加工技术在 BGO 晶体中制备了折射率升高型、双线型、包层光波导及三维波导分支器结构。通过对飞秒激光参数的调试，在 BGO 晶体中成功制备不同的波导及分支器形态，并具有良好的导波性质。折射率升高型波导及分支器结构具有制备简单、结构灵活、可支持中红外传输的优点；双线型波导结构稳定，在 600℃高温退火下仍然性质稳定，波导损耗低至 0.5 dB/cm；包层光波导对光的限制能力较强，且支持各偏振方向下的无差别导波。对不同参数、不同形态的 BGO 晶体通道光波导的研究，有利于理解分析波导形成原理及特性，对其在波导集成器件的应用提供基础。
2. 利用飞秒激光微加工技术在 Nd:YVO_4 晶体中制备双线型，圆形单包层和双包层波导结构，并在波导结构中实现调 Q 脉冲波导激光振荡。包层与双线型波导相比，导波性能和激光性能大幅提升，其中双包层波导结构得益于其较大的吸收横截面积，激光性能优异。研究工作为波导激光器的制备提供了数据支持。
3. 利用荧光比率法首次表征了 Nd:YAG 晶体和钕镱共掺磷酸盐玻璃光波导的温度。实现了波导在泵浦条件下的三维高分辨率热成像。在 Nd:YAG 晶体中，波导升温约为 10℃，而在钕镱共掺磷酸盐玻璃中，由于其热热系数较低，波导升温高达 200℃。理论和实验上证明了时间调制泵浦光的方法可以有效降低波导在泵浦下的温度升高。研究工作开创了利用荧光比率法测量和监控集新成光子器件温度变化的新思路。

攻读博士学位期间发表的论文及获得的奖励

已发表论文：

1. **Two-photon luminescence thermometry: towards 3D high-resolution thermal imaging of waveguides**
   Ruiyun He, Javier R. Vázquez de Aldana, Ginés Lifante Pedrola, Feng Chen, and Daniel Jaque
   Optics Express **24**, 16156–16166 (2016).

2. **All-optical thermal microscopy of laser-excited waveguides**
   Ruiyun He, Javier R. Vázquez de Aldana, Ginés Lifante Pedrola, Feng Chen, and Daniel Jaque
   Optics Letters **41**, 2061–2064 (2016).

3. **Three-dimensional dielectric crystalline waveguide beam splitters in mid-infrared band by direct femtosecond laser writing**
   Ruiyun He, Javier R. Vázquez de Aldana, and Feng Chen
   Optics Express **22**, 31293–31298 (2014).

4. **Femtosecond laser micromachining of lithium niobate depressed cladding waveguides**
   Ruiyun He, Qiang An, Yuechen Jia, Gabriel R. Castillo-Vega, Javier R. Vázquez de Aldana, and Feng Chen
   Optical Materials Express **3**, 1378–1384 (2013).

5. **Passively Q-switched Nd:YVO_4 waveguide laser using graphene as a saturable absorber**
   Ruiyun He, Javier R. Vázquez de Aldana, and Feng Chen
   Optical Materials **39**, 125–129 (2015).

6. **Embedded silver nanoparticles in KTP crystal produced by ion implantation**
   Ruiyun He, Feng Ren, and Feng Chen
   Materials Letters **193**, 158–160 (2017).

7. **Femtosecond laser micromachined optical waveguides in $Bi_4Ge_3O_{12}$ crystals**
   Ruiyun He, Qiang An, Javier R. Vázquez de Aldana, Qingming Lu, and Feng Chen
   Applied Optics **52**, 3713–3718 (2013).

8. **Focused ion-beam writing of channel waveguides in bismuth germanate crystal for telecommunication bands**
   Ruiyun He, Sudheer Kumar Vanga, Andrew A. Bettiol, and Feng Chen
   Optical Engineering **54**, 057108 (2015).

9. **Planar optical waveguide in $SrTiO_3$ crystal fabricated by carbon ion irradiation**
   Ruiyun He, Shuqian Sun, Miaomiao Xu, Feng Chen, Shavkat Akhmadaliev, and Shengqiang Zhou
   Nuclear Instruments and Methods in Physics Research B **308**, 6–8 (2013).

10. **Graphene Q-switched laser operation in Nd:YVO_4 cladding waveguides produced by femtosecond laser writing**
    ***Ruiyun He*,** Javier R. Vázquez de Aldana, and Feng Chen
    Advanced Solid State Lasers 2014, OSA Technical Digest (online), paper AM5A.3.

11. **Optical lattice-like cladding waveguides by direct laser writing: fabrication, luminescence, and lasing**
    Weijie Nie, ***Ruiyun He***, Chen Cheng, Uéslen Rocha, Javier R. Vázquez de Aldana, Daniel Jaque, and Feng chen
    Optics Letters **41**, 2169–2064 (2016).

12. **Optical ridge waveguides in Er^{3+}/Yb^{3+} co-doped phosphate glass produced by ion irradiation combined with femtosecond laser ablation for guided-wave green and red upconversion emissions**
    Chen Chen, ***Ruiyun He***, Yang Tan, Biao Wang, Shavkat Akhmadaliev, Shengqiang Zhou, Javier R. Vázquez de Aldana, Lili Hu, and Feng Chen
    Optical Materials **51**, 185–189 (2016).

13. **Ridge waveguides in Nd:ABC_3O_7 disordered crystals produced by swift C^{5+} ion irradiation and precise diamond dicing: Broad band guidance and spectroscopic properties**
    Chen Chen, Qingfang Luan, ***Ruiyun He***, Chen Cheng, Shavkat Akhmadaliev, Shengqiang Zhou, Haohai Yu, Huaijin Zhang, and Feng Chen
    Optics & Laser Technology **68**, 84–88 (2015).

14. **Q-switched Nd:YAG channel waveguide laser through evanescent field interaction with surface coated graphene**
    Yang Tan, ***Ruiyun He***, John Macdonald, Ajoy Kumar Kar, and Feng Chen
    Applied Physics Letters **105**, 101111 (2014).

15. **Optical waveguides in $LiTaO_3$ crystals fabricated by swift C^{5+} ion irradiation**
    Guiyuan Liu, ***Ruiyun He***, Shavkat Akhmadaliev, Javier R. Vázquez de Aldana, Shengqiang Zhou, and Feng Chen
    Nuclear Instruments and Methods in Physics Research B **325**, 43–46 (2014).

16. **Polarization-dependent optical absorption of MoS_2 for refractive index sensing**
    Yang Tan, ***Ruiyun He***, Chen Cheng, Dong Wang, Yanxue Chen, and Feng Chen
    Scientific Reports **4**, 7523 (2014).

17. **Femtosecond laser micromachined optical waveguides in $LiTaO_3$ crystal**
Miaomiao Xu, ***Ruiyun He***, Shuqian Sun, Javier R. Vázquez de Aldana, and Feng chen
Physica Status Solidi (RRL)-Rapid Research Letters **7**, 1014–1017 (2013).

参加的国内及国际会议:

1. **17th National Conference of Optics and Ptophysics**

Luminescence Thermometry: 3D high-resolution thermal imaging of waveguides
Chongqing Universiy of Arts and Sciences, Chongqing, China (October, 2016).

2. **XIV Congreso Nacional de Materiales**

Thermal imaging of ultrafast laser inscribed waveguides
Universidad de Oviedo, Gijón, Spain (June, 2016).

3. **Pacific Rim Laser Damage 2015**

A three-dimensional mid-infrared 1×6 waveguide beam splitter produced by direct femtosecond laser writing
Jiading, Shanghai, China (May, 2015).

4. **Optical frontier–The 10th National Conference on Laser Technology and Optoelectronics**

Continuous wave laser generation in Nd:YVO_4 channel waveguide produced by femtosecond laser inscription
Pudong, Shanghai, China (March, 2015).

5. **Advanced Solid State Lasers (ASSL) Conference**

Graphene Q-switched laser operation in Nd:YVO_4 cladding waveguides produced by femtosecond laser writing
Hilton Shanghai Hongqiao, Shanghai, China (November, 2014).

6. **18th International Conference on Ion Beam Modifications of Materials**

Planar optical waveguides in $SrTiO_3$ crystal fabricated by swift heavy-ion irradiation
Shandong University, Qingdao, China (September, 2012).

获得的荣誉、奖励：

1. 2016年　　博士研究生国家奖学金
2. 2016年　　山东大学优秀研究生
3. 2016年　　博士生学业奖学金
4. 2015年　　博士生学业奖学金
5. 2014年　　山东大学第五届“五•四”青年科学奖
6. 2014年　　博士生学业奖学金
7. 2013年　　山东大学硕士研究生校长奖学金
8. 2013年　　硕士研究生国家奖学金
9. 2013年　　山东大学优秀研究生标兵称号

致　谢

五年的硕博连读生涯步入尾声，五年光阴之于人生是短暂的，五年生涯之于青春是蓬勃的，而五年历练之于未来是无价的。感恩在这五年里陪伴我的良师益友，在此向他们表示我最衷心的感谢！

首先感谢我的导师陈峰教授，本文工作是在陈峰教授的悉心指导下完成的。导师学识渊博，治学严谨，为人正直，诲人不倦，是我学习的榜样。导师在实验设计、数据分析和论文写作的各个阶段尽心尽力的指导，使我受益匪浅。我在研究生期间所获取的知识和进步都与导师的精心教导密切相关，在今后的工作我会时刻谨记导师的谆谆教诲，谨在此向导师表示最诚挚的敬意和最衷心的感谢。

感谢西班牙马德里自治大学材料物理系 Daniel Jaque 教授和 Ginés Lifante Pedrola 教授，两位学术造诣深厚、科研成果颇丰，在学习和科研给予我大量的鼓励和支持，在生活上予以我无微不至的关怀和帮助，使我的一年留学生涯收获颇多，在此对两位教授表示由衷的感谢和祝福。

感谢离子束应用实验室的诸位老师对我的鼓励和帮助，感谢王雪林教授、胡卉教授、王磊副教授、谭杨副教授、刘鹏老师、管婧工程师、陈明工程师对我的支持，和睦的工作氛围和良好的实验室条件使我的工作可以顺利进行。在此向各位老师表示诚挚的谢意。

山东大学化学与化工学院路庆明高级工程师在晶体生长和加工方面给予了大量的理论和技术支持，在此向路庆明老师表示由衷的感谢。

本论文是在国际合作者的倾心帮助下完成的。在这里感谢西班牙萨拉曼卡大学 Javier. R. Vázquez de Aldana 副教授和 Carolina R. Castillo-Vega 博士在飞秒激光微纳加工方面的支持；感谢西班牙罗维拉-维尔吉利大学 Airán Ródenas Seguí 副研究员对显微拉曼光谱测试的帮助。在此对各位学者表示衷心的感谢。

衷心感谢离子束课题组的师姐董宁宁、任莹莹、刘桂媛，师兄安强、姚一村、贾曰辰、刘洪亮、程亚洲，他们对我的科研和生活给予了悉心的指点和帮助，入学伊始即给我展示了一个积极向上的环境；感谢离子束课题组的师妹吕金蔓、聂伟杰、马利男、李玲琪，师弟程晨、陈琛、尚震、李让、李子琦，他们给我的工作提供了无私的帮助，给我的科研岁月带来了无限的温馨和乐趣。

感谢西班牙马德里自治大学材料物理系荧光成像实验组的老师 Jose García Solé, Francisco Jaque, Eugenio Cantelar,·Emma Martín Rodríguez, Dirk H. Ortgies, Patricia Haro-González，他们对我的研究工作的帮助和贡献不可或缺；感谢材料物理系秘书 Antonio Bravo López 和研究生办公室老师 Ana Amigo 对我的无私帮助；感谢学生 Blanca del Rosal，Jon Martínez de Mendívil，Erving C. Ximendes，Uéslen Rocha，Paloma Rodríguez-Sevilla，Lucía Labrador-Páez，胡杰，他们在异国他乡带给我温暖和欢乐，使我在西班牙度过一段快乐的时光。

感谢物理学院的领导和老师，他们工作认真、和蔼可亲，关心和支持我的工作。感谢我的同学，庆幸一路上有大家的陪伴。

感谢我的父母家人对我的关怀和爱护，他们的支持和理解是我坚强的后盾，他们的幸福是我前进的动力，在此献上我最诚挚的祝福和感谢。

结束即是开始，感恩亦是责任。

2017 年 4 月于山东大学

附三篇已发表论文

Letter Vol. 41, No. 9 / May 1 2016 / Optics Letters 2061

Optics Letters

All-optical thermal microscopy of laser-excited waveguides

Ruiyun He,[1,2] Javier Rodríguez Vázquez de Aldana,[3] Ginés Lifante Pedrola,[2] Feng Chen,[1] and Daniel Jaque[2,*]

[1]School of Physics, State Key Laboratory of Crystal Materials and Key Laboratory of Particle Physics and Particle Irradiation (MOE), Shandong University, Jinan 250100, China
[2]Fluorescence Imaging Group, Departamento de Física de Materiales, Facultad de Ciencias, Universidad Autónoma de Madrid, Madrid 28049, Spain
[3]Aplicaciones del Láser y Fotónica (ALF-USAL), Universidad de Salamanca, Salamanca 37008, Spain
*Corresponding author: daniel.jaque@uam.es

Received 9 February 2016; revised 16 March 2016; accepted 25 March 2016; posted 28 March 2016 (Doc. ID 259218); published 27 April 2016

We report on a unique combination of high-resolution confocal microscopy and ratiometric luminescence thermometry to obtain thermal images of 800 nm pumped ultrafast laser-inscribed waveguides in a Nd:YAG crystal. Thermal images evidence a strong localization of thermal load in the waveguide active volume. Comparison between experimental data and numerical simulations reveals that ultrafast laser-inscribed damage tracks in Nd:YAG crystals behave both as low-index and low-thermal conductivity barriers.

OCIS codes: (110.6820) Thermal imaging; (230.7380) Waveguides, channeled; (160.5690) Rare-earth-doped materials; (300.6280) Spectroscopy, fluorescence and luminescence; (140.3390) Laser materials processing.

http://dx.doi.org/10.1364/OL.41.002061

The appearance of light-induced temperature increments and temperature gradients is known to be one of the most critical parameters affecting photonic devices. As a widely studied example, pump-induced temperature increments in high power lasers have been demonstrated to be a limiting factor [1,2]. As a matter of fact, efficient heat dissipation in high-power solid-state lasers has been the object of extensive studies as a result of the appearance of sophisticated and efficient temperature stabilization systems. Temperature effects are expected to be even more critical and relevant in integrated photonic devices based on optical waveguides. Note that the performance of such elements is based on a reduced (10^{-2} – 10^{-3}) refractive index contrast. Since refractive index is, in most of the cases, a temperature dependent magnitude, the existence of local thermal loadings can lead to a modification of the refractive index contrast and, therefore, the confinement properties of the waveguide [3]. In addition, thermal measurements in optical waveguides are also of great interest from a pure fundamental point of view. Fabrication of optical waveguides requires microstructural modification of an initially homogeneous material. Intrawaveguide thermal imaging is essential to study how heat dissipation and diffusion takes place in such microstructured materials. Despite its great interest from an applied and fundamental point of view, thermal imaging of optical waveguides still remains as an almost unexplored research field.

The lack of experimental data concerning thermal imaging of optical waveguides results from the fact that the typical methods used for thermal imaging (such as infrared thermography) cannot be applied due to the micrometric dimensions of the optical active volume [4,5]. Experimental techniques for thermal imaging of waveguides should satisfy several requirements: submicrometric spatial resolution, subdegree thermal sensitivity, and complete absence of any physical contact. These three technical requirements are simultaneously satisfied by confocal luminescence thermometry (CLT), which is based on the extraction of thermal information from an appropriate analysis of the confocal fluorescence images of microsized devices. CLT has already been demonstrated to be a flexible and sensitive technique capable of providing three-dimensional thermal images of luminescent systems [6–8]. Nevertheless, its potential application for the acquisition of thermal images of integrated waveguides has not been yet demonstrated.

In this Letter, we provide experimental evidence of how high-resolution CLT can be successfully applied to obtain thermal images of active waveguides in the presence of optical excitation. In particular, this possibility has been demonstrated in ultrafast laser-inscribed (ULI) waveguides fabricated in Nd:YAG laser crystals and ceramics that are becoming one of the most promising, cost-effective, and flexible integrated devices [9–12]. The role played by the laser-modified local thermal conductivity of the Nd:YAG network on the spatial distribution of pump-induced heating is also discussed.

A schematic of the experimental setup used throughout this work is included in Fig. 1(a). The surface channel waveguide is fabricated by ULI as described elsewhere [12]. The top inset in Fig. 1(a) shows an optical transmission image of the waveguide cross section in which the presence of the damage tracks

0146-9592/16/092061-04 Journal © 2016 Optical Society of America

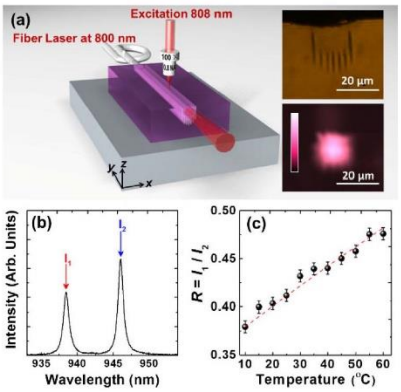

Fig. 1. (a) Schematic of the experimental setup. Insets show (top) the microscope image of the waveguide endface and (bottom) the spatial modal distribution at 800 nm. (b) Normalized microluminescence emission spectra around 940 nm. The two emission lines used for ratiometric thermal sensing are indicated. (c) Intensity ratio R as a function of temperature. Dots are experimental data and the dashed line corresponds to the linear fit.

is clearly observed. Seven damage tracks were inscribed forming a pseudo semicircle close to the crystal surface so that light could be confined between the crystal–air interface and the low-refractive index circular barrier [12].

Thermal loading in the Nd:YAG waveguide was investigated by using a "pump and probe" setup. The "pump" radiation was provided by an 800 nm laser diode coupled to a single-mode fiber that is pigtailed into one of the ends of the waveguide [Fig. 1(a)]. The bottom inset in Fig. 1(a) shows the waveguide mode at 800 nm, showing clear confinement between damage tracks and crystal surface. The Nd:YAG waveguide is placed into a homemade high resolution confocal microscope equipped with a 3-axes motorized stage. A second 808 nm laser beam (low power), serving as a "probe" beam, is focused into the sample by using a single long-working distance microscope objective (100 ×, 0.80 NA). The luminescence generated in the 920–950 nm spectral range, corresponding to the high energy lines within the $^4F_{3/2} \rightarrow {}^4I_{9/2}$ transition [13], is collected by the same microscope objective and analyzed by a high resolution spectrometer. A typical microluminescence spectrum is shown in Fig. 1(b). We focus on the spatial variation of the spectral properties of these two particular emission lines, as they have been demonstrated to be excellent probes to detect slight modifications in the microstructural properties of the YAG network [14]. In addition, recent works have demonstrated that the ratio between the emission intensities of these two lines was also used for high resolution remote temperature sensing [15]. Figure 1(c) shows the intensity ratio $R = I_1/I_2$, where I_1 and I_2 are the luminescence emitted intensities at 938 and 946 nm as obtained for different temperatures of the Nd:YAG crystal. From this calibration curve, it is possible to measure temperature with a ratiometric sensitivity close to 0.5%°C^{-1}. Thus, simultaneous cross-sectional scanning of the 808 nm "probe" spot and spectral analysis of collected luminescence provides simultaneously microstructural (damage, stress, and disorder), and thermal images of the waveguide. It is important to note that the power of the "probe" beam is not larger than 20 mW, so that it induced a negligible local heating.

Figure 2 presents the confocal fluorescence images of the waveguide's cross section based on the spatial variation of the spectral shift and width of the emission line at 945 nm, with and without 800 nm "pump" laser radiation propagating along the waveguide. These images were obtained at a distance of 100 μm from the waveguide's input face. It is clear that damage tracks are characterized by a broadening of the emission lines. This suggests the presence of well-localized damage of the Nd:YAG network [14]. This local damage is accompanied by a redshift that is attributed to a local densification at the damage tracks that is mechanically compensated by a local dilatation at their apexes [16]. Based on previous works, we conclude that ULI waveguides in crystalline materials are typically characterized by a low index (damage) cladding and a high index (compressed) core leading to strong light confinement between the crystal–air interface and the damage tracks [as observed in the inset of Fig. 1(a)].

The bottom row in Fig. 2 includes the fluorescence cross-sectional images of the waveguide as obtained in terms of the spatial variation of the intensity ratio R that is unequivocally related with the local Nd:YAG temperature, which was strongly modified with the 800-nm "pump" laser radiation propagating along the waveguide. Such change is further evidenced in Fig. 3(a), which shows the intensity ratio profiles obtained by the excitation beam scanning parallel to crystal surface [x axis in Fig. 1(a)] at a depth of 5 μm, either in presence or absence of 800 nm propagating radiation (the scan lines are indicated in Fig. 2 by dashed lines). In the absence of "pump" radiation propagating along the waveguide, the ratio decreases at the damage tracks and at the waveguide volume. When "pump" radiation is propagating along the waveguide, the intensity ratio profile is clearly modified. A slight increment in the ratio is found in the waveguide's surroundings, whereas inside the waveguide, the ratio increment becomes more pronounced. These changes are attributed to the temperature increment caused by the "pump" 800 nm radiation.

The temperature profile can be now calculated by taking the "laser-off" profile as background and by using the calibration curve of Fig. 1(c). As shown in Fig. 3(b), in our experimental

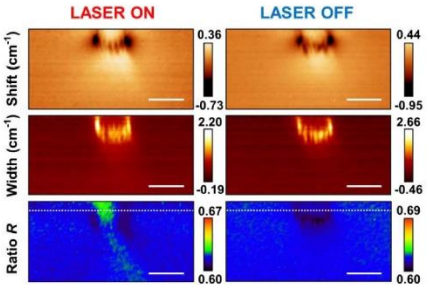

Fig. 2. Cross-sectional confocal fluorescence images of the ULI waveguide in Nd:YAG as obtained in terms of the spatial variation of the spectral shift, linewidth of the 945 nm emission line, and the intensity ratio R, obtained with (right column) and without (left column) of 800 nm radiation propagating along the waveguide. Scale bar is 20 μm in all the cases.

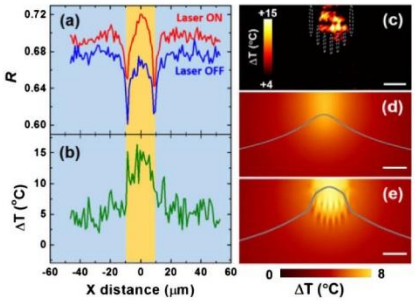

Fig. 3. (a) Variation of the intensity ratio R as obtained along the horizontal scans schematically indicated in Fig. 2 in presence and absence of 800 nm laser radiation. (b) Temperature increment profile calculated from (a). (c) Cross-sectional thermal image of the Nd:YAG waveguide. Dashed lines indicate the position of damage tracks. All experimental data were obtained for 100 mW of injected power at a distance of 100 μm from the input face. Calculated thermal image of waveguide assuming (d) a homogeneous thermal conductivity or (e) a localized thermal conductivity reduction at damage tracks. Gray lines are obtained at a depth of 5 μm. Scale bar is 10 μm in (c)–(e).

conditions, the laser-induced thermal load in ULI Nd:YAG waveguides is on the order of a few degrees. Although the partial absorption of the 800 nm laser radiation causes a slight temperature increment in the waveguide surroundings, the temperature increment is well-localized at the waveguide's volume. This is further ratified by the thermal image included in Fig. 3(c), obtained by analyzing the ratio-based fluorescence images of Fig. 2. The strong spatial localization of the laser-induced heating suggests that the damage tracks are behaving as a material volume with large thermal impedance capable of producing strong thermal confinement. This is, indeed, in agreement with the results published by Bellouard *et al.* [17], who concluded that ultrafast laser-induced damage tracks produced in transparent materials are characterized by a reduced thermal conductivity. Figures 2 and 3 reveal that the moderate temperature change induced in the waveguide by the "pump" beam affect neither the stress field nor the damage pattern (shift and width images in Fig. 2 are not affected by the presence of the "pump" beam). Note that this conclusion is valid for the laser powers and maximum temperature increments found in this work, but it is not general. For larger pump powers and temperature increments, the induced modifications in stress fields or the possible presence of self-annealing processes could not be neglected. Finally, from Fig. 3(b), we have estimated thermal gradients at the edge of the waveguide close to 0.5°C/μm that are more than 1 order of magnitude larger than the thermal gradients observed in laser crystals [18].

The effect that the reduction of thermal conductivity at damage tracks has on the spatial distribution of the laser-induced temperature increment has been also investigated by performing numerical simulations of the thermal diffusion equation using a finite difference approach. Thermal and spectroscopic properties assumed in our calculations were the same as those used by Innocenzi *et al.* [19]. Figure 3(d) shows the calculated steady-state temperature distribution caused by the 800 nm radiation propagating along the waveguide, assuming a homogeneous thermal conductivity (i.e., assuming that the ULI process does not modify the original thermal conductivity of the YAG network). In absence of any modification of thermal conductivity, the temperature increment spreads out of the waveguide volume due to heat diffusion. Figure 3(e) shows the steady state temperature distribution when a severe (80%) decrease in the thermal conductivity at damage tracks is assumed. This simulation was found to provide the best agreement between calculations and experimental data. Note that this assumed value is found reasonable when it is compared with the damage level caused by ULI in the Nd:YAG network that has been previously reported to range between 50% and 70% [14,20]. Although not identical, the calculated thermal profile well reproduces the main features of the experimental data included in Fig. 3(b): there is a slight temperature increment in the surroundings of the waveguide, but thermal loading is mainly taking place in the waveguide volume, which is further evidenced in the horizontal temperature files at a depth of 5 μm [gray lines in Figs. 3(d) and 3(e)]. At this point, it should be noted that although the numerical calculations reproduced the experimental temperature patterns qualitatively, a quantitative discrepancy is observed. While numerical simulations predict a temperature increment of 8°C within the waveguide volume, experimental measurements reveal a larger temperature increment of 15°C. The origin of this discrepancy is not fully understood yet, but we state that it could be due to different reasons, including the variation of the fractional thermal loading of Neodymium ions inside the waveguide's volume or the presence of heating centers associated with the formation of lattice defects. Nevertheless, what is clear from both the experiments and simulations presented here is that the magnitude of the laser-induced thermal loading is of a few degrees.

The maximum temperature increment induced inside the waveguide (ΔT_{WG}) was also measured as a function of the "pump" laser power injected into the waveguide at a fixed location (100 μm from the waveguide's input face) as shown in Fig. 4(a). Figure 4(b) depicts the surface temperature increment (ΔT_{surf}) at different distances from the input face for a fixed injected laser power (100 mW). Note that laser-induced heating was found to increase linearly with the injected 800 nm laser power and to decrease exponentially with the propagation length along the waveguide as was, indeed, expected.

In order to get an additional proof of the existence of the intrawaveguide temperature increments of a few degrees, an

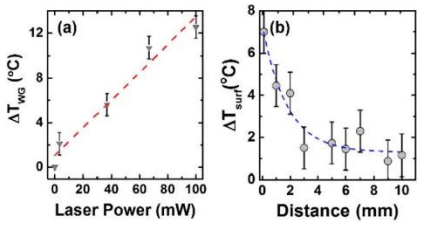

Fig. 4. (a) Waveguide temperature increment as a function of the 800 nm "pump" laser power at a fixed distance of 100 μm from input face. (b) Temperature increment for a fixed 800 nm injected laser power of 100 mW as a function of the distance from the input face. Dots are experimental data and dashed lines are the best fits to (a) linear and (b) exponential functions.

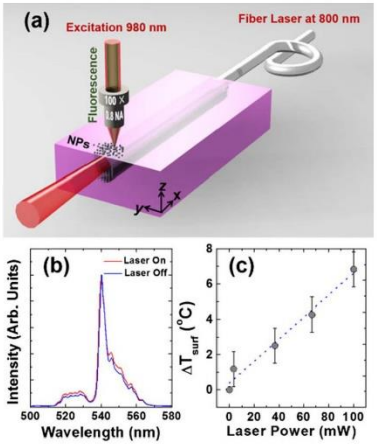

Fig. 5. (a) Schematic of the experimental setup used for surface temperature determination using Er:Yb:LaF_3 NPs. (b) Normalized upconversion spectra as obtained in presence and absence of 800 nm laser radiation propagating along the waveguide. (c) Laser-induced increment in the surface temperature as a function of the 800 nm laser-injected power. Data were obtained at 100 μm from the input face.

alternative approach for thermal sensing was carried out. Upconverting Erbium:Ytterbium co-doped LaF_3 nanoparticles were deposited on the top of the channel waveguide, as illustrated in Fig. 5(a). Here, the same experimental setup was applied but the "probe" 808-nm was replaced by a "probe" 980 nm laser beam. The purpose of this 980 nm beam is to excite, via a two-photon process, the green luminescence of Erbium ions. This technique has been widely used for high sensitivity ratiometric thermal sensing [6]. Basically, temperature sensing was obtained from the ratiometric analysis of the two emission lines of the 500–550 nm emission band of Erbium ions. Figure 5(b) shows the two-photon emission spectra generated by the Er:Yb:LaF_3 nanoparticles placed on top of the waveguide at a distance of 100 μm in respect to input face as obtained in either the presence or absence of "pump" 800 nm radiation propagating along the waveguide. It is clear that the presence of the "pump" propagating laser radiation induces a change in the Erbium emission spectrum, leading to an increment of the relative contribution of the 545 nm emission line that is unequivocally related to a temperature increment in the Er:Yb:LaF_3 nanoparticles. A quantitative analysis of the emission spectra, based on calibration curves previously reported [21], reveals a laser-induced temperature increment close to 7°C that can be attributed to be the laser-induced temperature increment at the waveguide surface (ΔT_{surf}). Note that the maximum temperature increment on the surface is smaller than inside the waveguide that is close to 12°C [Fig. 4(a)]. This difference was, indeed, reasonable, since temperature is expected to decrease rapidly when moving away from the waveguide core.

In summary, we have demonstrated how luminescence thermometry, in combination with high resolution confocal fluorescence imaging, constitutes a contact-free technique for intrawaveguide thermal imaging. The viability of this technique has been applied to the case of ULI Nd:YAG waveguides under real operation conditions. Two main conclusions have been extracted: first, for injected laser powers close to 100 mW, intrawaveguide laser-induced heating of a few degrees have been experimentally found. Second, thermal loading has been demonstrated to be mainly confined at the waveguide's volume due to the local reduction of thermal conductivity induced at the damage tracks that simultaneous behave as thermal and optical barriers.

Funding. Ministerio de Economía y Competitividad (MINECO) (FIS2013-44174-P, MAT2013-47395-C4-1-R).

Acknowledgment. Ruiyun He offers thanks for the support of the China Scholarship Council.

REFERENCES

1. A. J. Glass and A. H. Guenther, Appl. Opt. **12**, 637 (1973).
2. M. B. Bavil and E. Safari, J. Mech. Sci. Technol. **28**, 3231 (2014).
3. W. Koechner, Appl. Opt. **9**, 2548 (1970).
4. H. M. Pollock and A. Hammiche, J. Phys. D **34**, R23 (2001).
5. S. Chénais, S. Forget, F. Druon, F. Balembois, and P. Georges, Appl. Phys. B **79**, 221 (2004).
6. C. D. S. Brites, P. P. Lima, N. J. O. Silva, A. Millan, V. S. Amaral, F. Palacio, and L. D. Carlos, Nanoscale **4**, 4799 (2012).
7. D. Jaque and F. Vetrone, Nanoscale **4**, 4301 (2012).
8. J. Petit, B. Viana, and P. Goldner, Opt. Express **19**, 1138 (2011).
9. J. Siebenmorgen, K. Petermann, G. Huber, K. Rademaker, S. Nolte, and A. Tünnermann, Appl. Phys. B **97**, 251 (2009).
10. G. Salamu, F. Jipa, M. Zamfirescu, and N. Pavel, Opt. Mater. Express **4**, 790 (2014).
11. A. G. Okhrimchuk, A. V. Shestakov, I. Khrushchev, and J. Mitchell, Opt. Lett. **30**, 2248 (2005).
12. H. Liu, Y. Jia, J. R. Vázquez de Aldana, D. Jaque, and F. Chen, Opt. Express **20**, 18620 (2012).
13. A. A. Kaminskii, Laser Photon. Rev. **1**, 93 (2007).
14. A. Ródenas, G. A. Torchia, G. Lifante, E. Cantelar, J. Lamela, F. Jaque, L. Roso, and D. Jaque, Appl. Phys. B **95**, 85 (2009).
15. A. Benayas, B. del Rosal, A. Pérez-Delgado, K. Santacruz-Gómez, D. Jaque, G. A. Hirata, and F. Vetrone, Adv. Opt. Mater. **3**, 687 (2015).
16. S. Kobyakov, A. Kamińska, A. Suchocki, D. Galanciak, and M. Malinowski, Appl. Phys. Lett. **88**, 234102 (2006).
17. Y. Bellouard, E. Barthel, A. A. Said, M. Dugan, and P. Bado, Opt. Express **16**, 19520 (2008).
18. A. Benayas, E. Escuder, and D. Jaque, Appl. Phys. B **107**, 697 (2012).
19. M. E. Innocenzi, H. T. Yura, C. L. Fincher, and R. A. Fields, Appl. Phys. Lett. **56**, 1831 (1990).
20. A. Benayas, W. F. Silva, C. Jacinto, E. Cantelar, J. Lamela, F. Jaque, J. R. Vázquez de Aldana, G. A. Torchia, L. Roso, A. A. Kaminskii, and D. Jaque, Opt. Lett. **35**, 330 (2010).
21. E. C. Ximendes, U. Rocha, C. Jacinto, K. U. Kumar, D. Bravo, F. J. Lopez, E. M. Rodriguez, J. Garcia-Sole, and D. Jaque, Nanoscale **8**, 3057 (2016).

Research Article | Vol. 24, No. 14 | 11 Jul 2016 | OPTICS EXPRESS 16156

Optics EXPRESS

Two-photon luminescence thermometry: towards 3D high-resolution thermal imaging of waveguides

RUIYUN HE,[1,2] JAVIER RODRÍGUEZ VÁZQUEZ DE ALDANA,[3] GINÉS LIFANTE PEDROLA,[2] FENG CHEN,[1,4] AND DANIEL JAQUE[2,5]

[1]*School of Physics, State Key Laboratory of Crystal, Shandong University, Jinan 250100, China*
[2]*Fluorescence Imaging Group, Departamento de Física de Materiales, Facultad de Ciencias, Universidad Autónoma de Madrid, Madrid 28049, Spain*
[3]*Aplicaciones del Láser y Fotónica (ALF-USAL), Universidad de Salamanca, Salamanca 37008, Spain*
[4]*drfchen@sdu.edu.cn*
[5]*daniel.jaque@uam.es*

Abstract: We report on the use of the Erbium-based luminescence thermometry to realize high resolution, three dimensional thermal imaging of optical waveguides. Proof of concept is demonstrated in a 980-nm laser pumped ultrafast laser inscribed waveguide in Er:Yb phosphate glass. Multi-photon microscopy images revealed the existence of well confined intra-waveguide temperature increments as large as 200 °C for moderate 980-nm pump powers of 120 mW. Numerical simulations and experimental data reveal that thermal loading can be substantially reduced if pump events are separated more than the characteristic thermal time that for the waveguides investigated is in the ms time scale.

OCIS codes: (110.6820) Thermal imaging; (300.6410) Spectroscopy, multiphoton; (160.5690) Rare-earth-doped materials; (130.2755) Glass waveguides.

References and Links

1. G. Lifante, *Integrated Photonics: Fundamentals* (JohnWiley and Sons, 2008).
2. T. Suhara and M. Fujimura, *Waveguide Nonlinear-Optic Devices* (Springer, 2003).
3. A. J. Glass and A. H. Guenther, "Laser induced damage of optical elements–a status report," Appl. Opt. **12**(4), 637–649 (1973).
4. W. Koechner, "Thermal lensing in a Nd:YAG laser rod," Appl. Opt. **9**(11), 2548–2553 (1970).
5. M. B. Bavil and E. Safari, "Thermal and stress analyses in an end-pumped Nd:YAG slab laser using finite element method," J. Mech. Sci. Technol. **28**(8), 3231–3236 (2014).
6. G. Schreiber, H. Suche, Y. L. Lee, W. Grundkötter, V. Quiring, R. Ricken, and W. Sohler, "Efficient cascaded difference frequency conversion in periodically poled Ti:$LiNbO_3$ waveguides using pulsed and cw pumping," Appl. Phys. B **73**(5), 501–504 (2014).
7. D. Jaque and F. Vetrone, "Luminescence nanothermometry," Nanoscale **4**(15), 4301–4326 (2012).
8. C. D. S. Brites, P. P. Lima, N. J. O. Silva, A. Millán, V. S. Amaral, F. Palacio, and L. D. Carlos, "Thermometry at the nanoscale," Nanoscale **4**(16), 4799–4829 (2012).
9. R. He, J. R. Vázquez de Aldana, G. L. Pedrola, F. Chen, and D. Jaque, "All-optical thermal microscopy of laser-excited waveguides," Opt. Lett. **41**(9), 2061–2064 (2016).
10. F. Vetrone, R. Naccache, A. Zamarrón, A. Juarranz de la Fuente, F. Sanz-Rodríguez, L. Martinez Maestro, E. Martín Rodriguez, D. Jaque, J. García Solé, and J. A. Capobianco, "Temperature sensing using fluorescent nanothermometers," ACS Nano **4**(6), 3254–3258 (2010).
11. S. F. León-Luis, U. R. Rodríguez-Mendoza, I. R. Martín, E. Lalla, and V. Lavín, "Effects of Er^{3+} concentration on thermal sensitivity in optical temperature fluorotellurite glass sensors," Sens. Actuators B Chem. **176**, 156–164 (2013).
12. P. Haro-González, B. del Rosal, L. M. Maestro, E. M. Rodríguez, R. Naccache, J. A. Capobianco, K. Dholakia, J. G. Solé, and D. Jaque, "Optical trapping of $NaYF_4$:Er^{3+},Yb^{3+} upconverting fluorescent nanoparticles," Nanoscale **5**(24), 12192–12199 (2013).
13. P. Du, L. Luo, W. Li, and Q. Yue, "Upconversion emission in Er-doped and Er/Yb-codoped ferroelectric $Na_{0.5}Bi_{0.5}TiO_3$ and its temperature sensing application," J. Appl. Phys. **116**(1), 014102 (2014).
14. S. A. Wade, S. F. Collins, and G. W. Baxter, "Fluorescence intensity ratio technique for optical fiber point temperature sensing," J. Appl. Phys. **94**(8), 4743–4756 (2003).
15. K. T. V. Grattan and T. Sun, "Fiber optic sensor technology: an overview," Sensor. Actuat. A-Phys. **82**, 40–61 (2000).

#267158 http://dx.doi.org/10.1364/OE.24.016156
Journal © 2016 Received 26 May 2016; revised 2 Jul 2016; accepted 2 Jul 2016; published 8 Jul 2016

Optics EXPRESS

16. F. Chen and J. R. V. de Aldana, "Optical waveguides in crystalline dielectric materials produced by femtosecond-laser micromachining," Laser Photonics Rev. **8**(2), 251–275 (2014).
17. S. Gross and M. J. Withford, "Ultrafast-laser-inscribed 3D integrated photonics: challenges and emerging applications," Nanophotonics **4**(3), 332–352 (2015).
18. K. Sugioka and Y. Cheng, "Ultrafast lasers—reliable tools for advanced materials processing," Light Sci. Appl. **3**(4), e149 (2014).
19. V. K. Rai, "Temperature sensors and optical sensors," Appl. Phys. B **88**(2), 297–303 (2007).
20. L. Marciniak, K. Waszniewska, A. Bednarkiewicz, D. Hreniak, and W. Strek, "Sensitivity of a nanocrystalline luminescent thermometer in high and low excitation density regimes," J. Phys. Chem. C **120**(16), 8877–8882 (2016).
21. Z. Cai, A. Chardon, H. Xu, P. Féron, and G. M. Stéphan, "Laser characteristics at 1535 nm and thermal effects of an Er:Yb phosphate glass microchip pumped by Ti:sapphire laser," Opt. Commun. **203**(3–6), 301–313 (2002).
22. S. Chénais, S. Forget, F. Druon, F. Balembois, and P. Georges, "Direct and absolute temperature mapping and heat transfer measurements in diode-end-pumped Yb:YAG," Appl. Phys. B **79**(2), 221–224 (2004).
23. J. Petit, B. Viana, and P. Goldner, "Internal temperature measurement of an ytterbium doped material under laser operation," Opt. Express **19**(2), 1138–1146 (2011).
24. G. Canat, J. C. Mollier, Y. Jaouën, and B. Dussardier, "Evidence of thermal effects in a high-power Er^{3+}-Yb^{3+} fiber laser," Opt. Lett. **30**(22), 3030–3032 (2005).
25. A. Kosterin, J. K. Erwin, M. Fallahi, and M. Mansuripur, "Heat and temperature distribution in a cladding-pumped, Er: Yb co-doped phosphate fiber," Rev. Sci. Instrum. **75**(12), 5166–5172 (2004).
26. Y. Z. Xu, H. Y. Tam, S. Y. Liu, and M. S. Demokan, "Pump-Induced thermal effects in Er–Yb fiber grating DBR lasers," IEEE Photonics Technol. Lett. **10**(9), 1253–1255 (1998).
27. T. Liu, Z. M. Yang, and S. H. Xu, "3-Dimensional heat analysis in short-length Er^{3+}/Yb^{3+} co-doped phosphate fiber laser with upconversion," Opt. Express **17**(1), 235–247 (2009).
28. Y. Bellouard, E. Barthel, A. A. Said, M. Dugan, and P. Bado, "Scanning thermal microscopy and Raman analysis of bulk fused silica exposed to low-energy femtosecond laser pulses," Opt. Express **16**(24), 19520–19534 (2008).
29. Y. P. Lan, Y. F. Chen, and S. C. Wang, "Repetition-rate dependence of thermal loading in diode-end-pumped Q-switched lasers: influence of energy-transfer upconversion," Appl. Phys. B **71**(1), 27–31 (2000).
30. S. R. Bowman, S. P. O'Connor, and S. Biswal, "Ytterbium laser with reduced thermal loading," IEEE J. Quantum Electron. **41**(12), 1510–1517 (2005).
31. J. F. Philipps, T. Töpfer, H. Ebendorff-Heidepriem, D. Ehrt, and R. Sauerbre, "Spectroscopic and lasing properties of Er^{3+}:Yb^{3+}-doped fluoride phosphate glasses," Appl. Phys. B **72**(4), 399–405 (2001).
32. B. Lai, L. Feng, J. Wang, and Q. Su, "Optical transition and upconversion luminescence in Er^{3+} doped and Er^{3+}–Yb^{3+} co-doped fluorophosphate glasses," Opt. Mater. **32**(9), 1154–1160 (2010).

1. Introduction

Optical waveguides (WGs) are building blocks in modern integrated photonics as they provide full control over light propagation in the micrometric scale in an analogous way that microwires do in electrical circuits [1]. WGs are based on the controlled refractive index modulation at the micro and sub-micro scales designed for light confinement in an active volume of an enhanced refractive index and/or surrounded by low refractive index media. The requirements of integrated photonics restrict the typical dimensions of active volumes down to a few microns. Under those conditions, large photon densities could be achieved inside WGs and, hence, inside photonic circuits. Such large photon densities could be beneficial for some applications (e.g., those involving nonlinear processes [2]) but could also lead to the appearance of adverse effects [3–5]. Among all of the potential arising adverse effects, local heating has been well known to be of special relevance [3]. Intra-waveguide local heating arises from the partial absorption of propagating light by the material and its subsequent re-emission in the form of heat that could lead to relevant temperature increments at the WG volume and its surroundings. These local light-induced heating could lead to the appearance of a variety of adverse effects. For instance, the optical performance of any optical WG is determined by the refractive index contrast between WG active volume and its surroundings [4]. In most of the cases, refractive index is temperature-dependent so that intra-waveguide heating could modify the refractive index of WG active volume and, the refractive index contrast. This would lead to deterioration in the confinement ability of the optical WGs. In addition, the appearance of relevant thermal gradients in integrated photonic circuits could give place to the creation of no negligible stress fields that could affect both the performance and lifetime of those integrated circuits [5]. Moreover, in waveguide frequency converters

Optics EXPRESS

inscribed in non-linear crystal, the efficient generation of the new wavelength (i.e. second harmonic) is based on phase matching condition, that is very critical with slight changes of temperature. The conversion efficiency is thus highly dependent on temperature [6]. Control over heat generation processes inside WGs therefore becomes essential. Thermal control requires, as a first step, a detailed knowledge of the temperature patterns created by the propagating radiation inside WGs. The acquisition of thermal images of active WGs with sub-micron resolution is not an easy task at all. Thermal imaging of WGs should be obtained in a contact-less mode so that the optical performance of the WG would be non-affected by the measuring performance. Additionally, as WGs are three dimensional (3D) structures, full characterization would require the acquisition of 3D thermal images. Classical methods, such as Scanning Thermal Microscopy or Thermal Lens based interference methods failed to satisfy these two requirements simultaneously. Thus, the development of new thermal imaging techniques should be developed for thermal imaging of integrated optical WGs.

Luminescence Thermometry (LT) [7,8] is a relatively new thermal imaging technique that has been demonstrated to be a simple, flexible and sensitive approach capable of providing contact-free, 3D images of a great variety of systems. LT is based on the extraction of thermal information from an appropriate analysis of fluorescence images. Very recent works have demonstrated the suitability of LT for 3D thermal imaging of optical WGs, in particular of Nd:YAG WGs [9]. In that case, the Neodymium ions were used as thermal probes and the 3D capacity was provided by using a confocal architecture. In these conditions thermal sensitivity of obtained images was limited to 2 °C. To improve the thermal sensitivity of WGs thermal imaging, other luminescence probes with a superior sensitivity is required. Among the different luminescent ions as thermal sensors used in recent years, Erbium ions have been emerged of special relevance as they provide, based on their visible emission bands, thermal sensitivities in a large variety of materials larger than 0.01 $°C^{-1}$ (one order of magnitude larger than those provided, for example, by Neodymium ions) [10,11]. In addition, when combined with appropriate donor ions (such as Ytterbium), the thermal sensitive visible band of Erbium ions can be efficiently excited by infrared (980-nm) via a two-photon excitation process [12,13]. This would provide the LT with a superior spatial resolution via multi-photon microscopy without requiring the use of confocal apertures, i.e. with an improved acquisition times and signal-to-noise ratio. Erbium ions have been used in the past as thermal sensors in fibers [14,15] but its application for the acquisition of high spatial and thermal resolution 3D thermal images of integrated optical WGs has not been explored yet.

In this work, we focus on an Ytterbium and Erbium codoped phosphate glass produced by ultrafast laser inscription (ULI), a well-known technique for waveguide fabrication in dielectrics [16–18], and report on the acquisition of two-photon and 3D thermal images of ULI waveguides (ULI-WGs) by LT. The "pump and probe" experiments in combination with two-photon microscopy have been used to elucidate the 3D spatial extension and magnitude of the 980-nm laser-induced thermal loading in both the WG active volume and surroundings. Time modulation of the 980-nm pump radiation has been used to investigate the dynamics of thermal loading processes inside the WG. Results have been compared to numerical simulations, being in good agreement.

2. Experimental details

The Er:Yb:phosphate glass (doped with 1.5 wt.% Er_2O_3 and 4.5 wt.% Yb_2O_3) used in this work was cut to dimensions of 17 × 9 × 2 mm^3 and with all the faces polished to optical quality. An amplified Ti:Sapphire laser system operating at a wavelength of 800-nm, which produced pulses of 120 fs duration, 1 mJ maximum pulse energy at a repetition rate of 1 kHz, was utilized to fabricate surface cladding structures in the glass sample. For doing so the sample was placed in a 3-axes motorized stage with a spatial resolution better than 100 nm. The laser beam was focused through the sample surface by a 40 × microscope objective (N.A. = 0.65). Pulse energy of 0.36 μJ was found as the optimum value to produce filaments while

Optics EXPRESS

scanning the sample at a constant velocity of 0.5 mm/s. By inscribing parallel filaments with a lateral separation of 3 μm at different depths, surface cladding structures were inscribed.

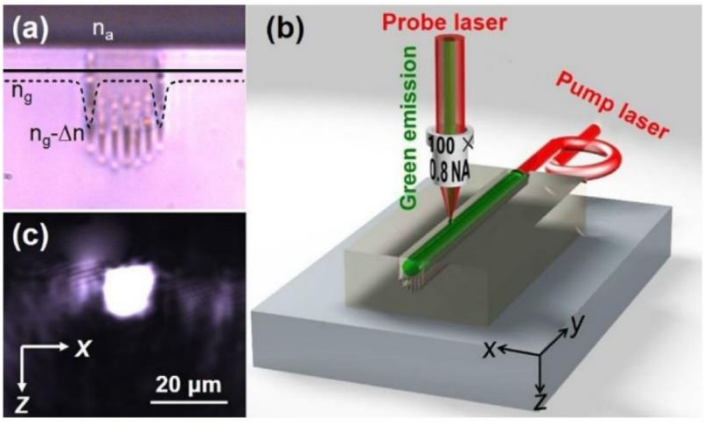

Fig. 1. (a) Cross-sectional optical microscope image of the surface cladding WG. The dashed line illustrate the refractive index profile at the depth of 5 μm, as indicated by the solid line. (b) Schematic of the "pump and probe" experimental setup. (c) Near-field spatial modal distribution at 800-nm. The scale bar is 20 μm for both (a) and (c).

Figure 1(a) shows the cross sectional optical microscope image of the surface cladding WG. The WG consists on a 17 μm in diameter semi-circle constituted by seven filaments and the glass/air interface. The ULI filaments has a decreased refractive index Δn. The waveguide core (n_g) is surrounded by the low refractive index ULI filaments (n_g-Δn) and the air (n_a = 1). The dashed line in Fig. 1(a) illustrates the refractive index profile at the depth of 5 μm, from which the two lateral filaments with low refractive index are clearly shown. These filaments act as a low-index barrier to confine the light propagation inside the waveguide volume. By using an end-coupling arrangement, a single mode fiber was pigtailed into the endface of the WG, as shown in Fig. 1(b). Figure 1(c) shows the near-field spatial modal distribution at 800-nm collected from the opposite endface of the WG, showing well-confined propagation. A schematic plot of the experimental setup used for two-photon florescence measurements and thermal imaging is included in Fig. 1(b). The Er:Yb phosphate glass was mounted on an *XYZ* motorized stage that allows the 3D scanning. The sample was optically excited by means of a single-mode fiber-coupled 980-nm laser diode. The "probe" laser beam was tightly focused into the sample by using a 100 × (NA = 0.80) near-infrared long working distance microscope objective. Based on the parameters of the "probe" laser beam and the microscope objective, the voxel volume of the "probe" laser is estimated to be 2.5 μm^3. The "pump" laser beam was coupled into the waveguide endface by single mode fiber.

The 980-nm laser radiation is absorbed by the Yb^{3+} ions ($^2F_{7/2} \rightarrow {}^2F_{5/2}$ transition), and then the energy is transferred from Yb^{3+} ions to Er^{3+} ions, leading to the excitation of Erbium ions up to $^2H_{11/2}$, and $^4S_{3/2}$ level, from which the subsequent green luminescence is generated, as depicted in Fig. 2(a). The two-photon green luminescence signal was collected by the same microscope objective and spectrally analyzed by a high-resolution spectrometer (Horiba Jobin Yvon iHR320). The micro-luminescence spectrum obtained in our experiment is shown in Fig. 2(b). In this work, we focused on the two thermal sensitive emission lines (525 nm and 545 nm, as depicted in Fig. 2(b)) as they can be used to detect the temperature modifications in the ULI Er:Yb:phosphate glass WGs. As commented in the introduction, several works have revealed that the intensity ration between these two emission lines can be used for high resolution thermal sensing. Such thermal sensitivity arises from the fact that these two lines are originated from the thermally coupled $^2H_{11/2}$ and $^4S_{3/2}$ states. As temperature changes, population redistribution among these states takes place, leading to remarkable change in the intensity ratio between these bands, in such a way that this intensity ratio can be used as a

Optics EXPRESS

temperature indicator. Figure 2(b) includes two micro-luminescence spectra obtained by coupling the 980-nm "pump" laser beam into the WG volume at two different powers, which induce different temperature increments in the WG. The remarkable ratio increment between the two emission lines as the temperature increases is observed. The intensity ratio R between the two visible bands, obtained as a function of the sample temperature, is shown in Fig. 2(c). The emission intensities were measured under only "probe" laser excitation when the glass sample was placed at a heating plate with temperature control from 10 to 60 °C. As can be observed the intensity ratio R varies in a linear way in the temperature range under this study. From the linear fit of experimental data, we can extract a relative ratiometric thermal sensitivity S to be 0.9% °C^{-1}, where S is defined as [19]:

$$S = \frac{1}{R}\frac{dR}{dT} \tag{1}$$

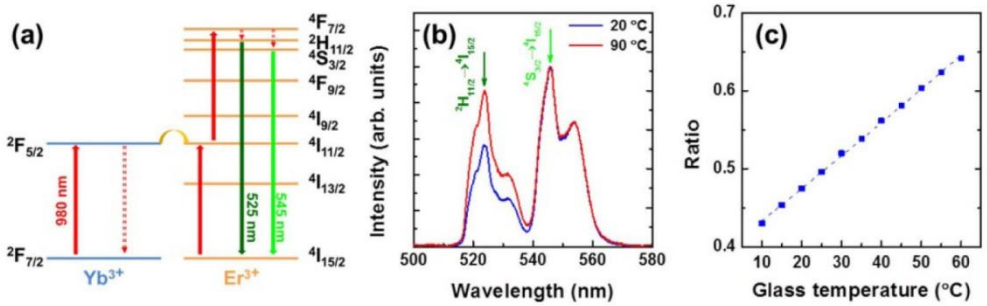

Fig. 2. (a) Energy level diagram showing the relevant states of the Yb^{3+} and Er^{3+} ions and the two-step up conversion excitation mechanism. (b) Normalized micro-luminescence emission spectra obtained at two different "pump" laser powers. The two emission lines used for ratiometric thermal sensing are indicated. (c) Ratio increment as a function of the glass temperature. The dashed line indicates the linear fit of the experimental data.

3. Results and discussion

In the "probe and pump" setup, the "probe" beam is considered as a background contribution. The temperature increment caused by the "probe" beam is estimated to be 40 °C, which is a fixed constant value in the following measurements. To get rid of the fluorescence variation created by the "probe" beam, we have measured the "ratio maps" with the 980-nm "pump" beam "on" or "off", while the "probe" beam is fixed at the same power. The net variation induced by the "pump" beam in the intensity ratio was obtained by subtracting the ratio map with the "pump" beam off and "probe" beam on from that with both the "pump" and "probe" beams on. The temperature increment ΔT refers to thermal loading induced by the "pump" laser propagating in the waveguide with the background temperature is excluded. A recent work on the Er based luminescent thermometer proves that the excitation power density is an important factor to the thermal sensitivity determination [20]. Here we discussed the effect of the excitation power density in our "probe" and "pump" measurement, showing that the thermal sensitive is a constant in this system. For the "probe" laser, the excitation density is estimated to be 2×10^6 W/cm^3, while it is lower by two orders of magnitude for the "pump" laser, ranging from 2×10^4 to 4×10^4 W/cm^3 at different powers. So we can conclude that the variation of the thermal sensitivity at different "pump" laser densities is negligible as the "probe" laser density is much higher. The large ratiometric thermal sensitivity of Erbium ions (Fig. 2(c)) allows us to obtain 3D thermal images from the proper calibration of the 3D micro-luminescence images obtained in terms of the intensity ratio R.

Optics EXPRESS

3.1 Thermal loading under continuous wave excitation

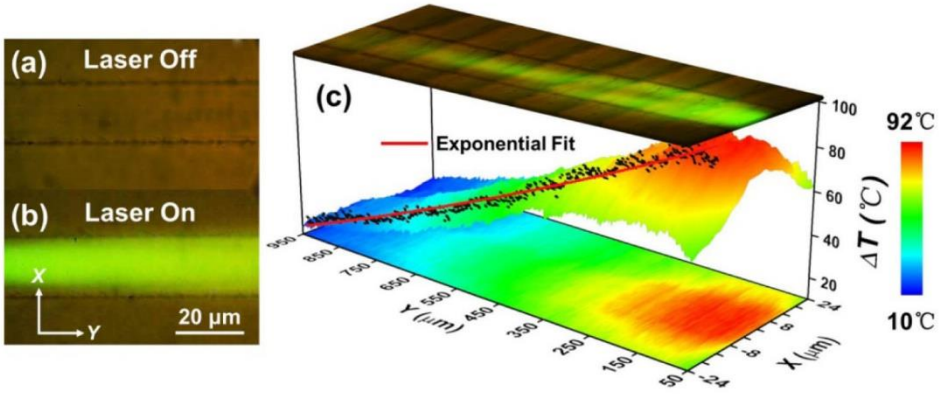

Fig. 3. Microscope images of the WG surface: (a) "pump" laser off and (b) "pump" laser on, in which the confined green emission generated by the "pump" 980-nm laser is clearly shown. (c) 2D temperature image obtained along the WG propagation direction (*Y*). Position $Y = 0$ μm corresponds to the input face of the WG. The horizontal scan path (*X*) is indicated by the solid line in Fig. 1(a). The top view shows the green emission along the WG. The black dots are experimental data extracted from the 2D temperature image, illustrating ΔT versus position along WG propagation direction (*Y*) at $X = 0$ (in the middle of the waveguide volume). The solid red line is the exponential fit of the experimental data.

Following the above explained procedure we firstly obtained the temperature patterns created by the 980-nm "pump" radiation in the *XY* plane (top thermal images). Figures 3(a) and 3(b) depict the microscope top images of the WG. When the 980-nm "pump" laser was switched off, optical image reveal the presence of the parallel ULI damage tracks constituting the WG. On the other hand, in presence of 980-nm "pump" radiation propagating along the WG, the up-converted green emission generated by Erbium ions is clearly observed, being well confined within the WG volume (i.e. between damage tracks). The *XY* (top) thermal image was obtained by scanning the "probe" beam in the *XY* plane at a fixed depth ($Z = 5$ μm) while keeping the "pump" laser power fixed. Figure 3(c) shows the experimentally obtained *XY* image as obtained for a "pump" 980-nm laser power of 60 mW. From this *XY* temperature image, several conclusions can be extracted:

i. The "pump" laser induced intra-waveguide heating decreases along the WG propagation direction *Y*, being mainly concentrated in the first millimeter. This fact is attributed to the strong absorption of the 980-nm "pump" radiation along the WG by the Ytterbium ions. Indeed the absorption coefficient of our Er:Yb codoped phosphate glass has been measured to be $\alpha_{abs} = 8.2$ cm^{-1} at 980-nm, so that the propagation length of "pump" radiation is expected to be $L_{abs} = 1.2$ mm, defined as the length at which, the laser power is declined to 1/e of the input power. The absorption of pump radiation during the first 1 mm is further proved by the optical image included in Fig. 3(c) from which it is clear that green emission is almost completely attenuated along the first 1 mm of propagation length. What is more, the temperature increment is plotted as a function of the position along the waveguide propagation direction *Y*, following a good exponential fit.

ii. Secondly, thermal images revealed the presence of laser-induced thermal loadings as large as 92 °C for a moderate 980-nm "pump" power of 60 mW. This fact suggests that pump-induced thermal effects in Er:Yb glass WGs cannot be neglected at all and should be seriously considered during design and operation of such devices. These pump-induced thermal loadings have been, indeed, found to be comparable in a Er:Yb phosphate glass microchip laser [21], and much larger than lasers in Yb doped crystals [22,23] and Er:Yb codoped fibers [24–27].This large pump induced thermal loading could be due to the

large pump laser densities achieved in our WGs in which 980-nm pump radiation is confined between damage tracks separated only 17 μm.

iii. Finally, although the 980-nm pump radiation is well confined within WG volume, the temperature pattern clearly extends over the surroundings of the WG due to thermal diffusion.

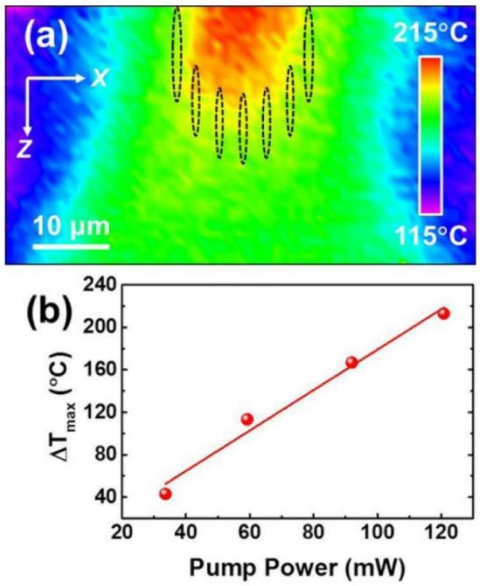

Fig. 4. (a) The cross sectional thermal image obtained at a distance of 50 μm from the input WG face with a CW 980-nm pump laser at a power of 120 mW. Dashed lines indicate the position of damage tracks. (b) Maximum temperature increments induced by different pump powers.

In order to get additional information about the confinement of the pump induced temperature pattern in the WG, we have also measured the cross sectional thermal image of the WG by scanning the 980-nm "probe" spot along the *XZ* plane. Figure 4(a) shows a WG cross sectional thermal image obtained at a distance of 50 μm from the input face with a CW 980-nm pump laser at a power of 120 mW. From this thermal image it is clear that, although some heating is also produced in the surroundings of the WG, it is mostly localized within the WG volume. Indeed, the ULI filaments (indicated by the dashed lines in Fig. 4(a)) seem to be producing an efficient thermal confinement that results in a high temperature increment inside the WG volume, reaching a maximum temperature increment around 215 °C. This suggests that damage filaments could act as "thermal barriers". This behavior is further supported by the fact that the observed "temperature spreading" in the surroundings of WG volume is highly anisotropic. Along the *Z* direction, parallel to the filaments, temperature gradients in the surroundings of WG are found to be close to 1.5 °C/μm whereas along the horizontal *X* direction (perpendicular to damage filaments) thermal gradients increase up to 1.9 °C/μm. These facts indicate that ULI damage filaments are behaving as anisotropic thermal barriers. This is, indeed, in agreement with the results published by Belloudard *et al.* [28] which concluded that ULI damage produced in transparent materials is characterized by a reduced thermal conductivity.

Finally, by measuring thermal images for different "pump" powers we were able to determine the variation of temperature increment induced at WG volume (ΔT_{max}) as a function of the 980-nm "pump" power. Results obtained at a fixed distance (50 μm) from the WG input endface are shown in Fig. 4(b). Note that in the "pump" power range under study in this work, the induced temperature increment has been found to follow a linear trend with

the 980-nm "pump" power. This fact reveals that, despite the large temperature increments induced in the WG volume (in excess of 200 °C), those are not causing relevant leaking of 980-nm "pump" radiation out of the WG, which would be detected by the appearance of sublinear behaviors in the temperature versus pump power curve.

3.2 Thermal loading under pulse excitation: Thermal accumulation effects

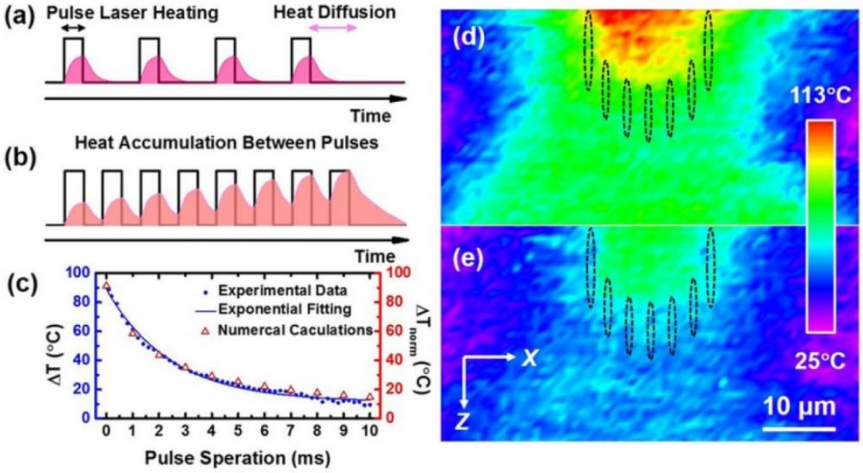

Fig. 5. Schematic representation of the heating and diffusion processes induced by a train of square laser pulses. (a) The pulse separation is long enough that the thermal diffusion has carried the heat away from the sample before the next pulse arrives. (b) The pulse separation is shorter than the time for heat to diffuse away, resulting in an accumulation of heat. (c) The experimental (solid circles) and numerical calculation (triangles) of temperature increment as a function of the pulse separation. The peak power was fixed to 60 mW, and the pulse width was fixed to 2 ms. (d) and (e) show the cross sectional thermal images obtained at a distance of 50 μm from the input face. (d) CW laser with a "pump" power of 60 mW. (e) Square pulse laser with a pulse separation of 2 ms and peak power of 60 mW. Dashed lines indicate the position of damage tracks.

Data included in previous section reveal that 980-nm pump induced thermal loading in Er:Yb ULI glass WGs cannot be neglected at all and it could lead to the appearance of adverse effects that could result, in the long term scale, to severe deterioration in their optical performance. In this sense, new strategies have to be developed to reduce this large thermal loading to avoid undesired deterioration. It has been proposed and experimentally demonstrated in previous works that time modulation of pump radiation could be used for efficient reduction of thermal loading. When the time distance between consecutive pump pulses (i.e., pulse separation) is larger than the characteristic thermal relaxation time ($\tau_{thermal}$), thermal accumulation between consecutive laser pulses is minimized resulting on a reduced average heating [21,26]. This possibility has been demonstrated to be especially suitable for the optimization of the laser performance of microchip lasers that are also characterized by large pump-induced thermal loadings of the active volume [29,30]. Nevertheless, up to the best of our knowledge, this possibility has not been yet demonstrated in laser excited WGs. In this section we have systematically studied the average heating induced in our ULI Er:Yb glass WGs by time-modulated pump radiation. The 980-nm "pump" laser was time-modulated to generate a train of square laser pulses with a fixed pulse width of 2 ms, a peak power of 60 mW and a pulse separation ranging from 0.1 ms to 10 ms. The waveform of the pulse laser is schematically illustrated in Figs. 5(a) and 5(b) for pulse separations significantly larger and shorter than the thermal relaxation time, respectively. In Fig. 5(a), when the pulse separation was significantly larger than $\tau_{thermal}$, almost complete heat dissipation occurs between pump pulses, in such a way that thermal accumulation does not take place. On the

other hand, when the pulse separation is below $\tau_{thermal}$, thermal relaxation between consecutive pump pulses does not occur and, as a result, thermal accumulation takes place, leading to a larger average temperature increment (Fig. 5(b)). This was experimentally verified by measuring the intra-waveguide temperature increment as a function of the pulse separation. Experimental data are included in Fig. 5(c) as solid circles. The uncertainty of the temperature increment is estimated to be ± 2 °C, showing the high accuracy of the data. It has been observed that the intra-waveguide temperature increment decreases monotonously with the pulse separation. By fitting the temperature increment versus time to a single exponential decay, a characteristic time constant close to 2 ms is found. Thus we conclude that the observed decrease in the average temperature increment is, indeed, caused by a reduction in the thermal accumulation between pump pulses.

The advantage of using time-modulated pump radiation is further evidenced in Figs. 5(d) and 5(e). In these figures we show the cross sectional thermal images obtained when the "pump" beam had a constant power of 60 mW and when the "pump"beam was constituted by a train of 2 ms width pulses with a pulse separation of 2 ms. In the last case, the pulse energy was set to 120 nJ that corresponds to a peak power of 60 mW (same as the power used under CW excitation). The thermal images show similar temperature distributions. In both cases, the thermal pattern is characterized by a remarkable thermal confinement inside the WG area. This unequivocally indicates that time modulation of the heat generation source has not effect on the spatial distribution of heat that it is mainly determined by the spatial confinement of pump radiation and the existence of thermal barriers (damage tracks). On the other hand, the magnitudes of the temperature increments are quite different. Indeed, time modulation of pump beam leads to a significant reduction in the maximum temperature increment inside the WG from 113 °C down to 60 °C. Figure 5 demonstrates the advantages of using modulated pump radiations for the minimization of undesirable thermal effects in integrated optical devices.

3.3 Numerical simulation

In order to corroborate the correctness of our measurements and the validity of our conclusions, numerical simulations of the thermal diffusion equation have been carried out by applying a finite difference approach. Thermal and spectroscopic properties assumed in our calculations were extracted from previous works describing Erbium and Ytterbium codoped phosphate glasses [31,32].

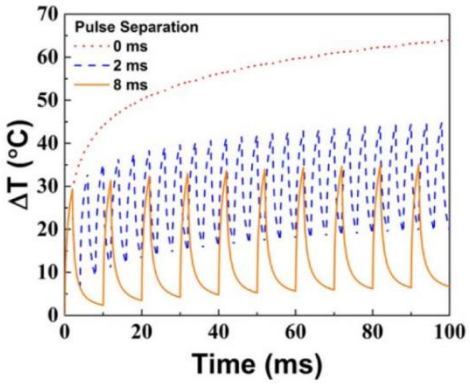

Fig. 6. Simulated time evolution of pump-induced temperature increment inside the WG for three different time configuration of the 980-nm "pump" radiation. The pulse separations are 0 ms (i.e. CW laser, dot), 2 ms (dash), and 8 ms (solid), from top to bottom, respectively.

Figure 6 shows the time evolution of the temperature inside the WG for three different time configuration of the 980-nm pump radiation. The dot line in Fig. 6 shows the calculated temperature when the pump beam was assumed to be a CW beam with a constant pump

Optics EXPRESS

power of 60 mW. Saturation is achieved when the heating rate caused by the absorption of pump radiation is equal to the heat dissipation due to temperature differences between environment and phosphate glass. When the pump beam was constituted by 2 ms pulses with a pulse separation of 2 ms, the time evolution of intra-waveguide temperature increment is shown in Fig. 6 (dash line). In this case, temperature increases during the laser pulse and relaxes during the time interval between pulses. Particularly, simulations reveal that complete thermal relaxation does not occur between consecutive pulses and thus heat accumulation takes place. As a consequence, WG temperature increases, on average, with time. It should be noted that the partial thermal relaxation between pulse leads to an average WG temperature smaller than that achieved under CW excitation. Finally, the solid curve in Fig. 6 shows the time evolution of WG temperature when the pulse separation was set to 8 ms that is larger than the characteristic thermal relaxation time. Again, WG temperature increases during the pump pulse but, at variance with previous cases, almost complete thermal relaxation occurs between pulses. In this case thermal accumulation between consecutive pulses is almost negligible and, consequently, the average WG temperature increment is almost negligible. The average temperature increment normalized to the temperature increment induced under CW excitation (T_{norm}) as a function of the time distance between pulses extracted from numerical calculations (triangles) has been included together with experimental data (solid circles) in Fig. 5(c). As can be observed, an excellent agreement between experimental data and numerical calculations has been obtained revealing the correctness of our calculations as well as the role played by thermal accumulation in the observed minimization of thermal loading when using time-modulated pump radiations.

4. Summary

In summary, we have demonstrated how the high thermal sensitivity of the two-photon excited luminescence of Erbium ions, in combination with high resolution multiphoton fluorescence imaging, constitutes an accurate, reliable and flexible three dimensional, contact-free technique for thermal imaging of photonic devices. In particular, we have provided high resolution 3D thermal images of 980-nm laser pumped ULI channel waveguide in an Erbium and Ytterbium codoped phosphate glass. Thermal images have revealed that in these structures laser induced thermal loading cannot be neglected at all. Temperature increments at waveguide's volume as large as 200 °C have been found for moderate pump powers of 120 mW. Furthermore, thermal images have also revealed a strong confinement of the pump induced thermal load at the waveguide's volume revealing the thermal impedance caused by the damage tracks that simultaneously behave as thermal and optical barriers.

Thermal images have also indicated that such relevant pump induced intra-waveguide thermal loading can be substantially reduced by time modulation of the pump beam. Experimental and numerical simulations have concluded that intra-waveguide thermal relaxation times are in the millisecond time scale in such a way that heat accumulation can be minimized by using pulse pump beams with time separation between pulses of few milliseconds.

This work introduces to the scientific community a high resolution, flexible, simple and versatile tool for the acquisition of 3D high resolution and time resolved thermal images of active photonic devices that would be essential for the complete understanding of their optical performance as well as for the optimization of their optical performance.

Funding

Ministerio de Economía y Competitividad of Spain (MINECO) (FIS2013-44174-P, MAT2013-47395-C4-1-R); National Natural Science Foundation of China (NSFC) (11274203).

Optics EXPRESS

Acknowledgments

Ruiyun He thanks the support of the China Scholarship Council.

Three-dimensional dielectric crystalline waveguide beam splitters in mid-infrared band by direct femtosecond laser writing

Ruiyun He,[1] Irene Hernández-Palmero,[2] Carolina Romero,[2] Javier R. Vázquez de Aldana,[3] and Feng Chen[1,*]

[1]*School of Physics, State Key Laboratory of Crystal Materials, Shandong University, Jinan 250100, China*
[2]*Centro de Láseres Pulsados (CLPU), Parque Científico, 37185 Villamayor, Salamanca, Spain*
[3]*Laser Microprocessing Group, Universidad de Salamanca, Salamanca 37008, Spain*
[*]*drfchen@sdu.edu.cn*

Abstract: We report on the fabrication of three-dimensional waveguide beam splitters in a dielectric $Bi_4Ge_3O_{12}$ (BGO) crystal by direct femtosecond laser writing. In the laser written tracks of BGO crystal, positive refractive index is induced, resulting in so-called Type I configuration waveguiding cores. The "multiscan" technique is utilized to shape cores with designed cross-sectional geometry in order to achieve guidance at mid-infrared wavelength of 4 μm. The fundamental mode guidance along both TE and TM polarizations has been obtained in the waveguide structures. With this feature, we implement beam splitters from 2D to 3D geometries, and realize 1 × 2, 1 × 3, and 1 × 4 power splitting at 4μm.

OCIS codes: (140.3390) Laser materials processing; (230.7370) Waveguides; (230.1360) Beam splitters; (130.3060) Infrared.

References and links

1. E. J. Murphy, *Integrated Optical Circuits and Components: Design and Applications* (Marcel Dekker, 1999).
2. G. C. Righini and A. Chiappini, "Glass optical waveguides: a review of fabrication techniques," Opt. Eng. **53**(7), 071819 (2014).
3. M. Quintanilla, E. M. Rodríguez, E. Cantelar, F. Cussó, and C. Domingo, "Micro-Raman characterization of Zn-diffused channel waveguides in Tm^{3+}:$LiNbO_3$," Opt. Express **18**(6), 5449–5458 (2010).
4. A. Tervonen, B. R. West, and S. Honkanen, "Ion-exchanged glass waveguide technology: a review," Opt. Eng. **50**(7), 071107 (2011).
5. F. Chen, "Micro-and submicrometric waveguiding structures in optical crystals produced by ion beams for photonic applications," Laser Photon. Rev. **6**(5), 622–640 (2012).
6. R. W. Eason, T. C. May-Smith, C. Grivas, M. S. B. Darby, D. P. Shepherd, and R. Gazia, "Current state-of-the-art of pulsed laser deposition of optical waveguide structures: Existing capabilities and future trends," Appl. Surf. Sci. **255**(10), 5199–5205 (2009).
7. F. Chen and J. R. Vazquez de Aldana, "Optical waveguides in crystalline dielectric materials produced by femtosecond-laser micromachining," Laser Photon. Rev. **8**(2), 251–275 (2014).
8. D. Choudhury, J. R. Macdonald, and A. K. Kar, "Ultrafast laser inscription: perspectives on future integrated applications," Laser Photonics Rev. **8**(6), 827–846 (2014).
9. T. Calmano and S. Müller, "Crystalline waveguide lasers in the visible and near-infrared spectral range," IEEE J. Sel. Top. Quantum Electron. **21**(1), 1602213 (2015).
10. K. Song, Y. Fan, and Y. H. Zhang, "Broad-band power divider based on radial waveguide," Microw. Opt. Technol. Lett. **49**(3), 595–597 (2007).
11. M. Sakakura, T. Sawano, Y. Shimotsuma, K. Miura, and K. Hirao, "Fabrication of three-dimensional 1 x 4 splitter waveguides inside a glass substrate with spatially phase modulated laser beam," Opt. Express **18**(12), 12136–12143 (2010).
12. S. Nolte, M. Will, J. Burghoff, and A. Tuennermann, "Femtosecond waveguide writing: a new avenue to three-dimensional integrated optics," Appl. Phys., A Mater. Sci. Process. **77**(1), 109–111 (2003).
13. Y. Tan, F. Chen, X. L. Wang, L. Wang, V. M. Shandarov, and D. Kip, "Formation of reconfigurable optical channel waveguides and beam splitters on top of proton-implanted lithium niobate crystals using spatial dark soliton-like structures," J. Phys. D Appl. Phys. **41**(10), 102001 (2008).
14. R. R. Gattass and E. Mazur, "Femtosecond laser micromachining in transparent materials," Nat. Photonics **2**(4), 219–225 (2008).

#226064 - $15.00 USD Received 30 Oct 2014; revised 27 Nov 2014; accepted 28 Nov 2014; published 10 Dec 2014

15. M. Ams, G. D. Marshall, P. Dekker, J. A. Piper, and M. J. Withford, "Ultrafast laser written active devices," Laser Photon. Rev. **3**(6), 535–544 (2009).
16. K. Sugioka and Y. Cheng, "Ultrafast lasers: reliable tools for advanced materials processing," Light Sci. Appl. **3**(4), e149 (2014).
17. Y. Liao, J. Song, E. Li, Y. Luo, Y. Shen, D. Chen, Y. Cheng, Z. Xu, K. Sugioka, and K. Midorikawa, "Rapid prototyping of three-dimensional microfluidic mixers in glass by femtosecond laser direct writing," Lab Chip **12**(4), 746–749 (2012).
18. N. Pavel, G. Salamu, F. Jipa, and M. Zamfirescu, "Diode-laser pumping into the emitting level for efficient lasing of depressed cladding waveguides realized in Nd:YVO_4 by the direct femtosecond-laser writing technique," Opt. Express **22**(19), 23057–23065 (2014).
19. G. Salamu, F. Jipa, M. Zamfirescu, and N. Pavel, "Cladding waveguides realized in Nd:YAG ceramic by direct femtosecond-laser writing with a helical movement technique," Opt. Mater. Express **4**(4), 790–797 (2014).
20. A. Zoubir, C. Lopez, M. Richardson, and K. Richardson, "Femtosecond laser fabrication of tubular waveguides in poly(methyl methacrylate)," Opt. Lett. **29**(16), 1840–1842 (2004).
21. R. Osellame, M. Lobino, N. Chiodo, M. Marangoni, G. Cerullo, R. Ramponi, H. T. Bookey, R. R. Thomson, N. D. Psaila, and A. K. Kar, "Femtosecond laser writing of waveguides in periodically poled lithium niobate preserving the nonlinear coefficient," Appl. Phys. Lett. **90**(24), 241107 (2007).
22. A. Rodenas and A. K. Kar, "High-contrast step-index waveguides in borate nonlinear laser crystals by 3D laser writing," Opt. Express **19**(18), 17820–17833 (2011).
23. R. Y. He, Q. An, J. R. Vázquez de Aldana, Q. M. Lu, and F. Chen, "Femtosecond-laser micromachined optical waveguides in $Bi_4Ge_3O_{12}$ crystals," Appl. Opt. **52**(16), 3713–3718 (2013).
24. A. Ródenas, G. Martin, B. Arezki, N. Psaila, G. Jose, A. Jha, L. Labadie, P. Kern, A. Kar, and R. Thomson, "Three-dimensional mid-infrared photonic circuits in chalcogenide glass," Opt. Lett. **37**(3), 392–394 (2012).
25. W. Drozdowski, A. J. Wojtowicz, S. M. Kaczmarek, and M. Berkowski, "Scintillation yield of $Bi_4Ge_3O_{12}$ (BGO) pixel crystals," Physica B **405**(6), 1647–1651 (2010).
26. J. Yang, C. Zhang, F. Chen, Sh. Akhmadaliev, and S. Q. Zhou, "Planar optical waveguides in $Bi_4Ge_3O_{12}$ crystal fabricated by swift heavy-ion irradiation," Appl. Opt. **50**(36), 6678–6681 (2011).
27. I. Bányász, S. Berneschi, N. Q. Khánh, T. Lohner, K. Lengyel, M. Fried, Á. Péter, P. Petrik, Z. Zolnai, A. Watterich, G. Nunzi-Conti, S. Pelli, and G. C. Righini, "Formation of slab waveguides in eulytine type BGO and CaF_2 crystals by implantation of MeV nitrogen ions," Nucl. Instr. Meth. B **286**, 80–84 (2012).
28. I. Bányász, Z. Zolnai, S. Pelli, S. Berneschid, M. Fried, T. Lohner, G. Nunzi-Conti, and G. C. Righini, "Single- and double-energy N^+ - irradiated planar waveguides in eulytine and sillenite type BGO crystals," Proc. SPIE **8627**, 862705 (2013).
29. I. Vurgaftman, J. R. Meyer, N. Tansu, and L. J. Mawst, "InP-Based Dilute-Nitride Mid-Infrared Type-II 'W' Quantum-Well Lasers," J. Appl. Phys. **96**(8), 4653–4655 (2004).
30. R. Y. He, Q. An, Y. C. Jia, G. R. Castillo-Vega, J. R. Vázquez de Aldana, and F. Chen, "Femtosecond laser micromachining of lithium niobate depressed cladding waveguides," Opt. Mater. Express **3**(9), 1378–1384 (2013).
31. Y. Y. Ren, G. Brown, A. Ródenas, S. Beecher, F. Chen, and A. K. Kar, "Mid-infrared waveguide lasers in rare-earth-doped YAG," Opt. Lett. **37**(16), 3339–3341 (2012).
32. A. J. Maker and A. M. Armani, "Low-loss silica-on-silicon waveguides," Opt. Lett. **36**(19), 3729–3731 (2011).
33. D. G. Lancaster, S. Gross, H. Ebendorff-Heidepriem, M. J. Withford, T. M. Monro, and S. D. Jackson, "Efficient 2.9 μm fluorozirconate glass waveguide chip laser," Opt. Lett. **38**(14), 2588–2591 (2013).
34. J. R. Macdonald, S. J. Beecher, A. Lancaster, P. A. Berry, K. L. Schepler, S. B. Mirov, and A. K. Kar, "Compact Cr:ZnS channel waveguide laser operating at 2,333 nm," Opt. Express **22**(6), 7052–7057 (2014).
35. J. R. Macdonald, S. J. Beecher, P. A. Berry, K. L. Schepler, and A. K. Kar, "Compact mid-infrared Cr:ZnSe channel waveguide laser," Appl. Phys. Lett. **102**(16), 161110 (2013).
36. J. Siebenmorgen, K. Petermann, G. Huber, K. Rademaker, S. Nolte, and A. Tunnermann, "Femtosecond laser written stress-induced Nd:$Y_3Al_5O_{12}$ (Nd:YAG) channel waveguide laser," Appl. Phys. B **97**(2), 251–255 (2009).
37. RSoft Design Group, Computer software BandSLOVE, *http://www.rsoftdesign.com*

1. Introduction

Optical waveguides, as the basic components in integrated photonics, offer the confinement of light propagation within small volumes, in which relatively high optical intensities could be achieved [1,2]. Several techniques, including metal-ion indiffusion [3], ion/proton exchange [4], ion implantation/irradiation [5], epitaxial layer deposition [6], and femtosecond laser micromachining/writing [7–9], have been employed to fabricate diverse configurations in various materials. Particularly, a number of approaches to achieving waveguide beam splitters, which could divide the input beam equally into multiple output waveguides without significant additional loss, have been reported in the literatures [10–13].

Recent years, the femtosecond laser writing has been widely applied as one of the most efficient techniques for micro-fabrication of transparent optical materials due to the advantageous capability of direct 3D micromachining over competing techniques [14–16]. In optics, it appears as a direct, rapid, maskless fabrication technique that can create optical

#226064 - $15.00 USD Received 30 Oct 2014; revised 27 Nov 2014; accepted 28 Nov 2014; published 10 Dec 2014

waveguides or more complicated photonic devices (splitters, optical circuits, etc.), avoiding temperature control or complex clean room facilities. With a suitable choice of laser parameters (wavelength, polarization, repetition rate, pulse energy, focusing conditions, moving speed), one can inscribe devices in various optical materials, including glass [11, 12, 17], crystals [18], ceramics [19], and polymers [20]. Femtosecond laser pulses with high intensities induce extremely localized modifications of material matrix through nonlinear absorption processes. The refractive index modification of the femtosecond laser irradiated regions could be either positive or negative, depending on the materials' nature as well as the laser parameters. The well-accepted configuration classification of femtosecond laser written optical waveguides includes Type I (index increased in the irradiated region) [7–9, 21, 22] and Type II (guiding cores typically within the region between two parallel damage tracks of reduced index) [7–9, 23], and Type III cladding structures (cores surrounded by a number of low-index tracks) [7–9]. Particularly, Type I structures are easier for direct 3D fabrication of complex devices. Moreover, the "multiscan" fabrication technique could be used to produce positive step-index cores with desirable cross-sectional shape [22, 24]. While it is very common in glasses [19, 20], Type I waveguides have only been reported in a few crystals, including LiNbO3 [21] and Nd:YCOB [22], with limitations in stability and polarization.

Bismuth germanate ($Bi_4Ge_3O_{12}$ or BGO) is a well-known scintillating crystal with cubic structure [25]. The features of BGO crystal, such as non-hygroscopic, high electro-optic coefficient and easy preparation, make it an ideal crystal for nuclear physics, space physics, high-energy physics, medicine, industry and other fields. In early works, BGO waveguides were fabricated by ion implantation/irradiation [26–28]. Femtosecond laser micromachining was also utilized in BGO crystal to fabricate Type II dual-line and depressed cladding waveguides [23]. Based on our previous work, we aim to write Type I BGO crystal waveguides supporting guidance along any transverse polarization. On the other hand, spurred by the development of quantum cascade lasers (QCLs) and fiber lasers [29], the MIR part of the spectra has become a region of numerous scientific and technological interests. So far, MIR optical waveguides have been reported in $LiNbO_3$ crystal [30], YAG crystal [31], silica on silicon [32], and chalcogenide glass [24], etc. The realization of compact MIR laser sources have been reported, which based on the femtosecond laser written waveguides in ZBLAN glass [33], Cr:ZnS [34], and Cr:ZnSe [35] crystals.

In this work, we report on the realization of Type I waveguides and 3D beam splitters at the wavelength of 4 μm in BGO crystal produced by direct femtosecond laser writing.

2. Experiments

An amplified Ti:Sapphire laser system, which produced linearly polarized pulses (120 fs duration, 800 nm wavelength, 1 mJ maximum energy, and a repetition rate 1 kHz) was utilized to fabricate straight waveguides and beam splitters in a BGO crystal with dimensions of 10 × 10 × 2 mm^3. In order to fabricate 3D structures with designed dimensions for MIR guiding, the multiscan procedure was implemented which implies the inscription of several parallel lines nearly overlapped. A 40 × microscope objective (N.A. = 0.40) was used to focus the beam approximately 50 μm below the largest surface of the crystal, that was positioned and moved with a XYZ translation stage. The scanning velocity was set to 500 μm/s in order to get an optimum spatial overlap between two consecutive pulses while minimizing the processing time as much as possible. Figure 1(a) shows a schematic of the femtosecond laser writing process. Many different trials were done changing the separation between adjacent tracks and pulse energy. Finally, the pulse energy (irradiated on the sample) of ~0.14 μJ and the separation of 3 μm were found as the best parameters, under our experimental conditions, for light guiding at 4 μm. In these conditions, two straight waveguides with 6 and 24 parallel scans, No. 1 and No. 2 respectively, were fabricated (see Fig. 1(b), left column). The 1 × 2 splitter (No. 3) was designed with a straight 3 mm length input arm, and two output arms with 0.4° of divergence (50 μm of lateral separation) at the same depth of the sample. The 1 × 3 splitter (No. 4) has a similar design and dimensions but the three outputs lie at different depths of the sample in a 3D configuration. Two 1 × 4 splitters were also implemented with lateral

#226064 - $15.00 USD Received 30 Oct 2014; revised 27 Nov 2014; accepted 28 Nov 2014; published 10 Dec 2014

separation between the arms of 60 and 110 μm (No. 5 and 6 respectively), forming squared 2 × 2 waveguide arrays at the output with 0.5° and 0.9° of divergence.

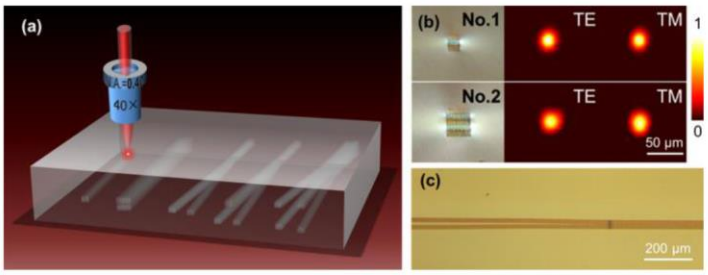

Fig. 1. (a) Schematic of the direct femtosecond laser writing process. (b) Optical microscope images of the cross sections of multiscan waveguides No. 1 (top) and No. 2 (bottom), and measured near-field intensity distributions at 4 μm. (c) Optical microscope image of the splitting point of the 1 × 4 beam splitter No. 6.

After direct femtosecond laser writing, the end faces were optically polished for measuring the guiding properties of the waveguides and beam splitters, resulting in a final length of 9.9 mm for all the waveguides. The microscope images of the cladding waveguide cross sections were taken by using a metalloscope (Axio Imager, Carl Zeiss) operating in transmission mode. The near-field modal distributions were investigated by utilizing a typical end-face arrangement. The linearly polarized laser at 4 μm, generated by the Tunable Laser System - MIRTM 8025 (Daylight Solutions, Inc.), was coupled into and out of the waveguides by MIR microscope objective lenses (ZnSe, LFO-5-12-3.75, N.A. = 0.13). A linear polarizer was placed before the input microscope objective lens to change the polarization of the incident light. Afterwards, a MIR beam imaging camera (WinCamD, DataRay Inc.) was employed to record the data. Based on the above arrangement and power meter, the propagation losses were determined by directly measuring the light powers coupled into and out of the end-faces. The coupling efficiency was estimated by considering the overlap of the incident light beam and waveguide mode. The coupling and Fresnel reflection losses of the waveguide systems were calculated as well.

3. Results and discussion

As shown in Fig. 1(b), the optical microscope images of the cross sections of the straight waveguides No. 1 and No. 2 exhibit well-defined rectangular shapes with dimensions of 16.4 × 18.3 μm^2 and 32.2 × 37.0 μm^2, respectively. Utilizing the multiscan technique, the desired waveguide cross sections were achieved with great precision and flexibility. In our previous work [23], Type II dual-line waveguides and depressed cladding waveguides were fabricated using the same laser facility but with different irradiation parameters. While for the dual-line waveguides, the pulsed energies were set to 1.68/2.52 μJ and the scan velocity was 50 μm/s, the parameters of the circular cladding waveguide was set to 1.68 μJ and 500 μm/s. In this work, in order to obtain waveguides for MIR with positive refractive index changes ($\Delta n > 0$) in the writing regions, the optimum parameters were found to be 0.14 μJ, 500 μm/s and 3 μm of lateral separation between tracks. As shown in Fig. 1(b), the Type I waveguides No. 1 and No. 2 supported fundamental mode guiding at 4 μm for both the TE and TM polarizations, respectively. By contrast, Type I waveguides in crystals reported before only supported guidance along one particular polarization direction [19,22].

The good performance of the straight waveguides reported above was also found in the beam-splitters (Nos. 3-6) that were written directly inside the BGO crystal with the same irradiation parameters. Figure 1(c) depicts the top view of the splitting point of beam splitter No. 6, showing smooth transition. The darker area around that point is produced by the irradiation with a larger amount of pulses as it is a stopping and starting point for the stage motion. The 1 × 2 and 1 × 3 splitters (Nos. 3 and 4) were fabricated with a 6 laser scans homogeneous section along all the waveguide (like waveguide No. 1), both in the entrance

#226064 - $15.00 USD Received 30 Oct 2014; revised 27 Nov 2014; accepted 28 Nov 2014; published 10 Dec 2014

waveguide as in the splitting arms. However, in splitters Nos. 5 and 6 the entrance waveguide was implemented with 24 scans (like waveguide No. 2) while the splitting arms have just 6 scans. We have used this strategy to decrease the laser damage at the splitting point and to obtain a more efficient beam division, making use of the fact that waveguides with both sections (Nos. 1 and 2) show similar fundamental mode performance. Figure 2 shows the microscope images of the end faces of the 1 × 2, 1 × 3, and 1 × 4 beam splitters. Also shown are the near-field intensity distributions of the beam splitters which, as expected, exhibit fundamental mode propagation at 4 μm along both the TE and TM polarizations.

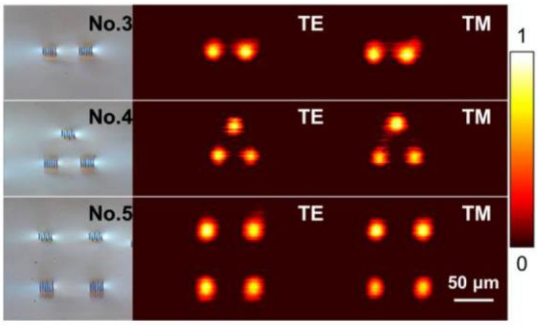

Fig. 2. Optical microscope images of the cross sections (left) and measured near-field intensity distributions at 4 μm of beam splitters Nos. 3-5 (right).

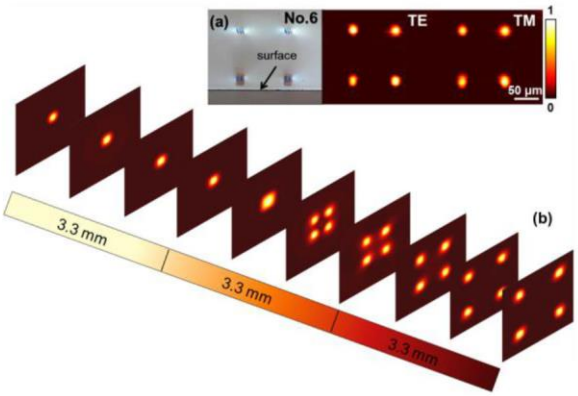

Fig. 3. (a) Optical microscope image of the cross section and measured near-field intensity distributions at 4 μm of the 1 × 4 beam splitter No. 6. (b) Simulated beam profile evolution for the 4 μm TE polarized light propagating along beam splitter No. 6.

In order to reconstruct the profile of the increased refractive index in the modified regions, we used the method introduced by Siebenmorgen *et al.* [36]. The calculated maximum refractive index contrast was estimated to be $(5.3 \pm 1) \times 10^{-3}$ for BGO straight waveguides at 4 μm. It seems reasonable to assume that the refractive index changes at 4 μm are approximately the same for the beam splitters. We simulated the light propagation at 4 μm by using the commercial program BeamPROP (Rsoft©, Inc), which is based on the finite-difference beam propagation method (FD-BPM) [37]. To determine more accurately the magnitude of the refractive index change (Δn), the same waveguide design was tested in the software with different values of Δn, ranging from 4.3×10^{-3} to 6.3×10^{-3} in 0.1×10^{-3} steps. By comparing the simulated profiles with the measured near-field intensity distribution in Fig. 3(a), the refractive index changes of the waveguide was determined to be 5.0×10^{-3}, for which the best agreement with the experimental results was obtained. Figure 3(b) shows the simulated beam profile evolution of 4 μm light propagating on TE polarization along the 1 × 4 beam splitter No. 6. As depicted in Fig. 3(a), a clear beam splitting is observed at the waveguide output with measured intensity splitting ratio of 27:26:23:24 for the four arms.

#226064 - $15.00 USD Received 30 Oct 2014; revised 27 Nov 2014; accepted 28 Nov 2014; published 10 Dec 2014

Although the splitting ratio is not equal, it could be improved by optimizing the design and processing parameters.

Table 1. Propagation Losses α (dB/cm) of the BGO Waveguides and Beam Splitters

	No. 1	No. 2	No. 3	No. 4	No. 5	No. 6
TE	3.39	3.70	3.35	3.70	3.81	3.95
TM	3.22	3.47	3.23	3.47	3.59	3.71

Table 1 shows the propagation losses (α) of the femtosecond laser writing waveguides and beam splitters (the coupling loss (~0.97 dB) and Fresnel reflection loss of the two end faces (:1.07 dB) are not included in the propagation loss). As one can see, the differences between TE and TM polarizations were less than 7%, showing the good features of polarization-insensitive guidance. The all-angle light transmission to investigate the thorough information of the polarization effects of the guidance was shown in Fig. 4. It is found that the guidance exists for the 4 μm laser light at any transverse polarizations. By comparing the propagation losses of the straight waveguides and beam splitters written with the same parameters, the additional losses of the 3D splitters were determined to be less than ~0.3 dB. A part of the splitting losses could be attributed to the imperfections of the structures, but the obtained values are significantly smaller than those reported for femtosecond laser written 1 × 3 splitters in pure fused silica (the splitting losses ~6 dB) [10].

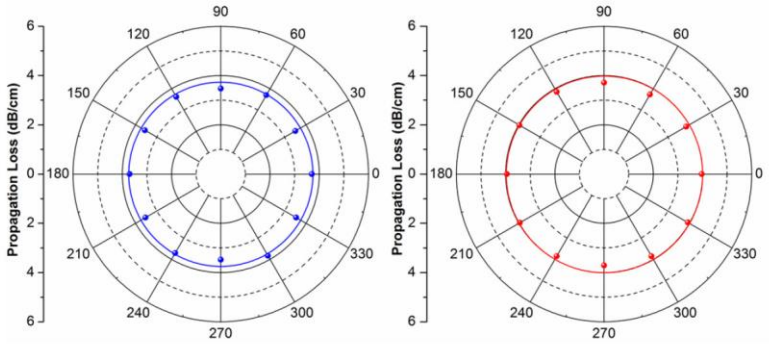

Fig. 4. Polar images of the propagation losses of BGO waveguide No.2 (a) and beam splitter No.6 (b) measured at 4 μm.

4. Summary

In conclusion, we have demonstrated the fabrication of 3D beam splitters in BGO crystal by direct femtosecond laser writing. For the waveguides and beam splitters with positive refractive index changes, fundamental mode guidance are achieved along both TE and TM polarizations at the wavelength of 4 μm. The propagation losses and splitting losses are estimated to be less than 4 dB/cm and 0.3 dB respectively, and the splitting ratio is almost equalized. The results show the promising capability of direct femtosecond laser written complex devices in BGO crystal for MIR applications.

Acknowledgments

This work was supported by the National Natural Science Foundation of China (No. 11274203), Junta de Castilla y León under project (SA086A12-2), and Ministerio de Economía y Competitividad under project (FIS2013-44174-P), Spain.

#226064 - $15.00 USD Received 30 Oct 2014; revised 27 Nov 2014; accepted 28 Nov 2014; published 10 Dec 2014